



CARBON NANOTUBE FIELD EMISSION ARRAYS

DISSERTATION

Benjamin L. Crossley, Major, USAF

AFIT/DCE/ENG/11-03

DEPARTMENT OF THE AIR FORCE

AIR UNIVERSITY

AIR FORCE INSTITUTE OF TECHNOLOGY

Wright-Patterson Air Force Base, Ohio

APPROVED FOR PUBLIC RELEASE; DISTRIBUTION UNLIMITED

The views expressed in this dissertation are those of the author and do not reflect the official policy or position of the United States Air Force, Department of Defense, or the United States Government. This material is declared a work of the U.S. Government and is not subject to copyright protection in the United States.

AFIT/DCE/ENG/11-03

CARBON NANOTUBE FIELD EMISSION ARRAYS

DISSERTATION

Presented to the Faculty

Graduate School of Engineering and Management

Air Force Institute of Technology

Air University

Air Education and Training Command

In Partial Fulfillment of the Requirements for the

Degree of Doctor of Philosophy

Benjamin L. Crossley, B.S.E.E., M.S.E.E.

Major, USAF

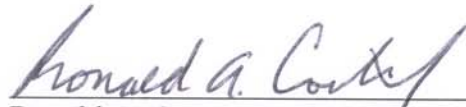
June 2011

APPROVED FOR PUBLIC RELEASE; DISTRIBUTION UNLIMITED

Carbon Nanotube Field Emission Arrays

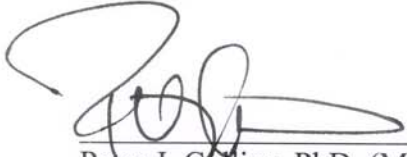
Benjamin L. Crossley, B.S.E.E, M.S.E.E.
Major, USAF

Approved:



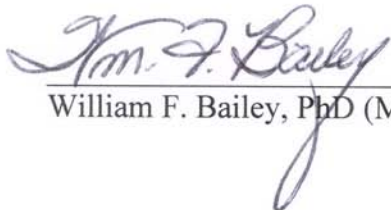
Ronald A. Coutu, Jr., PhD, (Chairman)

7 June 2011
Date



Peter J. Collins, PhD, (Member)

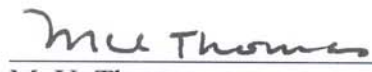
20 MAY 2011
Date



William F. Bailey, PhD (Member)

20 May 2011
Date

Accepted:



M. U. Thomas
Dean, Graduate School of
Engineering and Management

8 June 2011
Date

Abstract

This effort exploits the unique physical and electrical characteristics of carbon nanotubes (CNTs) for field emission applications. Carbon nanotube field emission devices are designed, fabricated, and tested. Two reliable CNT synthesis methods, microwave plasma enhanced chemical vapor deposition (MPE-CVD) and thermal chemical vapor deposition (T-CVD), are developed. The physical properties of the resulting CNTs are analyzed using Raman spectroscopy and Scanning electron microscopy (SEM) and then tested for field emission performance. The T-CVD grown CNTs are shown to have fewer growth defects, but suffer from less process control making integration into devices difficult without further process development. Field emission testing shows the T-CVD CNTs to be much better emitters, exceeding 13 mA/cm^2 at an electric field of only $1.4 \text{ V}/\mu\text{m}$, while the best MPE-CVD CNTs only managed $\sim 1 \text{ mA/cm}^2$ at the much higher electric field of $4.56 \text{ V}/\mu\text{m}$.

Two methods of device fabrication, conventional photolithography and nanosphere lithography, are developed and used to fabricate gated field emission arrays. Finite element analysis is used to optimize the gated array design to maximize the electric field strength. All fabrication steps are successfully demonstrated and prototype devices tested and compared to simple CNT carpet samples showing marked improvements by reducing electrostatic screening effects.

Acknowledgements

First and foremost, I owe my family, especially my wife, a debt of gratitude for helping and supporting me throughout this endeavor. For always providing me with new and different perspectives and continued motivation without which I would have never finished.

I would also like to thank my committee members, especially my advisor, for their assistance and encouragement.

Benjamin L. Crossley

Table of Contents

	Page
Abstract.....	iv
Acknowledgements	v
List of Figures.....	viii
List of Tables	xii
I. Introduction	1
1.1. Research Goals.....	3
1.2. Dissertation Organization	3
II. Background.....	5
2.1. Structure of Carbon Nanotubes.....	8
2.2. Mechanical Properties.....	15
2.3. Electrical Properties	17
2.4. Synthesis of Carbon Nanotubes	23
2.4.1. Arc discharge	23
2.4.2. Laser ablation.....	25
2.4.3. Thermal synthesis	25
2.4.3.1. Flame synthesis	26
2.4.3.2. Surface Decomposition	26
2.4.3.3. Chemical Vapor Deposition.....	27
2.4.3.4. Plasma Enhanced Chemical Vapor Deposition	28
2.5. Carbon Nanotube Growth Mechanisms	32
2.6. Sub-micron Patterning for CNT Synthesis	35
2.7. Field Emission	40
2.7.1. Fowler-Nordheim Model and Field Enhancement	40
2.7.2. Carbon Nanotube Field Emission	45
2.8. Summary	56
III. Plasma Enhanced CVD Carbon Nanotube Synthesis	58
3.1. MPE-CVD System.....	58
3.2. Substrate Preparation	59
3.3. Physical Vapor Deposition	60
3.4. Hydrogen Plasma Pretreatment.....	61
3.5. CNT growth	66
3.6. Pretreatment Study Conclusions	68
3.7. CNT Characterization and Process Improvements	69
3.7.1. Raman Spectroscopy.....	70
3.7.2. Improved MPE-CVD Synthesis Process	75
3.7.2.1. MPE-CVD Recipe	75
3.7.3. MWCNT Quality Analysis	76
3.8. Summary	78
IV. Thermal CVD CNT Synthesis Development and Characterization	79

4.1. Substrate Preparation	80
4.2. T-CVD CNT Synthesis Recipe	81
4.3. CNT Characterization	81
4.4. Field Emission Results	87
4.4.1. Test Chamber	87
4.4.2. Test Procedure	88
4.5. Summary	93
V. CNT Array Modeling and Simulation	96
5.1. Carbon Nanotube Array Models	97
5.2. COMSOL Multi-physics	100
5.3. Simulation Results	101
5.4. Summary	107
VI. CNT Field Emission Array Fabrication	109
6.1. Photolithography Process	110
6.2. Nanosphere Lithography	111
6.2.1. Fabrication Process	114
6.2.1.1. Drop Coating Process	116
6.2.1.2. Spin Coating Process	118
6.2.1.3. Spin Coating Results	119
6.2.1.4. Nanosphere Lithography Process Summary	124
6.3. Field Emission	125
6.4. Summary	127
VII. Conclusions	128
7.1. Contributions	131
7.2. Future Research	133
VIII. Bibliography	137

List of Figures

	Page
Figure 1. SEM images of a Spindt Cathode.....	2
Figure 2. Commercial Cathode CNT-based field emission display	3
Figure 3. Radushkevich TEM micrographs and SEM image CNTs grown at AFIT.....	5
Figure 4. Three Allotropes of Carbon.....	6
Figure 5. Graphene lattice showing unit vectors and chiral angle	9
Figure 6. Representations of the three types of SWCNTs.....	11
Figure 7. Hexagon base end cap and Pentagon base end cap	13
Figure 8. 90° bent SWCNT and bent MWCNTs	17
Figure 9. The Bravais lattice vectors and Brillouin zone of graphene.....	18
Figure 10. The energy dispersion relations for 2D graphite	19
Figure 11. Band structure of a (3,3) CNT and Band structure of a (4,2) CNT.....	20
Figure 12. Bandgap versus radius for zigzag SWCNTs	22
Figure 13. Basic electric arc discharge reactor	24
Figure 14. Simple laser ablation reactor schematic	25
Figure 15. Thermal CVD furnace	27
Figure 16. Microwave plasma enhanced chemical vapor deposition system	29
Figure 17. TEM images of pretreatments	31
Figure 18. Schematic of carbon nanotube base and tip growth mechanisms	34
Figure 19. SEM image of single MWCNT array.....	35
Figure 20. AFM patterned catalyst nanoparticles and individual MWCNTs	36
Figure 21. 0.5 μm PS monolayer and Ni catalyst particles.....	37

Figure 22. SEM images of CNT arrays from PS spheres	38
Figure 23. Block copolymer nanopatterning process	38
Figure 24. Statistical diameter distribution of catalyst particles and CNTs	39
Figure 25. Metal--Vacuum potential barrier and Triangular approximation	41
Figure 26. Fowler-Nordheim plot	43
Figure 27. Schematic of diode and triode configurations for field emission	48
Figure 28. Simulation of field penetration	50
Figure 29. Contour plots of local electric field	51
Figure 30. 5 μm diameter bundle array and inset of a single bundle tip	52
Figure 31. MWCNT bundle and inset of 5 bundle array	53
Figure 32. CNT device fabrication process	54
Figure 33. Single 10 x 10 μm^2 pixel and the corresponding profile	55
Figure 34. CNT bundle; Coated with oxide layer and released CNT bundle	56
Figure 35. Astex MPE-CVD System	59
Figure 36. 100 Å of evaporated Ni and sputtered Ni	61
Figure 37. 100 Å Ni Layer after 5 minute pretreatment	64
Figure 38. 5 minute pretreatment of 100 Å evaporated Ni and 100 Å sputtered Ni	65
Figure 39. CNT growth on 50 Å Ni, 100 Å Ni, and 200 Å Ni	67
Figure 40. Raman shift of various carbon materials	70
Figure 41. Commercial vertically aligned MWCNTs and Raman shift	72
Figure 42. T-CVD grown MWCNTs with truncated Raman shift	73
Figure 43. Poor quality CNT growth; defective CNT; and Raman shift	74
Figure 44. MPE-CVD grown CNTs and the corresponding Raman shift	77

Figure 45. SEM micrograph and Raman shift of MWCNTs grown via T-CVD.....	82
Figure 46. SEM of Cr100/Fe2 after T-CVD process	84
Figure 47. CNT carpet grown by T-CVD on Ti25/Fe10 sample.....	85
Figure 48. CNTs grown by T-CVD for 2 minutes on Ti25/Fe10 sample.....	87
Figure 49. Field Emission Test Chamber	88
Figure 50. Diode configuration testing schematic	88
Figure 51. Field emission current density plot for selected samples	89
Figure 52. Fowler-Nordheim plot for selected samples.....	91
Figure 53. Basic 2D model of 1 μm x 3 gate array with 1 μm pitch	98
Figure 54. Screening effects for single CNT, 200 nm spacing, and 50 nm spacing.....	101
Figure 55. E-field magnitude at CNT tips element arrays with varying pitches	102
Figure 56. Gated array with cross-section of E-field magnitude at CNT tips	103
Figure 57. Cross-section of E-field magnitude at CNT tips	104
Figure 58. Method for comparing similar CNTs of circular and square elements.	105
Figure 59. E-field magnitude at CNT tips across 2D element.....	106
Figure 60. Cross-section of E-field magnitude at CNT tips	107
Figure 61. Optimized CNT field emission array basic schematic	108
Figure 62. CNT field emission device photolithographic fabrication process.	110
Figure 63. Triode device fabricated by photolithographic process.....	111
Figure 64. 1 μm sphere monolayer	113
Figure 65. Complete device fabrication process.....	115
Figure 66. 1 μm sphere monolayer	117
Figure 67. Oxygen plasma etched 1 μm spheres	118

Figure 68. Monolayer of 500 nm diameter PS spheres.....	120
Figure 69. PS nanospheres after plasma ashing and PS nanospheres with Cr cap	122
Figure 70. 500 nm gate mask after PS release and after RIE	123
Figure 71. Single array element with CNTs	124
Figure 72. Field emission test of gated devices	126

List of Tables

	Page
Table 1. Collected data on field emission from CNT films or arrays.....	47
Table 2. Survey of reported CNT field emission since 2000.....	49
Table 3. Pretreatment Study Results.....	63
Table 4. Raman shift peak ratios and qualitative assessment	84
Table 5. Field emission data for all combinations of barrier/catalyst samples.....	91

Carbon Nanotube Field Emission Arrays

I. Introduction

Carbon nanotubes (CNTs) represent a relatively new material that has spawned an entire industry. Research into the properties and potential applications for CNTs began in 1991 when Iijima published an article identifying multi-walled carbon nanotubes (MWCNTs) [1]. In the ensuing years the characterization of unique and phenomenal mechanical, electrical, thermal, and chemical properties of CNTs has opened up vast potential applications in virtually every field of science and technology. This research effort is focused on just one of these applications--field emission.

CNTs have many characteristics ideal for field emission such as narrow diameters, high aspect ratios, high temperature stability, good conductivity, and structural strength. Developing high current density field emission arrays has been researched since the 1960s when Spindt first proposed micromachined sharp tipped structures for field emission [2]. Figure 1 shows scanning electron microscope images of a Spindt tip and the corresponding cathode array. Spindt cathodes have a number of limitations. The metal tips require much stronger fields for emission than CNTs, 100 V/ μm vs 1-10 V/ μm [3]. Spindt tips tend to form oxides which increase the work function and cause a decrease in emission current. The metal tips will sputter when bombarded with ionized particles. Sputtering will blunt the tip resulting in less field concentration and consequently reduce or stop emission [4]. The potential of CNTs to negate these

limitations and further improve field emission array performance provides continued motivation for CNT field emission research.

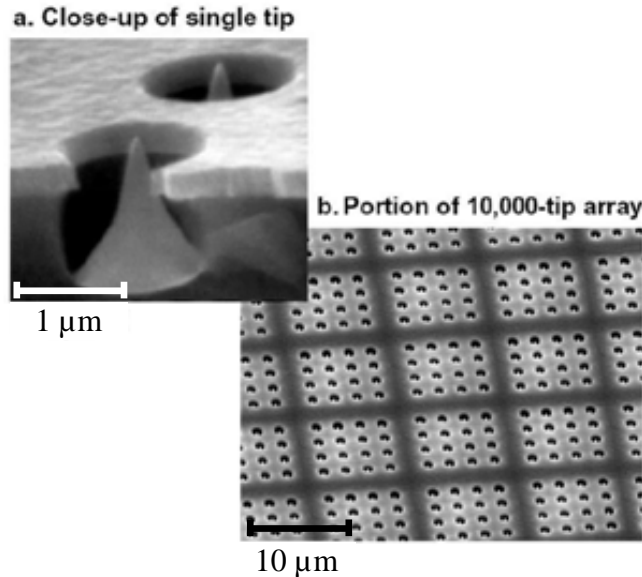
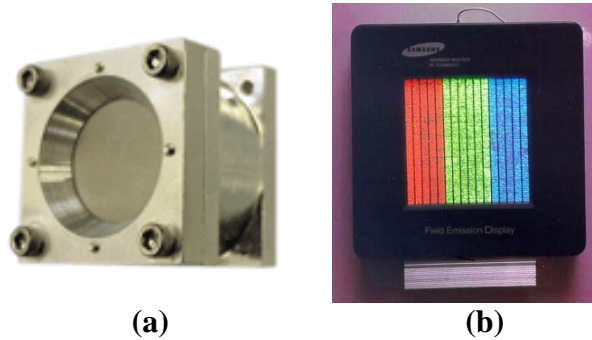


Figure 1. SEM images of a Spindt Cathode (a) a single tip and (b) the cathode array [5].

Carbon nanotube field emission arrays could have a number of applications. Of these applications these three receive the most research attention: flat panel displays, vacuum electronics and cold cathodes for charge neutralization for field emission electric propulsion (FEEP) on spacecraft. CNT-based field emission cathodes are commercially available. Busek Co. in Natick, MA offers half-inch cathodes, shown in Figure 2 (a), capable of 1.0 mA for over 6000 hours. The cathodes were to be deployed on the JPL, Space Technology 7/Disturbance Reduction System mission as part of the satellite FEEP system until funding was cut [6]. CNT-based field emission displays (FEDs) have received a lot of attention as a candidate for the next generation of flat panel displays. Many of the important performance metrics favor emission based displays such as wider field of view, brightness, and better color and contrast. In 1999, Samsung demonstrated

the small 4.5 inch CNT-based FED in Figure 2 (b) and has since developed a 38 inch color display [7].



**Figure 2. a) Busek Co. CNT-based Commercial Cathode [6]
b) Samsung CNT-based field emission display [7].**

1.1. Research Goals

The goal of this research effort was to develop state-of-the-art carbon nanotube fabrication and testing capabilities at AFIT with a focus on field emission applications. Research began with carbon nanotube synthesis. Two methods of fabrication were developed through detailed growth studies that highlighted new and important relationships between CNTs and different substrate and catalyst materials. Conventional and novel lithography methods were developed and employed to fabricate field emission devices. Finite element analysis was used to optimize the field emission device design. Testing included developing the ability to perform detailed analysis on the quality of the CNTs grown and test field emission device performance and determined relationships between CNT synthesis, quality, and performance.

1.2. Dissertation Organization

This dissertation is organized into seven chapters. Chapter II contains background information on the structure, physical and electrical properties, and synthesis methods of

carbon nanotubes. Current research into field emission devices and various methods of patterning and controlling CNT growth are also summarized. The development of multi-walled carbon nanotube synthesis via microwave plasma enhanced chemical vapor deposition and thermal chemical vapor deposition methods, along with the characterization of the resulting carbon nanotubes is explained in Chapters III and IV. Chapter V shows how a field emission array device design was optimized through a parametric study using finite element analysis. Efforts to fabricate and test field emission array devices, including the optimized design from Chapter V, are reported in Chapter VI. Finally, Chapter VII summarizes this research effort with conclusions and recommendations for future research.

II. Background

The first evidence of carbon nanotubes comes from transmission electron microscope (TEM) micrographs published by Radushkevich in 1952 in the Russian Journal of Physical Chemistry [8]. Armed with the knowledge of carbon nanotubes available today the micrographs, one of which is shown in Figure 3 with a scanning electron microscope (SEM) picture of recently grown CNTs, clearly show MWCNTs, however, without the capability to reliably produce, characterize, or use these carbon nanotubes little was done besides document their existence until 1991. Iijima effectively rediscovered or introduced carbon nanotubes to the scientific community as a by-product of an electric arc discharge method of synthesizing C60 fullerenes [1].

Iijima's discovery was coupled with a method of reliably reproducing the MWCNTs which led to an explosion of research in the area of carbon nanotubes. Iijima made another significant contribution with the discovery of single-walled carbon nanotubes (SWCNTs) in 1993 [9]. Researchers have scrambled ever since to refine

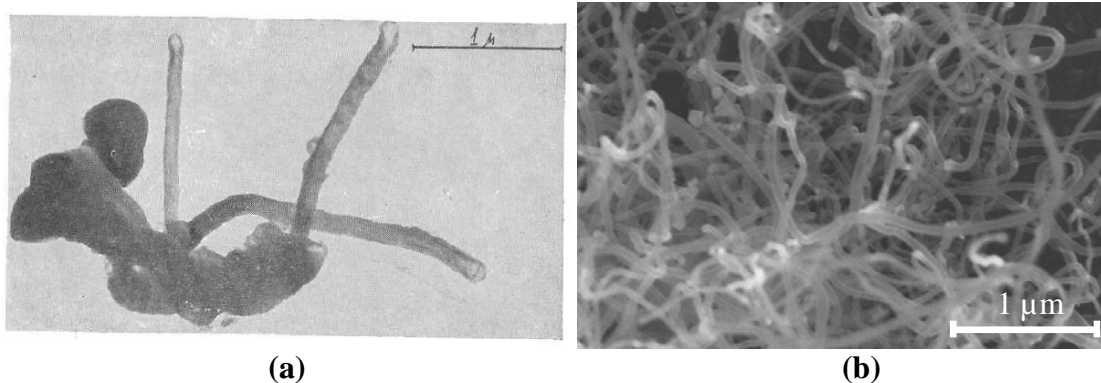


Figure 3. a) Radushkevich 1952 TEM micrographs of carbon nanotubes [8]. b) SEM image of representative CNTs grown at AFIT.

synthesis methods, define the growth processes, characterize the physical properties, and determine applications for both MWCNTs and SWCNTs. The results have been astounding and immense with an average of five CNT papers published a day and a billion dollar global industry growing up around the vast research efforts and few marketable applications [10].

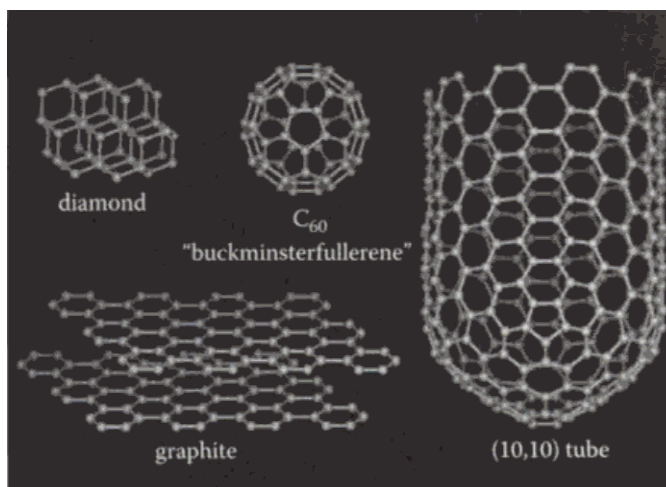


Figure 4. Three Allotropes of Carbon [12].

The element carbon is a very common and by far the most versatile element forming a myriad of organic compounds [11]. Carbon has 6 electrons, two of which fill the innermost shell or $1s$ orbital. The other four valence electrons can fill the sp , sp^2 , and sp^3 hybrid orbitals, depending on the solid allotrope formed [2]. Solid carbon can form three allotropes, shown in Figure 4 [12]. Diamond is the crystalline form of carbon resulting from the tetrahedral bonding of each carbon atom with four equidistant neighboring atoms. In this tetrahedral bonding configuration each of the valence electrons occupies the sp^3 hybrid orbital forming σ covalent bonds [2]. Graphite consists of hexagonal bonded sheets of carbon with three valence electrons occupying the planar sp^2 hybrid orbital. This forms three very strong in-plane σ bonds with the remaining

electron forming a weak out-of-plane π bond. Both diamond and graphite are common in nature and their respective properties have been studied extensively.

The third carbon allotrope, buckminsterfullerenes or fullerenes, was discovered in spherical form in 1985 by Rick Smalley *et al* [12]. The spherical fullerene or C_{60} fullerene consists of 60 carbon atoms bonded together in hexagons and pentagons forming a sphere like a soccer ball. Fullerenes of all sizes are single molecules, which is uniquely different from the other solid phase allotropes which are single element materials [12]. Besides the symmetrical C_{60} , the following fullerenes have been identified and characterized C_{70} , C_{76} , C_{78} , and C_{84} [11]. Although often referred to as a separate carbon allotrope, see Figure 4, carbon nanotubes are also members of the fullerene family. Carbon nanotubes are elongated fullerenes forming extremely high aspect ratio tubes. An ideal CNT is capped at each end with the hemisphere of a fullerene. Carbon nanotubes have similar σ - π bonding to graphite; however the radius of curvature of the tube causes unique properties, such as quantum confinement, that will be discussed below.

The properties of each of these allotropes of carbon vary greatly and open up many potential applications. Diamond has both the highest hardness and thermal conductivity of any known solid while being an excellent electric insulator [10]. Graphite's molecular sheets leave open bonds making electron transport easy resulting in semi-metallic conduction. The weak bonds between planar sheets make it an excellent dry lubricant but consequently a very soft material [12]. Fullerenes have properties ranging between diamond and graphite. Fullerenes, including nanotubes, form from carbon organizing in

different configurations resulting in different properties. This research focuses on the properties and applications of carbon nanotubes, which stem from their unique structure.

2.1. Structure of Carbon Nanotubes

Carbon nanotubes fall into two broad categories, single walled carbon nanotubes and multi-walled carbon nanotubes. Nanotubes are elongated fullerenes, however, nanotube structures are best described and understood from the perspective of a rolled graphene sheet. Single walled nanotubes consist of a single rolled graphene sheet and multi-walled nanotubes are multiple SWCNTs nested inside of each other. While this description has little in common with the actual process by which CNTs are formed, it provides an excellent method of uniquely describing CNTs and the corresponding fundamental physical properties.

In 1992, Hamada *et al* proposed describing the helical arrangement of the carbon hexagons in CNTs by referencing corresponding lattice points of a graphene sheet [13]. The result indicates an infinite number of possible CNT structures with a simple method to uniquely describe them. Hamada's method simply consists of choosing an origin point, \mathbf{A} , and another lattice point, \mathbf{A}' , on a 2-D graphene lattice as shown in Figure 5. Two single carbon atom hexagon unit vectors, \mathbf{a}_1 and \mathbf{a}_2 , are defined as:

$$\mathbf{a}_1 = \left(\frac{\sqrt{3}}{2}, \frac{1}{2} \right) a, \quad \mathbf{a}_2 = \left(\frac{\sqrt{3}}{2}, -\frac{1}{2} \right) a \quad (1)$$

where a is the length of the unit vectors and is determined from the carbon-carbon bond length as shown below [14]:

$$a = \sqrt{3}a_{cc} \quad (2)$$

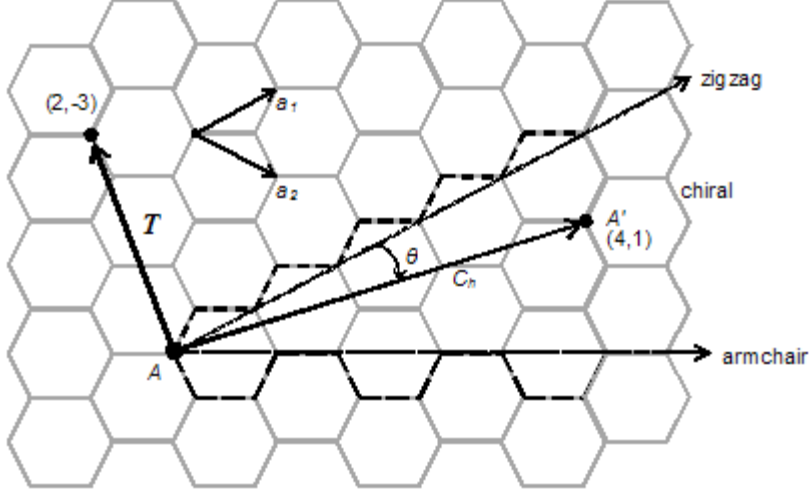


Figure 5. Graphene lattice showing unit vectors a_1 and a_2 , chiral vector, C_h , translation vector, T , and chiral angle, θ .

where a_{cc} is the carbon-carbon bond length [10]. The carbon-carbon bond length, usually given as 1.42\AA , is an approximation because the actual bond length is slightly different due to the curvature of the carbon nanotube [12]. The carbon-carbon bond length for graphene at 1.41\AA serves as a lower limit for a_{cc} because it is planar; as the radius of curvature decreases the bond length increases, for instance the C_{60} fullerene has a carbon-carbon bond length of 1.44\AA [10]. Using the unit vectors as a basis, a helical or chiral vector, C_h , can be defined between the origin and the chosen lattice point. The chiral vector is defined as:

$$C_h = n\mathbf{a}_1 + m\mathbf{a}_2 \quad (3)$$

where n and m are integers [15]. When the graphene sheet is rolled such that the origin will be superimposed on the chosen lattice point a SWCNT is formed with the helicity or chirality described by the chiral vector. A unit cell for a SWCNT can be determined by defining a unit vector for an unrolled CNT [14]. This CNT unit vector, referred to as the translation vector, is normal to the chiral vector and runs from the origin point A to the

next lattice point intersection. The translation vector is defined using the same basis vectors as before:

$$T = t_1 \mathbf{a}_1 + t_2 \mathbf{a}_2 \quad (4)$$

where t_1 and t_2 are integers which can be determined from the index integers n and m .

The equations for t_1 and t_2 as a function of n and m are given as:

$$t_1 = \frac{2m+n}{d_R}, \quad t_2 = -\frac{2n+m}{d_R} \quad (5)$$

Where d_R is the greatest common denominator between $(2m + n)$ and $(2n + m)$ [14]. Superimposing the chiral vector and translation vector at each end creates a rectangle that is defined as the carbon nanotube unit cell. The number of hexagons (N) and subsequently the number of carbon atoms contained in a unit cell is also a function of n , m , and d_R as shown below.

$$N = \frac{2(m^2 + n^2 + nm)}{d_R} \quad (6)$$

In the hexagonal lattice structure of a graphene sheet there are two carbon atoms per hexagon. The same is true for the rolled CNT lattice making the number of carbon atoms in a CNT unit cell equal to $2N$ [14].

The chiral vector, translation vector, chiral angle, and the corresponding nanotube diameter can all be determined from the integers, n and m [10]. Thus, SWCNTs are referred to using the simple indexing method, (n, m) . The three types of SWCNTs, zigzag, armchair, and chiral, are shown in Figure 5 with the corresponding chiral vector, translation vector and indexes for the chiral vector. Figure 6 displays a molecular representation of the three types of SWCNTs [12].

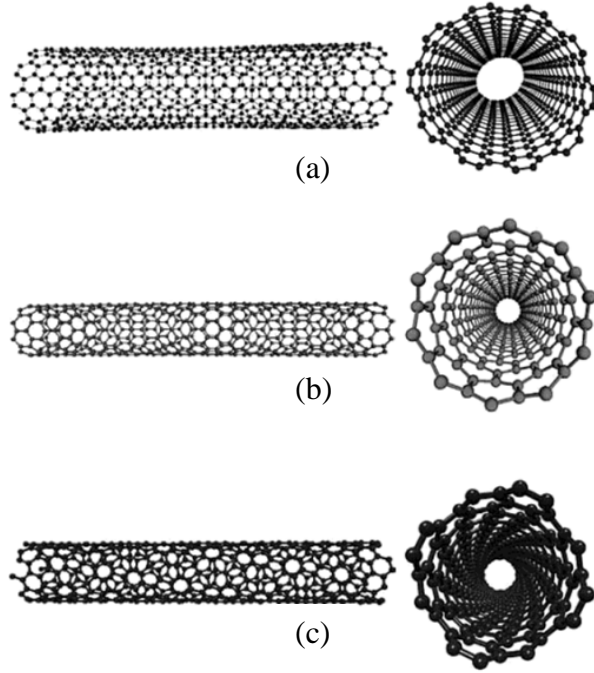


Figure 6. Representations of the three types of SWCNTs (a) armchair: $n = m$; (b) zigzag: $(n,0)$; and (c) chiral: (n,m) $m \neq 0$ [12].

All nanotubes with indexes of $(n, 0)$ are called zigzag because of the shape formed by the carbon hexagons along the chiral vector. The zigzag line forms the axis from which the chiral angle, θ , is measured [12]. Therefore, all zigzag nanotubes have a chiral angle of 0° . Due to the six fold symmetry of graphene the maximum chiral angle is 30° [10]. SWCNTs at this extreme are called armchair nanotubes, also because of the shape formed by the carbon hexagons along their chiral vector. Armchair nanotubes have indexes of (n, n) or in other words occur whenever $m = n$ [14]. The final type of SWCNT, encompassing all nanotubes that are neither zigzag nor armchair, is the appropriately named chiral nanotubes. Chiral nanotubes are truly chiral in nature meaning the nanotube and its mirror image cannot be superimposed. It should be noted that both zigzag and armchair nanotubes are achiral [9]. The chiral angle of chiral

nanotubes will be between 0° and 30° and can be calculated from the index using (7) shown below:

$$\tan(\theta) = \sqrt{3} \left(\frac{n}{2m+n} \right) \quad (7)$$

where θ is the chiral angle in degrees, n and m are the nanotube index integers [12].

The carbon nanotube is “rolled” along the chiral vector, so the vector length defines the nanotube circumference. The length of the chiral vector and subsequently the diameter can be determined from the index integers and the carbon-carbon atom bond length, a_{cc} . Equation (8) can be used to calculate the diameter (D) of a given carbon nanotube [10].

$$D = \frac{|C_h|}{\pi} = \frac{a_{cc} \sqrt{3(n^2 + m^2 + nm)}}{\pi} \quad (8)$$

The diameters of SWCNT are limited by the energy required to maintain the tubular shape. The smallest possible carbon nanotubes are theoretically the (5,0) zigzag CNT with a diameter of 0.39 nm, the (3,3) armchair CNT with a diameter of 0.41 nm, and the (4,2) chiral CNT with a diameter of 0.41 nm [16]. However, due to stability issues these nanotubes have not been grown as SWCNTs. Recently, Guan *et al* grew dual walled CNTs with a (3, 3) armchair nanotube (diameter 0.41 nm) inside a (12, 3) chiral nanotube (diameter 1.08 nm) [16]. This is the smallest measured CNT to date. At the other extreme SWCNTs are rarely larger than 2.5 nm due to a tendency to collapse into a nano-ribbon at larger diameters [10]. SWCNT diameters typically fall in the 1 – 1.5 nm range.

MWCNTs can range in diameter from 1 nm, like the dual walled nanotube reported above, to over a hundred nanometers. The distance between nested nanotubes is directly

related to the van der Waals bond or π bond that maintains the relatively weak bond between graphite sheets. This π bond creates the distance between graphite layers (0.335 nm) [11]. The same bond, stressed by the curvature of carbon nanotubes, causes a similar separation between nested nanotubes (0.34 nm) [9]. As such, much like graphite, the multiple nanotubes in MWCNTs only weakly interact with each other.

The bulk of research and structure details focus on the sidewalls of carbon nanotubes. The tips or ends of CNTs terminate in three ways, a carbon end cap, an open tube, or a catalyst nanoparticle. CNT end caps form from carbon atoms creating six pentagons and as many hexagons as necessary to match the CNT sidewalls. The very tip or base of the end cap can be a pentagon or hexagon as shown in Figure 7. The hemispherical shape of the end cap is caused by the formation of six pentagons. The placement of the pentagons determines the diameter and type of CNT the end cap will

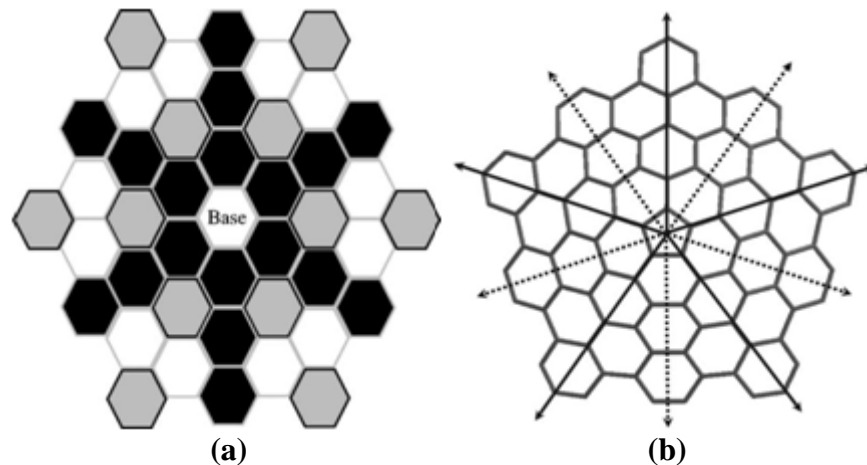


Figure 7. a) Hexagon base end cap, six pentagons placed in black spaces will match zigzag CNTs, six pentagons placed in gray spaces will match armchair CNTs, and six pentagons placed in any combination of black, gray, or white will match chiral CNTs. b) Pentagon base end cap, five pentagons placed in spaces along solid arrows will match armchair CNTs and five pentagons placed in spaces along dashed arrows will match zigzag CNTs [17].

match. Increasing the distance of the pentagons from the end cap base increases the diameter of the end cap hemisphere. When a hexagon base forms as shown in Figure 7 (a), the placement of the six pentagons in black spaces will match zigzag nanotubes, placement in the gray spaces will match armchair CNTs, and any placement combination in black, gray, or white spaces will match chiral CNTs [17]. If the base is a pentagon as shown in Figure 7 (b), the five remaining pentagons placed in spaces along solid arrows will match armchair nanotubes, while placing the five pentagons in spaces along the dashed arrows will match zigzag nanotubes [17]. The C_{60} fullerene hemisphere has a pentagon base with the remaining five pentagons located on the first space along the five solid arrows. The resulting diameter makes the C_{60} fullerene hemisphere the end cap for a (5,5) armchair CNT [18].

The structures described above are valid for defect free single wall and multi-wall carbon nanotubes. However, carbon nanotubes grown from most synthesis methods are rarely defect free, especially CNTs grown via chemical vapor deposition (CVD) methods. The common defects range from the relatively minor, such as heptagons and pentagons forming in the graphene lattice structure, to major defects that result in carbon nanofibers instead of nanotubes. When a metal catalyst nanoparticle is used in the synthesis process to nucleate CNTs, the nanoparticle will cap one end of the nanotube. The metal catalyst usually forms the cap at the tip or top of most MWCNTs due to the tip growth mechanism described in Section 2.5. CNTs without end caps are considered open. This can occur as a defect from early termination of the growth process; or CNTs capped with either carbon or a catalyst nanoparticle can be opened through an oxidation process. The

oxidation process is accomplished with either wet chemistry using dilute nitric acid or with gaseous oxidants such as oxygen or carbon dioxide [2]. Opening CNTs is usually accomplished for applications requiring increased chemical reactivity such as chemical functionalization.

Minor defects, such as heptagons and pentagons in the sidewalls and the defects at the carbon-catalyst interface at the CNT tip, are all potential field emission sites. Thus, for field emission applications such as this study these minor defects found in MWCNTs grown by CVD processes are necessary and will be discussed in Section 2.7.

2.2. Mechanical Properties

Since the discovery of CNTs the theoretical mechanical properties have driven much of the research. The potential for a single molecule material made from abundantly available carbon that is stronger than steel and reversibly deformable is a powerful motivator for research. CNTs have demonstrated these properties; however another unique and exciting feature, the nano-scale size of CNTs makes measuring mechanical properties accurately difficult. Initial tensile modulus (Young's modulus) measurements on MWCNTs, performed by measuring thermal vibrations with a transmission electron microscope, were reported as 1.8 TPa with a margin of error of ± 0.9 TPa [19]. Later, measurement methods using an atomic force microscope reported Young's modulus at 1.28 TPa [19]. Different measuring techniques coupled with different CNT synthesis or growth methods have resulted in a wide range of values for Young's modulus, especially for single walled CNTs. The typical value of Young's modulus used for MWCNTs is 1 TPa [10], [12]. Reported values and theoretical calculations for Young's modulus of

SWCNTs give a range of 0.5 – 5 TPa [20]. This wide disparity is well documented and has become known as “Yakobson’s Paradox,” after a researcher that published an extremely high theoretical calculation for Young’s modulus. The disparity also stems from results showing dependence upon CNT radius and chirality [20]. Often the Young’s modulus for SWCNTs is given as a modest 600-1000 GPa with a mention that theoretically the value could exceed 5 TPa [10], [12].

The same issues that plague accurate measurements of CNT Young’s modulus extend to tensile strength as well. Using an AFM to apply stress to a fixed SWCNT, Walters *et al*, were able to measure the tensile strength. The results were reported as a lower bound for tensile strength and strain of 45 ± 7 GPa and 5.8%, respectively [21]. Tensile strength for MWCNTs has been measured as high as 150 GPa and theoretical calculations place the upper limit at 300 GPa [10]. A tensile strength of 45 GPa is 20 times greater than steel and a Young’s modulus of 1 TPa is 5 times greater than steel while only a fraction of the density, 0.8 g/cm^3 for SWCNTs, 1.8 g/cm^3 for MWCNTs, and 7.7 g/cm^3 for steel [22]. These reported values place CNTs as the strongest and stiffest material known [10]. CNTs can withstand extreme strains up to 40% without suffering from plastic deformations or breaking [22]. These results in both single wall and double wall CNTs demonstrate the remarkable flexibility and strength of the hexagonal carbon lattice structure. As shown in Figure 8, nanotubes can fully recover from severe distortions even at angles greater than 90° without any plastic deformations [23].

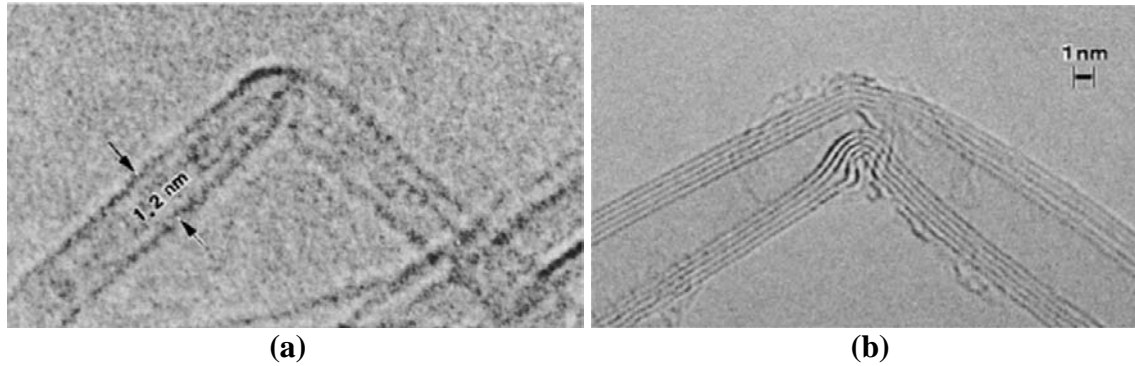


Figure 8. (a) 90° bent SWCNT and (b) bent MWCNTs; all CNTs recovered completely [23].

Carbon nanotubes, much like the other carbon allotropes, are stable at high temperatures. CNTs remain stable at temperatures exceeding 1500° C in an inert atmosphere [10]. The most interesting thermal property of CNTs is thermal conductivity. Theoretical molecular dynamics simulations indicate an incredibly high thermal conductivity of 6600 W/mK for an isolated SWCNT at room temperature which is much higher than even diamond [24]. The thermal conductivity for an individual MWCNT has been experimentally determined to be greater than 3000 W/mK [25]. The measured thermal conductivity of a SWCNT has been reported at 3500 W/mK [24]. These are some of the highest room temperature thermal conductivities reported until recently eclipsed by measurements of single layer graphene. The thermal conductivity of single layer graphene reported by Balandin *et al* was 5300 W/mK [26].

2.3. Electrical Properties

Research into the electrical properties of CNTs has focused primarily on single walled nanotubes. The high aspect ratio and hollow nature of CNTs make carrier transport one-dimensional (1-D) in nature. SWCNTs can be either metallic conductors or semiconductors depending on chirality. The energy gap of semiconducting tubes is

directly related to the SWCNT diameter. This coupled with the ability to sustain high current densities makes CNTs a leading candidate for nanoelectronics.

Much like the carbon nanotube structure, the electrical properties of SWCNTs are determined from the electrical properties of graphene. As shown in Figure 9 (a), the hexagonal lattice structure of graphene is not a proper Bravais lattice. The Bravais lattice is the two atom, A and B, based dotted rhombus; however the corresponding Brillouin zone in the reciprocal lattice, shown in Figure 9 (b), is hexagonal with labeled high symmetry points, Γ , K, and M [14]. Using the tight binding energy model, the energy dispersion relations for graphene can be calculated for the triangle formed from the high symmetry points. The results for the π covalent bonds which are perpendicular to the graphene plane are shown in Figure 10, where the upper half is the π^* -energy anti-bonding band, and the lower half is the π -energy bonding band. The unique feature of the

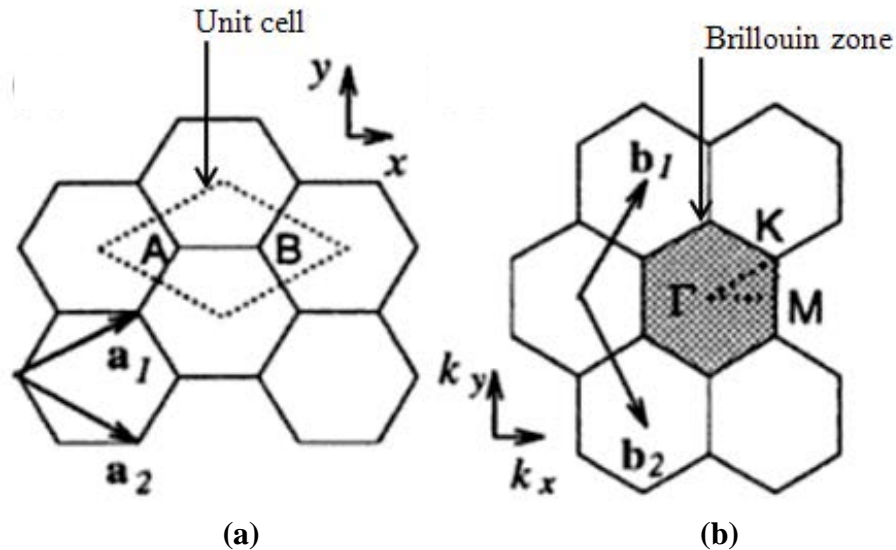


Figure 9. a) The Bravais lattice unit vectors, a_1 and a_2 , and unit cell. b) The corresponding reciprocal lattice vectors, b_1 and b_2 , and Brillouin zone of graphene [14].

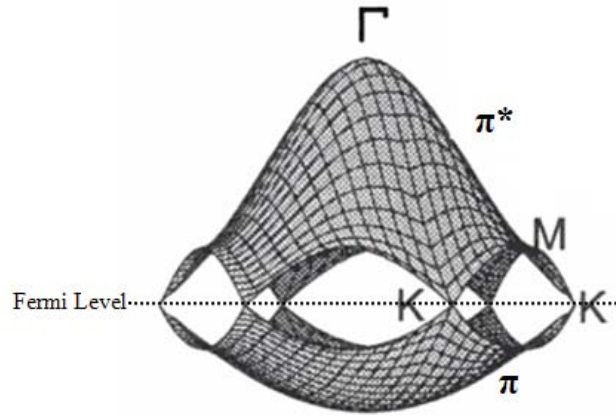


Figure 10. The energy dispersion relations for 2D graphite for the entire Brillouin zone [14].

graphene band structure is the six K points where the two bands are degenerate and the Fermi level passes. It has been shown through thorough calculations that at $T = 0$ K, the density of states is zero at the Fermi level, making graphene a zero band gap semiconductor [14]. It should be noted the many layers of graphene that make up graphite cause the bands to overlap making graphite a metal because both bands are partially filled even at $T = 0$ K. The unique zero band gap of graphene causes equally unique metallic or semiconducting properties, depending on chirality, for CNTs. Carbon nanotubes are considered one dimensional (1-D) because the periodic constraints caused by “rolling” the graphene sheet into a tube results in a 1-D Brillouin zone and N discrete 1-D wave vectors parallel to the CNT axis, where N is the number of hexagons in the CNT unit cell discussed in Section 2.1. The wave vectors along the tube axis are continuous for an infinite CNT and have a spacing of $2\pi/L$ for CNTs of finite length, L .

The band structure of a CNT can be determined using the zone folding approximation. Zone folding assumes the electronic band structure of a CNT is equivalent to the band structure of graphene along the allowed N discrete wave vectors.

Essentially the discrete wave vectors of the CNT are superimposed onto the graphene Brillouin zone [9]. Each wave vector then forms a cross-sectional cut through the band structure of graphene resulting in N 1-D energy bands. If one or more of the CNT wave vectors intercept a zero band gap K point on the graphene Brillouin zone then the CNT will be metallic. If the CNT wave vectors do not intercept a K point, the CNT will be semiconducting.

Figure 11 (a) shows the wave vectors of a (3,3) SWCNT superimposed on the graphene Brillouin zone with the closest wave vectors cut through the graphene band structure displayed. The wave vector intercepts two K points resulting in an overlapping band structure making the (3,3) SWCNT metallic. Figure 11 (b) has the same display for a (4, 2) SWCNT. Here the wave vectors do not intercept a K point; the resulting semiconducting band gap in the CNT band structure is clearly evident. SWCNTs can be

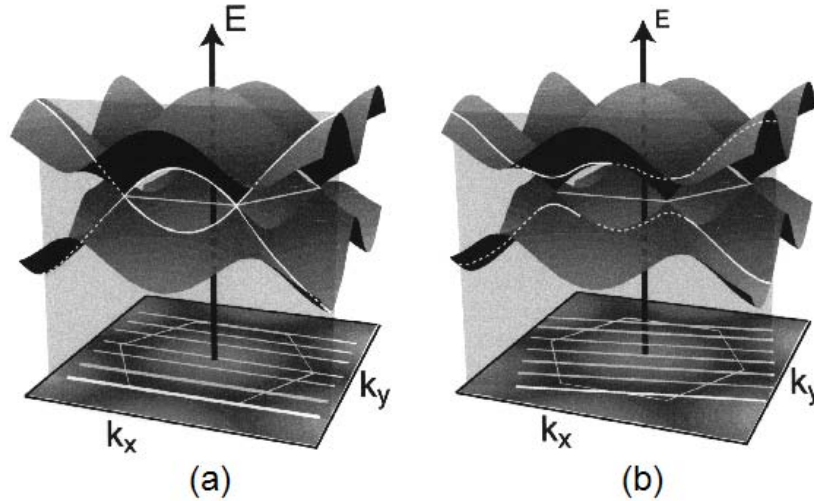


Figure 11. a) Band structure of a (3,3) CNT. b) Band structure of a (4,2) CNT. (bottom) Wave vectors (white lines) are superimposed over graphene Brillouin zone (hexagon). (top) CNT band structure are cuts through graphene band structure [27].

classified as metallic or semiconducting based on the index (n, m) using the following relationship:

$$\frac{n-m}{3} = q \quad (9)$$

If q is zero or an integer the nanotube is considered metallic. Under all other conditions it will be semiconducting. This works out mathematically that two thirds of all possible SWCNT are semiconducting while one third are metallic [9]. Armchair CNTs, indexed (n, n) , are truly metallic with fully overlapping energy bands. All other metallic carbon nanotubes as defined in Equation (9) have very small band gaps on the order of a few meV, the effects of which are negligible at room temperature [12].

The energy band gap of semiconducting CNTs is inversely proportional to the CNT diameter as shown in Equation (10) [14].

$$E_g = \frac{|t|a_{cc}}{D} \quad (10)$$

Where $|t|$ is the nearest neighbor Carbon-Carbon tight binding overlap energy (2.5 eV for 2-D graphene), a_{cc} is the Carbon-Carbon bond length (1.42 Å), and D is the diameter of the CNT as calculated using Equation (8). Another, more accurate, method of calculating the energy gap is given in Equation (11) below [20].

$$E_g = \frac{4\hbar v_F}{3D} \quad (11)$$

Where \hbar is the reduced Planck's constant, and v_F is the Fermi velocity. The energy band gap ranges from less than 10 meV for near metallic CNTs to 1.5 eV for semiconducting CNTs with small diameters [20]. Figure 12, a plot of calculated zigzag nanotube

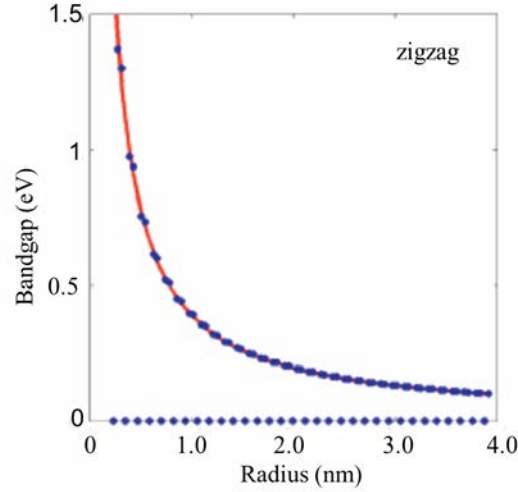


Figure 12. Bandgap versus radius for zigzag SWCNTs [7].

bandgap versus diameter, demonstrates the inverse relationship between bandgap and diameter.

It should be noted that only SWCNTs with diameters from 0.4 to 1.5 nm are actually grown because larger SWCNTs tend to collapse into ribbons [10]. The zero bandgap points are metallic CNTs that meet the conditions of Equation (9). The potential for a single material to be either metallic or semiconducting with a bandgap that can be engineered without doping is unique to carbon nanotubes. The electron confinement due to the 1-D nature of CNTs by definition limits carrier transport to one dimension, along the CNT axis, as well. This reduces electron scattering and correspondingly power dissipation. The strong carbon covalent bonds that give CNTs remarkable strength and thermal stability discussed in Section 2.2 also resist electromigration allowing CNTs to sustain current densities as high as 10^9 A/cm² [27].

Currently, with only one minor exception discussed in Section 2.4, there is no known method of controlling the chirality of the multiple nested tubes that make

MWCNTs. Thus about one third of the nested tubes will be metallic and are expected to dominate the electrical properties of the entire tube. As such, most MWCNTs tend to work as metallic conductors. However, it has been shown experimentally that at low bias most electric conduction occurs in the outermost tube of MWCNTs with some interaction with interior tubes, indicating that at least for low bias conditions the properties of the outer most tube dominate the electrical properties [20].

2.4. Synthesis of Carbon Nanotubes

Since Iijima recognized carbon nanotubes as a by-product of the arc discharge synthesis of fullerenes, the method has been refined for the fabrication of carbon nanotubes. There are three main carbon nanotube fabrication categories that have since been developed:

- Arc discharge synthesis
- Laser ablation synthesis
- Thermal synthesis.

Efforts to produce higher quality, larger quantities, and improve control have yielded a myriad of fabrication methods within each of these categories. The basic physics involved in each fabrication method defines the category.

2.4.1. Arc discharge

As mentioned above, arc discharge synthesis is also a well-documented method of producing carbon fullerenes which was the goal of Iijima when he first identified multi-walled carbon nanotubes. As such, arc discharge synthesis was the first synthesis method used to reliably produce both MWCNTs and SWCNTs [10]. Arc discharge or electric arc

discharge synthesis is accomplished by generating plasma between two graphite electrodes, as shown in Figure 13, using a low voltage, high current power supply. The process occurs in an inert atmosphere of He or Ar with pressures ranging from 100 to 1000 Torr [12]. The plasma contains vaporized carbon from the electrodes which then forms carbon nanotubes as it is deposited on the cathode and other areas of the reactor.

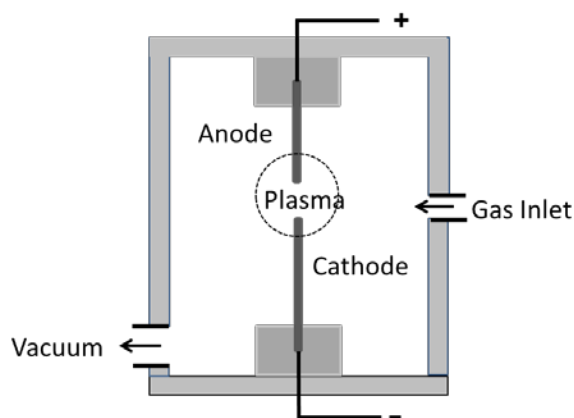


Figure 13. Basic electric arc discharge reactor.

SWCNTs can only be produced with the addition of a metal catalyst, usually added to the anode via a small hole where a catalyst/graphite powder mixture is placed. The first metal catalysts used were iron (Fe) and cobalt (Co); but a mixture of yttrium (Y) and nickel (Ni) is the current standard for SWCNTs producing a high yield, up to 90%, and fairly uniform diameters averaging from 1.2 to 1.4 nm [12]. CNTs produced using the arc discharge synthesis method require purification before use due to carbon soot and fullerene by-products. These processes, arc discharge synthesis and purification, have been well researched and developed. MWCNTs and SWCNTs produced via arc discharge are commercially available.

2.4.2. Laser ablation

The products of laser ablation is similar to arc discharge, both produce MWCNTs when a pure graphite target or anode is used; but can produce SWCNTs when the proper metal catalyst is present. Laser ablation or laser vaporization, as the name implies, uses a continuous-wave or pulsed-wave laser to vaporize a graphite or catalyst metal infused composite graphite target. The process occurs in a quartz furnace at 1200° C with a constant flow of inert gas, He or Ar [15]. Figure 14 is a simple schematic of a laser ablation synthesis method. The vaporized graphite creates a plume with nanoparticles of the metal catalyst which facilitate the growth of SWCNTs. The plume containing the carbon nanotubes and various by-products is swept through the furnace by the inert gas and collected via condensation on a cooled copper (Cu) collector. The presence of carbon by-products makes purification necessary. The diameter of SWCNTs produced from laser ablation average between 1.0 – 1.6 nm [12].

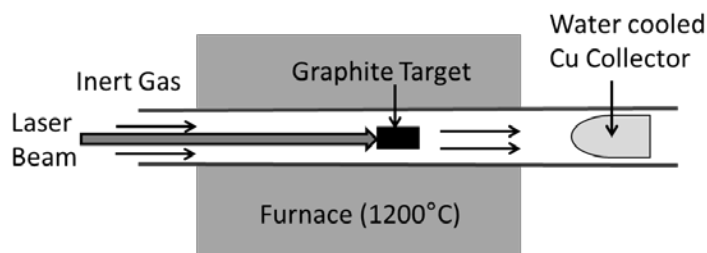


Figure 14. Simple laser ablation reactor schematic [15].

2.4.3. Thermal synthesis

Thermal synthesis is a broad category of synthesis methods that rely on thermal energy to produce CNTs. Included in this category is plasma enhanced chemical vapor deposition (PE-CVD), which is a hybrid of plasma based and thermal based synthesis, and silicon carbide (SiC) surface decomposition which, though a true thermal process, is

not often included in discussions of thermal synthesis methods. Due to the wide variety of options and precise control offered by thermal synthesis, chiefly chemical vapor deposition methods; this category has received the most attention from researchers and yielded the most promising results for controlled CNT fabrication.

2.4.3.1. Flame synthesis

The simplest method for producing CNTs, flame synthesis involves a fire composed of the proper stock materials. Flame synthesis has been used to produce both MWCNTs and SWCNTs by utilizing a hydrocarbon fire burning a mixture of 10% ethylene or acetylene, hydrogen gas (H_2) and an inert gas (He or Ar) with catalyst materials such as Fe or Co particles [12]. The yield rates for flame synthesis are currently very low, but the inexpensive simple process makes this method very alluring as a potential fabrication method.

2.4.3.2. Surface Decomposition

The fabrication of carbon nanotubes by surface decomposition of silicon carbide offers some unique benefits. First and foremost it is a catalyst free CNT synthesis, while other fabrication methods require metal catalysts, especially for the growth of SWCNTs. The by-products of surface decomposition are gaseous making purification processes, which can damage CNTs, unnecessary [28]. Finally, CNTs are vertically aligned and attached to the remaining silicon carbide substrate.

Surface decomposition is achieved through high temperatures in a relatively high vacuum. The temperatures necessary for SiC surface decomposition range from 1500° C to 1700° C. At these temperatures, it is theorized that the silicon becomes gaseous and

reacts with residual oxygen in the vacuum chamber. The remaining solid carbon realigns in either SWCNTs or MWCNTs depending upon the temperature and pressure settings [28]. Vacuum pressures for the process range from 10^{-3} to 10^{-5} Torr [28].

Surface decomposition as a carbon nanotube synthesis method is excellent; however applications for the end product are relatively few. The problems that plague this process begin with the source material. SiC is a difficult material to process and the high temperatures involved preclude patterning or other fabrication techniques which make integration into other fabrication technologies such as typical silicon based electronics impossible on a practical level. These drawbacks tend to limit the attention surface decomposition receives especially when compared to the process friendly chemical vapor deposition synthesis methods.

2.4.3.3. Chemical Vapor Deposition

CVD as a synthesis method could be considered a broad category by itself because of the vast number of variations that are available. The first and simplest form of CVD is thermal CVD. A thermal CVD system, as shown in Figure 15, consists of a furnace, feedstock gasses, and a vacuum pump. Resistive heaters or furnaces operate at temperatures ranging from 500°C to 1200°C in T-CVD systems. A substrate or target

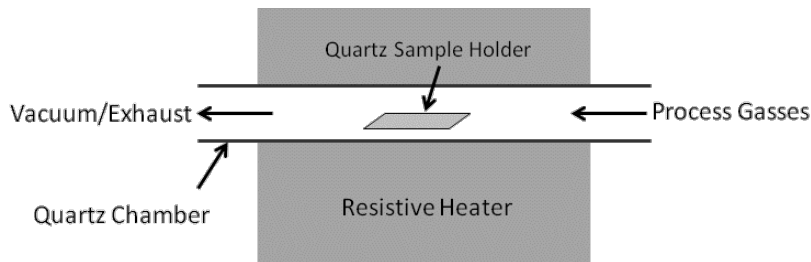


Figure 15. Thermal CVD furnace.

with Fe, Ni, Co, or an alloy of these three transition metals on the surface is placed in the furnace. An anneal in a non-volatile gas can be performed to form the necessary nanoparticles from thin films of the above mentioned catalyst materials. A carbon feedstock gas such as methane (CH_4) or carbon monoxide (CO) for SWCNT growth or acetylene (C_2H_2), ethylene (C_2H_4), or benzene (C_6H_6) for MWCNT is flowed across the target substrate [19]. The gas reacts with the catalytic nanoparticles to produce carbon nanotubes.

CVD synthesis occurs at relatively low temperatures that allow more conventional substrates, chiefly silicon, to be used, opening up opportunities for integration of CNTs with conventional electronics, optoelectronics, and other applications. With the proper growth conditions, pure CNTs can be produced with yield rates as high as 99% [12]. Thus no purification or post processing is necessary unless the catalyst metal must be removed. As a result thermal CVD and its many derivatives are the most widely used and researched carbon nanotube synthesis methods.

2.4.3.4. Plasma Enhanced Chemical Vapor Deposition

PE-CVD uses energy from H_2 plasma generated from a DC, radio frequency (RF), or microwave power supply, to break down the carbon feedstock gas and facilitate CNT growth at lower temperatures and pressures. Vertically aligned MWCNTs grown on a silicon substrate at temperatures below 330°C by microwave plasma enhanced CVD (MPE-CVD) have been documented [29]. Typical substrate temperatures range from 400°C to 900°C [12]. PE-CVD systems are capable of growing both SWCNTs and

MWCNTs; more importantly these CNTs can be patterned, vertically aligned, and grown on a variety of substrates.

To date, the only synthesis method known to preferentially produce CNTs of a specific chirality is via remote PE-CVD, a system that generates a low power plasma away from the growth substrate [12]. Li *et al* demonstrated the growth of very narrow SWCNTs with diameters from 0.8 nm to 1.5 nm. The chirality of these narrow diameter SWCNTs was such that 90% were semiconducting as opposed to 67% expected based on random growth [30]. Due to the lack of understanding of CNT growth mechanisms in general, the exact cause of this preferential growth is still unknown.

In order to achieve well aligned vertical CNTs an external magnetic or DC electric field in the form of a negative bias on the substrate is necessary. Typical values range from -150 V for SWCNTs to -650 V for MWCNTs [31], [32]. A common MPE- CVD system is shown in Figure 16. Microwave power, up to 1 kW, is transmitted from the generator through a wave guide to a microwave coupler that emits the radiation via the antenna into the CVD chamber. If conditions are correct, the resulting plasma will be centered over the substrate and allow for CNT growth over large areas, $>10\text{ cm}^2$. The

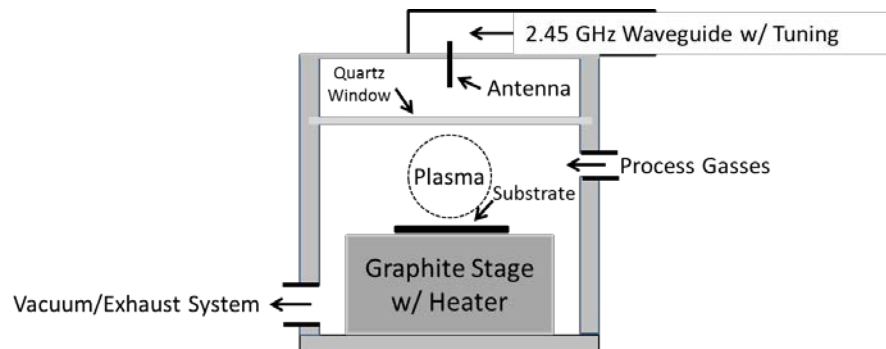


Figure 16. Microwave plasma enhanced chemical vapor deposition system.

CNT growth and plasma formation are dependent upon a number of controllable variables: the microwave power, chamber pressure, gas composition, gas flow, and substrate temperature. The ability to precisely control so many of the growth parameters is the key reason that CVD and PE-CVD in particular has become the most researched synthesis method.

All CVD methods require a metal catalyst nanoparticle to facilitate the growth of CNTs. Fe, Co, and Ni are most common, although alloys consisting of these and yttrium, molybdenum (Mo), ruthenium (Ru), and platinum (Pt) have resulted in increased yields under specific conditions [12]. In thermal CVD processes the alloy FeCo results in 10-100 times higher yields of SWCNTs over Fe alone [29].

There are a number of methods for depositing the catalyst on the substrate, many of which can be easily patterned making it possible to grow CNT arrays at desired locations. Common methods include soaking or spin coating the substrate with Fe, Co, or Mo nitrate or acetate salt and then drying the sample. Sputtering or evaporating a thin layer of catalyst material on the substrate and then subsequently breaking up the catalyst into nanoparticles using a pretreatment of H₂ plasma before introducing the carbon feedstock gas for CNT growth. This method has been used extensively and a correlation between the deposited layer thickness and resulting CNT diameters, thicker layers result in larger diameters, has been documented [33], [29]. The pretreatment time and power, however, must be determined for any given thickness.

Contrary to the relationship between catalyst layer thickness and CNT diameter, a longer pretreatment time does not always result in smaller particle sizes. Recently,

Amama *et al* reported that due to Ostwald ripening, pretreatment for too long will result in a lower CNT yield [34]. Ostwald ripening is a phenomenon related to strain energy that results in small particles shrinking and disappearing over time while large particles increase in size. The Ostwald ripening effect is clear from Figure 17 where a 5 min pretreatment has resulted in fewer and larger particles than the 30 s pretreatment. Nessim *et al* increased the MWCNT density yield by an order of magnitude by tuning the pretreatment process, including time and gas composition [35]. The control afforded by these catalyst deposition methods is limited to photolithographic methods for designating relatively large areas ($> 1 \mu\text{m}$) where CNTs can grow. The CNT distribution and diameter is also only moderately controllable through pretreatment methods. Sub-micron patterning methods that have proven successful for CNT fabrication are discussed below in Section 2.6.

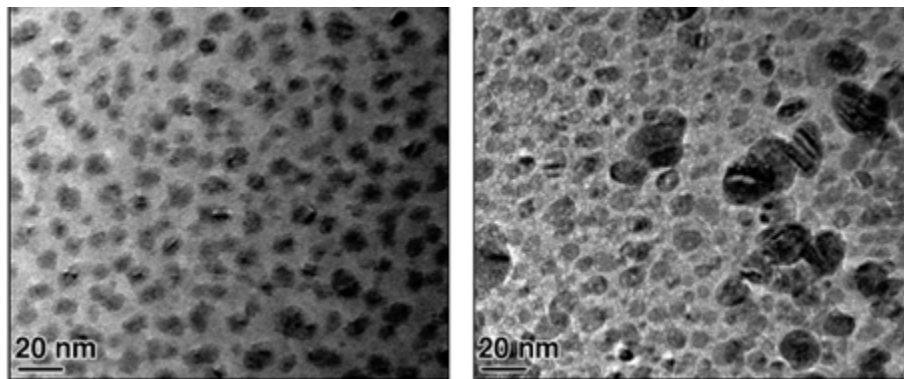


Figure 17. TEM images of a) 30 sec pretreatment and b) 5 min pretreatment [34]

The pretreatment and growth process as indicated above is also dependent upon the gas composition, flow rate, and pressure. PE-CVD systems use relatively low pressures ranging from 10 – 300 Torr [29]. Lower pressures reduce the presence of residual gases allowing for more process control. Flow rates depend upon the chamber pressure and gas

composition, but recipes reported in the literature range between 100 sccm and 400 sccm total gas flow rate. The gas flow rate can affect the plasma location within the chamber, so the location of the gas inlet will also determine the total gas flow rate.

Gas composition also varies greatly from process to process. Pretreatment recipes consist of pure H_2 , or some combination of H_2 and Ar. However, recent studies have indicated trace amounts ($< 1\%$) of water (H_2O) or nitrogen (N_2) can significantly improve pretreatment effects resulting in greater density and smaller diameter of catalyst particles [34], [36]. During growth, the gas composition can be even more complex consisting of a carbon feedstock such as but not limited to CO, CH_4 , or C_2H_4 , diluted in H_2 , Ar, N_2 , He, or some combination. Many different working compositions are possible, but Nessim *et al* concluded the carbon feedstock gas must be greater than 6% of the gas composition to provide enough carbon stock for CNT growth [35]. Gas compositions usually contain between 10% and 40% feedstock gas. Amorphous carbon, a common unwanted by-product, is more reactive than CNTs which has led to the use of trace amounts of oxidizers such as oxygen (O_2), H_2O , and hydroxide (OH) and the use of ethanol (C_2H_5OH) as a feedstock gas with very promising results [12].

2.5. Carbon Nanotube Growth Mechanisms

Carbon nanotube growth occurs in one of two places and via one of two methods at each location. The type of growth, gas phase or substrate, depends upon the location of the catalyst particle. When the catalyst and CNT formation occur in the chamber atmosphere, it is gas phase growth [12]. The more common substrate growth occurs

when the catalyst is deposited on the substrate. Both types of CNT growth rely on either surface carbon diffusion or bulk carbon diffusion as the actual growth mechanism.

Surface carbon diffusion is thought to be the growth mechanism for low temperature synthesis methods. The metal catalyst remains solid throughout the growth process and the “cracked” carbon from the feedstock gas diffuses around the particle surface. The carbon nanotube nucleates around the side of the metal particle. Since there is an abundant source of carbon from the feedstock gas, carbon continues to break down on the catalyst, diffuse around the particle, and facilitate nanotube growth [12].

In bulk carbon diffusion the catalyst can be either a solid or liquid nano-droplet depending on the transition metal and process temperature. The “cracked” carbon feedstock gas is dissolved by the catalyst until saturation at which point a carbon nanotube forms on the outer surface. This is a vapor – liquid – solid transition, where the feed stock gas is broken down into a hydrocarbon vapor, then forms a metal-carbon liquid when dissolved by the catalyst, and finally transitions to a crystalline carbon solid in the form of a nanotube [12].

Substrate growth via surface carbon diffusion is the most likely growth type and mechanism for PE-CVD methods. This stems from the goals of most PE-CVD growth methods which is to keep the temperature low to facilitate more substrate options and the use of deposited catalysts for controlled growth. Regardless of the growth mechanism substrate growth can occur at either end of the nanotube. If the stiction of the catalyst particle to the substrate is sufficiently large the particle will stay adhered to the substrate and the CNT will form via base growth. Tip growth occurs when the catalyst particle has

insufficient stiction. In this case, the CNT adheres to the substrate and the catalyst forms the tip of the growing CNT. Figure 18 illustrates both substrate growth conditions. While both base and tip growth have been observed with SWCNT and MWCNT fabrication, tip growth is dominant in MWCNTs and base growth is dominant in SWCNTs [12].

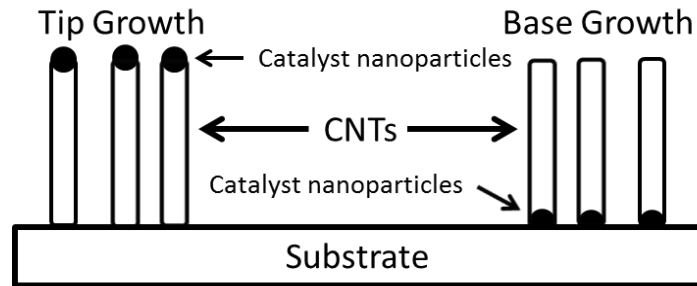


Figure 18. Schematic of carbon nanotube base growth and tip growth from a substrate [12]

In theory, CNT growth should be capable of continuous growth as long as the feedstock carbon gas is supplied. In reality, there are a number of conditions that can occur and impede or prematurely terminate the growth process. Growth can only occur at the catalyst; base growth can be slowed and even stopped due to slow or a lack of diffusion of carbon down to the nanoparticle. The carbon feedstock gas supplies an overabundance of carbon sometimes causing the deposition of amorphous carbon which can coat the catalyst and subsequently stop CNT growth. Occasionally, the catalyst can form graphitic shells instead of a carbon nanotube which will block access to more carbon ending the growth process [12]. These are causes of poor growth conditions and can usually be avoided by adjusting the growth parameters.

2.6. Sub-micron Patterning for CNT Synthesis

Pretreatment of a catalyst layer with temperature and plasma energy is successful in creating nanoparticles for CNT growth. The process can be adjusted to a point, but the nanoparticle distribution and sizes are random and dispersive. Thus, due to the correlation of CNT diameter to particle diameter, the CNTs are randomly distributed and have equally dispersive diameters. To address these issues, some unique approaches have been used to place catalyst nanoparticles at desired locations to achieve a specific diameter of CNT. The most successful method reported has been the use of e-beam lithography. Teo *et al* used e-beam lithography to deposit 100 nm Ni catalyst dots at a 10 μm pitch creating the separated array of vertically aligned single MWCNTs shown in Figure 19. The Ni dots were 100 nm in diameter and 7 nm tall. After a 700° C annealing before CNT growth, the diameter of the CNTs was 49 nm with a standard deviation of 2 nm [37]. E-beam lithography clearly provides the control necessary to engineer the size and location of individual CNTs.

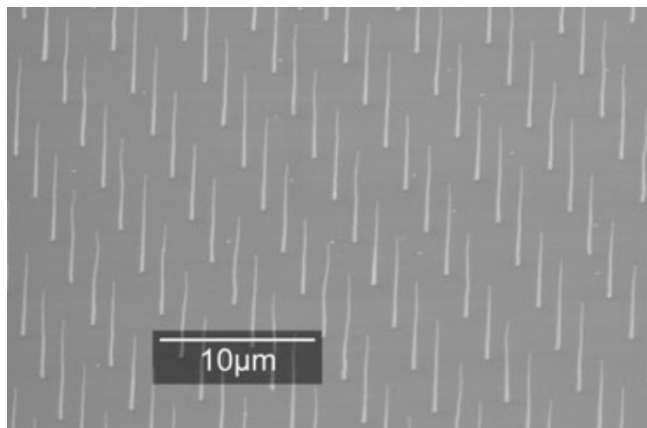


Figure 19. SEM image of single MWCNT array grown on 100 nm Ni catalyst [37].

Lin *et al* recognizing the expenses associated with e-beam lithography developed a method for nanometer scale patterning using an atomic force microscope (AFM) [38]. A Ni catalyst layer was patterned via oxidation by negatively biasing the AFM tip. The non-oxidized Ni was then removed using a wet etchant followed by CNT growth. $4\text{ }\mu\text{m} \times 4\text{ }\mu\text{m}$ arrays were successfully populated with MWCNTs and Figure 20 (a) shows patterned nano-dots with diameters of 81, 62, 47, 33, and 27 nm for each row from top to bottom with Figure 20 (b) showing the resulting individual MWCNTs [38]. Some of the smaller nanoparticles did not facilitate CNT growth. This is considered an issue with the growth parameters and not with the patterning process or resulting nanoparticle.

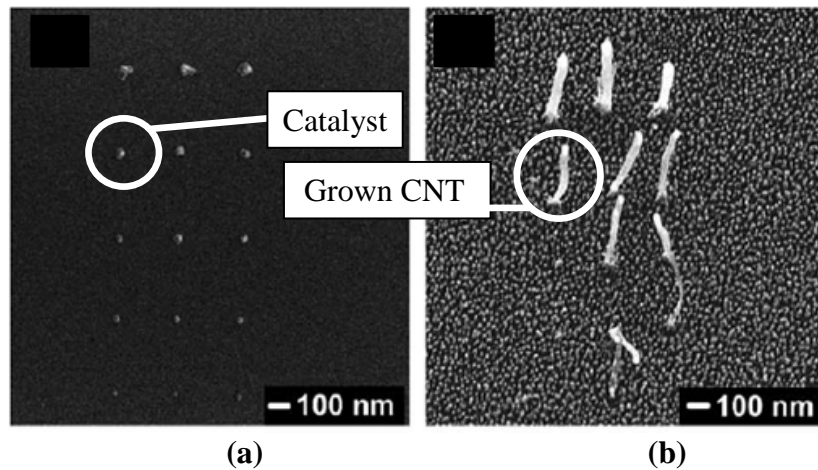


Figure 20. SEM images of a) AFM patterned catalyst nanoparticles and b) individual MWCNTs grown from the nanoparticles [38].

Nanosphere lithography has also been used successfully to control the diameter of fabricated CNTs [39]. Nanosphere lithography takes advantage of the self-assembling properties of polystyrene (PS) colloids. The colloids are available in diameters from $>10\text{ }\mu\text{m}$ down to 25 nm. Using the surface tension of water adjusted with a dodecyl sodium sulfate solution, the colloids pack together on the surface of the water into large uniform

monolayers. The monolayer is then transferred to the desired substrate, see Figure 21 (a), where it acts as a mask. Ni is then evaporated onto the substrate and the PS layer dissolved in toluene. The result is the uniformly distributed Ni triangles shown in Figure 21 (b). The size of the Ni nanoparticles, which in turn determines the diameter of the CNTs, is controlled by the size of the PS spheres. PS with diameters of 0.5 μm and 1 μm resulted in CNT diameters of 50 nm and 100 nm respectively [40].

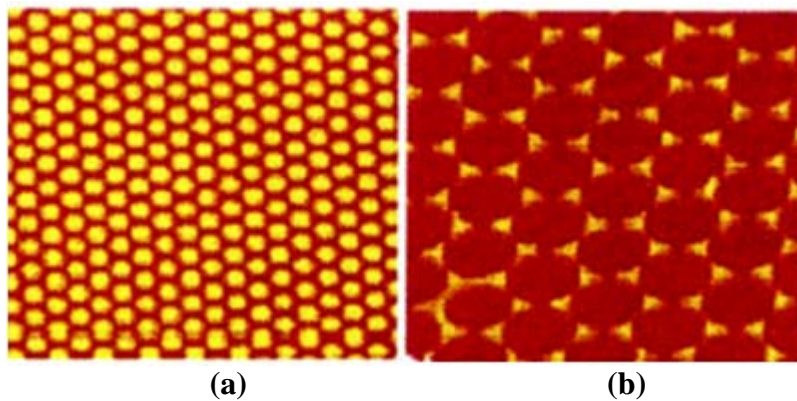


Figure 21. (a) AFM image of 0.5 μm PS monolayer and (b) AFM image of Ni catalyst particles after PS mask is removed [39].

An anneal performed at 900° C for one hour was used to turn the Ni triangles into spheres in preparation for CNT growth via PE-CVD. The resulting CNT arrays are shown in Figure 22 with the 100 nm CNTs on the right and 50 nm CNTs on the left as grown from the corresponding 1 μm and 0.5 μm PS masks [40]. Figure 22 displays the fairly sparse arrays of uniform diameter CNTs that are the product of this type of nanosphere lithography.

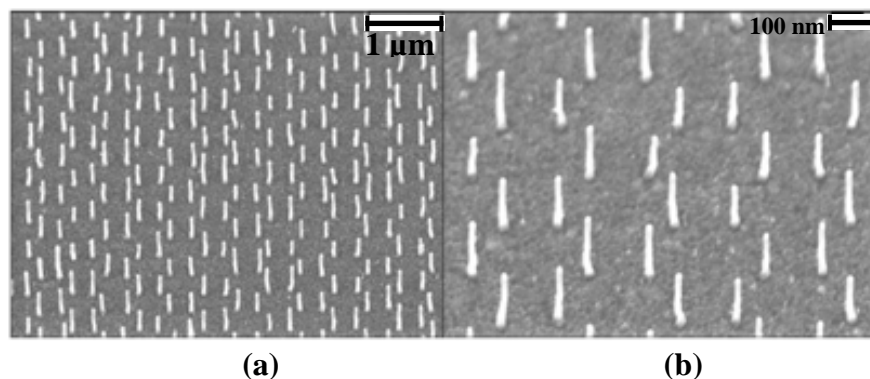


Figure 22. SEM images of CNT arrays resulting from 0.5 μm (a) and 1 μm (b) PS spheres [40].

Recently, another form of self-assembly masking method was developed to increase both CNT growth density and diameter uniformity. Lee *et al* make use of block copolymers, covalently linked but chemically distinct polymers, that allow separate chemical processes after deposition. Specifically, an asymmetric block copolymer of polystyrene and poly methyl methacrylate (PMMA) was used according to the process shown in Figure 23 [41]. The PMMA self-assembles into cylinders with a 34 nm diameter and center to center separation of 72 nm. The polystyrene, covalently bonded to the PMMA, fills the area between cylinders. The block copolymer is spin coated onto the

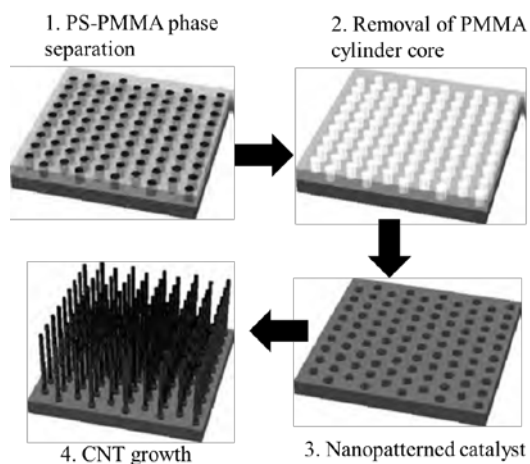


Figure 23. Block copolymer nanopatterning process [41].

substrate and cured at 190° C for 72 hours. Exposure to UV radiation and wet etch in acetic acid removes the PMMA cylinders leaving a uniform polystyrene mask. A 7 nm layer of Ni catalyst is evaporated onto the substrate. Lift-off is accomplished by dissolving the PS mask in toluene.

The catalyst particles deposited using the block copolymer nanopatterning increased areal density by an order of magnitude from 10^9 cm^{-2} to 10^{10} cm^{-2} and diameters decreased and became much less dispersive, see Figure 24 (a), when compared to catalyst particles created from typical pretreatment methods. As would be expected, Figure 24 (b) shows the CNTs grown via nanopatterning improved similarly to the catalyst particles [41]. Block copolymer nanopatterning improves control of key CNT fabrication parameters, however, the excessive processing time may be a deterrent to wide spread adoption.

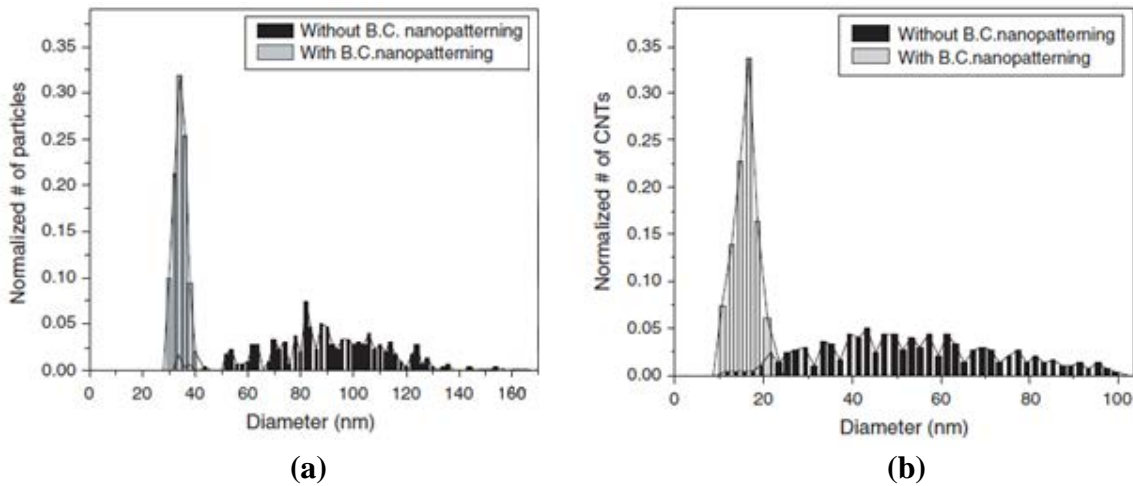


Figure 24. Statistical diameter distribution of catalyst particles (a) and CNTs (b) with and without block copolymer (B.C.) nanopatterning [41].

The capability to pattern and control the diameter of CNTs is crucial for most applications. While e-beam lithography is very effective, it is much too expensive and

time consuming to facilitate commercial fabrication of CNTs. Thus, new novel nanopatterning methods are continually being researched and developed constantly, in an effort to find an inexpensive, commercially viable process.

2.7. Field Emission

In 1995, only four years after carbon nanotubes were introduced to the scientific community by Iijima, de Heer *et al* demonstrated the field emission capabilities of carbon nanotubes [42]. They fabricated a small electron gun from a 1 mm diameter MWCNT film with an extraction grid 20 μm from the film. The electron gun was capable of producing current densities of 100 $\mu\text{A}/\text{cm}^2$ at a voltage of 200 V. At 700 V, the current densities were greater than 100 mA/cm^2 . The Fowler-Nordheim model for the tunneling of electrons through a metal-vacuum potential barrier was used to validate the field emission currents. These results spawned a flurry of research into the field emission capabilities of carbon nanotubes that has only increased in intensity over the ensuing 14 years.

2.7.1. Fowler-Nordheim Model and Field Enhancement

The Fowler-Nordheim (FN) model describes the current or current density obtained from electrons tunneling through a metal-vacuum potential barrier at 0 K [2]. Other conditions for the Fowler-Nordheim model include tunneling from a flat metal surface; the metal or emitter is modeled as a free electron gas; and the potential barrier height is independent of the applied voltage [7]. Although the actual potential barrier is a combination of the image force potential and the external force potential as shown in

Figure 25 (a); typically a simplifying triangular barrier, shown in Figure 25 (b), is used instead [7].

The simplified, but correct, FN equation for current density from field emission is shown below [43].

$$J = \frac{aF^2}{t^2(y)\phi} e^{\left(\frac{-b\phi^{3/2}}{F}v(y)\right)} \quad (12)$$

Where current density, J , is in A/cm^2 , a and b are constants of $1.54 \times 10^{-6} \text{AV}^{-2}\text{eV}$ and $6.83 \times 10^7 \text{eV}^{-3/2}\text{Vcm}^{-1}$, $t(y)$ and $v(y)$ are tabulated functions, F is the applied electric field, and ϕ is the work function. The function $t(y)$ is close to and so often set equal to unity. The Nordheim function, $v(y)$, varies significantly; however, in what is considered an improper or gross simplification $v(y)$ is also commonly set to unity [44].

The applied field is adjusted to account for the sharp tip of carbon nanotubes by including a field enhancement scale factor β . The field enhancement factor takes into

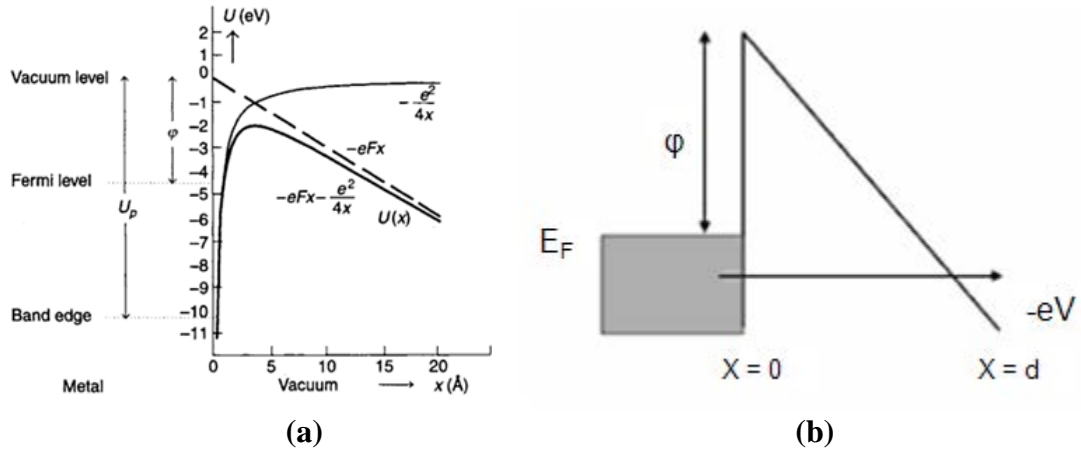


Figure 25. a) Metal--Vacuum potential barrier ($U(x)$), accounting for the image force ($-e^2/4x$) and external applied voltage ($-eFx$) [43]. b) Triangular potential barrier approximation, E_F is the Fermi level, V is the external applied voltage, and ϕ is the metal work function [7].

account the microscopic or localized field at the emitter tip. Electric field lines concentrate at the area of small radius of curvature resulting in much higher localized field potentials. The applied field F , is considered a uniform field such as between two parallel plates and is defined below:

$$F = \frac{V}{d} \quad (13)$$

where V is the applied voltage and d is the separation distance as shown in Figure 25 (b). The inclusion of the enhancement factor gives the localized field shown in Equation (14).

$$F_{Local} = \frac{\beta V}{d} \quad (14)$$

Field enhancement for field emitting CNTs has a wide range of reported values from 1000 to 8000 and even as high as 26000 [3], [45]. Issues with determining field enhancement will be discussed below.

Including the simplifications mentioned above, the field enhancement factor, and converting from current density to current by including the total emission area the following FN current relationship is obtained:

$$I \approx \frac{aS\beta V^2}{d^2\phi} e^{\left(\frac{-bd\phi^{3/2}}{\beta V}\right)} \quad (15)$$

where S is the emitting surface area in cm^2 . By dividing by V^2 and taking the natural log Equation (15) takes the form:

$$\ln\left(\frac{I}{V^2}\right) \approx -\frac{bd\phi^{3/2}}{\beta V} + \ln\left(\frac{Sa\beta^2}{d^2\phi}\right) \quad (16)$$

Equation (16) is easily recognized as the equation of a line for $\ln(I/V^2)$ as a function of $1/V$. Thus, FN field emission can be shown if a line results from plotting measurements of emission current as a function of the applied voltage in the form $\ln(I/V^2)$ versus $1/V$. This is often referred to as a Fowler-Nordheim plot and is used to demonstrate field emission as opposed to thermionic emission. Figure 26 shows the Fowler-Nordheim Plot of two CNT carpet samples grown via MPE-CVD at AFIT.

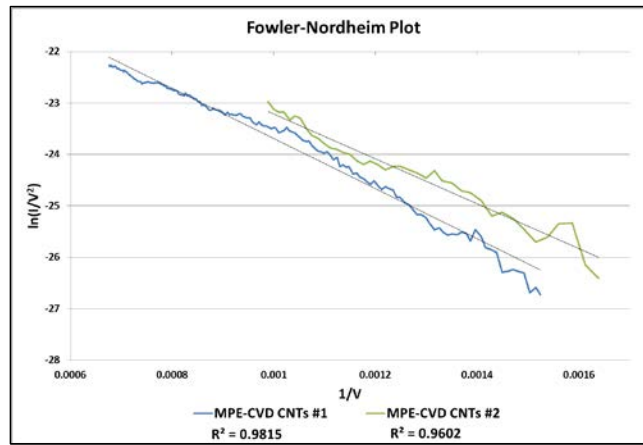


Figure 26. Fowler-Nordheim plot showing experimental results with fitted line.

The slope of the FN plot, given in Equation (17), can be used to determine the field enhancement factor, β . There is one caveat to this method of calculating the enhancement factor: the work function of the CNTs must also be known. Initially, the work function was unknown and a constant work function of 5 eV was used [42]. Since then, there have been several methods employed to measure the work function of CNTs. Ultraviolet photoemission spectroscopy was used to measure the work function of SWCNT bundles at 4.8 eV, while other reported values ranged from 4.3 eV to 5.7 eV [47].

$$m = \frac{bd\varphi^{\frac{3}{2}}}{\beta} \quad (17)$$

Xu *et al* used a transmission electron microscope with a unique tungsten needle sample holder measured the work function of individual MWCNTs grown via MPE-CVD. The measurements indicated differences in the physical structure at the tube tips caused variations in the work functions from 4.51 eV to 4.78 eV [48]. These values 4.5 - 4.8 eV have been adopted to estimate the field enhancement in more recent publications. Only MWCNTs are considered in this study as well, so a work function of 4.65 eV is used in all calculations. Thus, for MWCNT samples #1 and #2, shown in Figure 26, the resulting field enhancement factors are 2390 and 3460 respectively. A higher β is indicative of more efficient field emission. The increased localized electric field results in field emission at lower applied voltages.

With all the assumptions and simplifications listed, it is obvious the FN model is not completely accurate for field emission from CNTs. However, many experimental and theoretical efforts to develop an accurate model have yet to produce a conclusive result; while the FN relationship given above has been proven experimentally to be a good fit for I-V characteristics of CNT emitters of all kinds [7]. The sheer number of methods and processes used to achieve emission and the often seemingly contradictory results of different research efforts have made a functional model for electron emission from carbon nanotubes a difficult and elusive task.

2.7.2. Carbon Nanotube Field Emission

As previously documented, CNTs have many unique properties ideal for field emission. Carbon nanotubes make excellent electron emitters, not because of a low work function, but due to the extremely high local electric field that forms at the small diameter tips. Single walled CNTs have diameters from 0.6 nm to 1.4 nm and multi-walled CNTs can range from 12 nm to more than 100 nm in diameter. Both types of CNTs can range from tens of nanometers to microns and even millimeters in length resulting in incredible aspect ratios. The resulting focus of the electric field at the tips of the CNTs is often referred to as the electric field enhancement factor discussed above in Section 2.7.1. Previous research as summarized by Bonard *et al* has shown multi-walled CNTs to be more robust emitters than single walled CNTs [49]. Thus, only multi-walled CNTs are grown in this field emission effort. While the conductivity of single walled CNTs can be metallic or semiconducting depending on the nanotube structure, all multi-walled CNTs are considered metallic conductors because some of the nested nanotubes making up the multi-wall CNT will be metallic. This makes attempts to control or consider the chirality or type of CNTs grown unnecessary; another benefit of using MWCNTs for field emission instead of SWCNTs.

Potential commercial applications are the driving forces behind CNT field emission research. Different applications lead to different requirements, however, there are a few figures of merit that can be used to assess the relative quality of a CNT emitter. Current density is the value most often given when reporting results of CNT field emission research. Current density without knowing the associated electric field is of little use.

The area used to calculate current density is also important. The current density from a single CNT can be remarkably high, basing the potential emission from an array of nanotubes on a single CNT has led to current density predictions as unfathomably high as 10^7 A/cm^2 [50]. But, due to screening effects, getting every CNT in a large area to emit electrons has proven to be a much more difficult task making current density measurements of individual CNTs useless in predicting the field emission from large areas of CNTs.

Commercial applications for field emission start at current densities around 10 mA/cm^2 for flat panel displays [50]. As an emission cathode for space craft electronic propulsion neutralization the total current and emission efficiency is more important than the current density, however the requirement for all space applications is generally smaller is better, current densities greater than 50 mA/cm^2 would greatly reduce scaling [51]. But the Brusek Co CNT based cathode at half an inch and sustained output of 1 mA appears to have a current density of 0.2 mA/cm^2 . For microwave electronics, the current density needs to be at least a sustained 1 A/cm^2 to be competitive with the thermionic cathodes currently used [52].

Other important parameters that aid in comparing results are the turn-on field, E_{to} , threshold field, E_{th} , configuration (diode vs triode) and the corresponding dimensions, and the total emission current. The turn on and threshold fields, much like diodes and transistors, are the fields required to achieve a given current density. Bonard *et al* performed a survey of CNT field emission research in 2000; the results are shown in Table 1. They used $10 \mu\text{A/cm}^2$ for E_{to} but there is no standard for turn on values so

researchers often don't report them or don't use the same current densities to represent turn on. A current density of 10 mA/cm^2 for E_{th} is typical, but not always recorded in the literature [49].

Table 1. Bonard *et al* collected data on field emission from CNT films or arrays, see [49] for references to individual data sources [49].

Emitter	d (μm)	S (cm^{-2})	E_{to} (V/ μm)	E_{thr} (V/ μm)	J_{max} (A cm^{-2})	Remarks
MWNT	10–40	0.002	n.a.	<25*	1	Very dense “tubulene” film
MWNT	15	0.003	n.a.	~15*	10	Very dense “tubulene” film
Arc MWNT	20	0.008	n.a.	20*	0.1	
Arc MWNT	30	0.007	4.0	6.5		
Arc MWNT	125	0.07	2.6	4.6		
Arc MWNT	125	0.07	1.1	2.2		Purified sample with closed caps
Arc MWNT	20–100	2.5×10^{-5}	7.5*	10*	0.4	Open tubes dispersed in epoxy
Arc MWNT	80	0.025	0.9*	4*		O ₂ plasma treated tubes dispersed in epoxy
Arc MWNT	200	0.02	n.a.	1.5		Tubes dispersed in epoxy
SWNT	125	0.07	1.5	3.9		
SWNT	10–300	0.002	n.a.	4–7	4	
SWNT	150	3.1	2.1*	n.a.		
CVD MWNT	n.a.	0.001	1.7*	n.a.		
CVD MWNT	70	n.a.	n.a.	4.8–6.1		Aligned MWNTs, 15 emitters
CVD MWNT	150	3.1	n.a.	2.1*		Large amount of graphitic fragments
CVD MWNT	n.a.	0.0003	4.8	6.5	0.1–1	
CVD MWNT	600	0.07	n.a.	≥ 5		
CVD MWNT	150	0.2	3	6.6*		Si substrate
CVD MWNT	500	0.1	1.6	5*		Steel substrate
CVD MWNT	500	0.1	3	5.6*		Ni substrate
CVD MWNT	10–300	0.002	0.75	1.6	1–3	Catalyst supplied in gas phase
Graphitic fibers	300	1–10	2.1	n.a.	0.2	

d is the interelectrode distance, S the emission area, E_{to} and E_{thr} are the turn-on and threshold fields needed to produce an integrated current density of $10 \mu\text{A/cm}^2$ and 10 mA/cm^2 , and J_{max} is the maximal current obtained without destruction of the emitter. n. a. means that the value is not indicated or could not be deduced from the figures, and * indicates that the value was estimated or extrapolated from the presented data.

CNT field emission is achieved via two basic configurations, diode and triode, both shown in Figure 27. The diode configuration is often used for its simplicity and out of necessity, because many CNT fabrication techniques are not compatible with a triode type set-up. Field emission from a diode based device requires relatively high voltages to establish the necessary electric fields, due to the large distance, d , between the CNT

cathode emitters and the anode. Triode based devices allow for much lower voltages by locating a gate structure close to the cathode, typically within a few microns. The triode set up makes controlling or modulating field emission simpler due to the low voltage gate controlling emission.

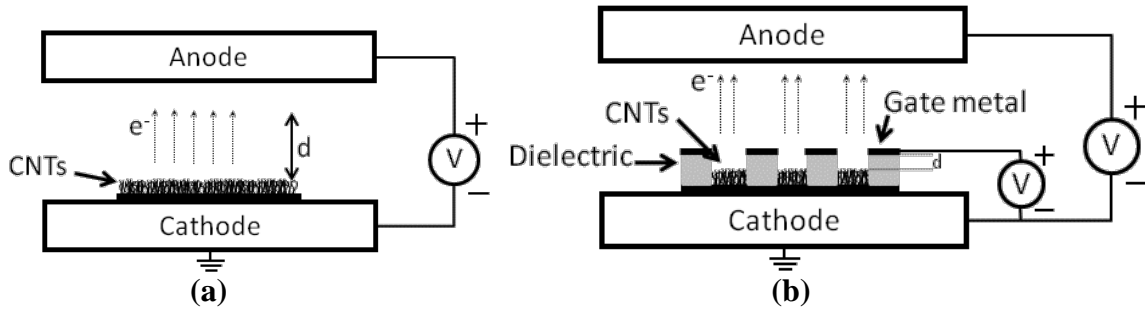


Figure 27. Schematic of a) diode and b) triode configurations for field emission.

Direct comparisons between different CNT field emission efforts are difficult as can be seen by trying to distill some meaningful conclusions from the data collected by Bonard in Table 1. This represents only a small fraction of the literature reporting on field emission effects over the first five years through 2000. Some conclusions and trends that Bonard *et al* recognized include [49]:

- The density of a CNT film affects field emission. A comparison showed that very low density films and very high density films performed much worse than a “medium” density film.
- Field emission from CNT films tends to degrade overtime. The exact cause is unknown, but residual gasses and current density have significant effects on degradation
- SWCNT films tend to degrade up to 10 times faster than MWCNT films. Individual CNT emitters, both multi-wall and single wall, fail abruptly and irreversibly.
- Study of individual emitters showed clear evidence of non-Fowler-Nordheim emission.

A brief survey of field emission efforts since 2000 shows the results of these conclusions. Table 2 details the measurements of a small sample of the field emission efforts since 2000 and the most noticeable trend is that almost all CNT films or arrays researched for field emission are multi-walled. This is driven by two factors, first CNT field emission devices are reaching commercialization which means lifetime is of the utmost importance and, as noted above, MWCNTs degrade much slower than SWCNTs. Second, commercialization also requires easy, inexpensive, and reproducible fabrication techniques like MWCNT synthesis via any number of CVD methods. Another trend not reflected in the data displayed in Table 2 is the orientation of the CNT emitters. Even though field emission has been demonstrated in randomly aligned and even horizontally aligned CNTs, it is generally accepted that vertical alignment results in better field enhancement resulting in lower field strengths [10]. All the efforts recorded in Table 2 use vertically aligned MWCNTs grown by some manner of CVD.

Table 2. Survey of reported CNT field emission since 2000.

Ref.	Emitter	d (μm)	S (mm^2)	E ($\text{V}/\mu\text{m}$) to/max	J_{max} (A/cm^2)	$\sim\beta$	Year
[53]	MWCNT	60	0.04	<1/3.2	0.3		2001
[54]	MWCNT	1	30	<1/5.5	17		2004
[55]	MWCNT	15	0.03	1.25/4	1.8	4250	2005
[56]	MWCNT	2	10 μ	16.5/23	0.0012		2005
[52]	MWCNT		0.25	6.5/16.5	1.0		2006
[3]	MWCNT			<4/8	1.8	7588	2007
[57]	MWCNT	1000	0.002	<2/2.9	2.8	2500	2007
[58]	MWCNT	1000	12	\sim 0.1/0.15	0.010	>1000	2008

In his seminal publication, de Heer estimated a mere 0.1 % of the total CNTs were emitting [42]. They concluded only a tiny fraction of CNTs was sharp enough to be efficient emitters. Since then, the phenomenon has been attributed to electrostatic

screening effects [7]. Nilsson *et al* conducted a study in screening effects by first performing 2D electrostatic simulations of field penetration between CNTs separated by different distances, visualized in Figure 28 [59]. The reduction in penetration as the CNTs are placed closer together reduces the field enhancement reducing the localized field. Nilsson *et al* posited that the closer the CNTs are packed the flatter they appear with no separation between tubes being equivalent to flat metal. Using these simulation results and corresponding experimental data between low, medium, and high density field emission arrays; an optimized separation distance of twice the height was determined [59]. Milne *et al* achieved this optimized height to separation using e-beam lithography to deposit 100 nm Ni dots over a $500 \times 500 \mu\text{m}^2$ area [52]. The resulting grid, shown in Figure 19, contains $5 \mu\text{m}$ tall MWCNTs with a separation pitch of $10 \mu\text{m}$. The array produced a sustained current of 2.5 mA or a current density of 1 A/cm^2 .

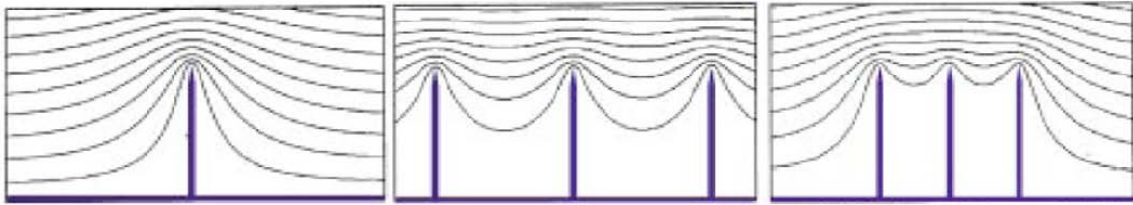


Figure 28. Simulation of field penetration [59].

Suh *et al* followed the Nilsson research with an experimental study in which the separation distances between an array of MWCNTs was fixed and the CNT heights were varied [60]. An optimized height to separation distance was obtained that differed from the Nilsson *et al* results. They concluded that screening effects are not the only factor involved in the optimizing of height and separation. As the height of the CNTs increases, the aspect ratio increases, improving the field emission efficiency. There is a tradeoff between the increasing height of the CNTs and the screening effects of nearest neighbors

that results in a maximum field enhancement at a separation equal to the height of the CNTs or half the distance that Nilsson *et al* predicted [60].

Recently, Smith and Silva, conducted 3D simulations of CNT arrays to determine screening effects and optimized height to separation distance [61]. The 3D visualized contour plots of the local electric field of an 11 by 11 CNT array with a separation distance equal to height in Figure 29 clearly show the internal CNTs have smaller localized fields. The outer most CNTs have localized fields 35% greater than the internal CNTs. Running a series of different simulations varying the separation distance from 0.3 to 5.3 times the CNT heights lead to two new conclusions. First, Nilsson *et al* had underestimated the effects of screening with their 2D simulations. Instead of a separation distance of two times the height; a separation distance of five times the height is necessary to avoid screening effects. Second, much like Suh *et al* found experimentally, there is a trade-off between screening effects and emission efficiency. Smith and Silva arrived at an optimized field emission array with an inter-nanotube separation of three times the CNT height [61]. To date, no experimental data is available on an actual CNT array optimized in this fashion.

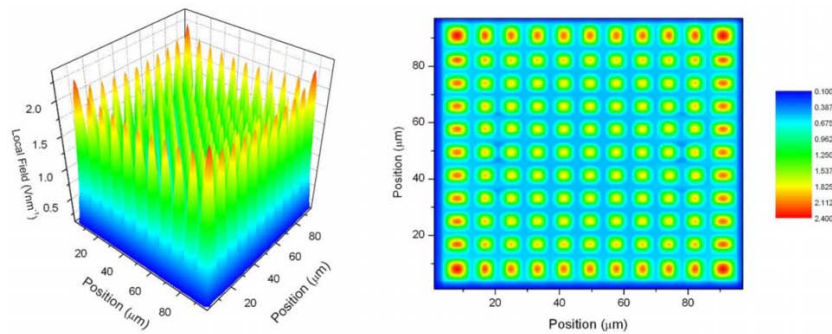


Figure 29. Contour plots of local electric field of 11 x 11 CNT array with inter-nanotube distance equal to height [61].

Fabrication and testing of MWCNT bundles for field emission has led to completely contradictory results to all three CNT array optimizations discussed above. Manohara *et al* fabricated arrays of MWCNT bundles via thermal CVD on silicon substrates [55]. The individual CNTs had lengths of $50 \pm 2 \mu\text{m}$ and diameters from 10 – 20 nm. When the Fe catalyst was patterned into arrays of dots ranging from 0.2 μm to 5 μm , it was found that the CNTs would form rope like bundles for the dots greater than 0.5 μm . These bundles were grown in 0.5 x 20 mm arrays with inter-bundle spacing ranging from 2 – 100 μm . Figure 30 shows a 5 μm diameter bundle array with 2 μm inter-bundle spacing.

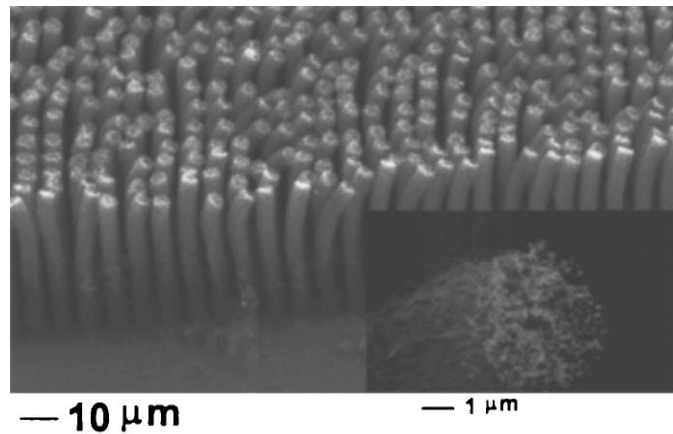


Figure 30. SEM of 5 μm diameter bundle array with inter-bundle spacing of 2 μm . Inset is a close up view of a single bundle tip [55].

After completing field emission tests across all the arrays and correlating the data, Manohara *et al* found an optimized bundle diameter of 1 – 2 μm and inter-bundle spacing of 5 μm . Smaller and larger inter-bundle spacing resulted in significantly less, up to two orders of magnitude, emission current as did both smaller and larger bundle diameters [55]. While difficult to reconcile with the optimized individual CNT arrays given above

because the heights of the bundles are 50 μm compared to 5 μm inter-bundle spacing, it is interesting that both cases result in a similar optimization of a “medium” density.

Fujii *et al* published similar results for CNT bundles in 2007, confirming that arrays of CNT bundles have emission properties that don’t match individually spaced CNT arrays or densely packed CNT films. Large MWCNT pillars, 50 μm diameter and 70 μm tall, were fabricated on stainless-steel substrates using a multilayer catalyst (Fe and Al) via thermal CVD [57]. Five pillars were fabricated into an array shown in the inset of Figure 31. This effort did not include any testing of different pillar or array dimensions, however, the field emission tests proved the array was very effective. The array demonstrated low field operation with a threshold field of 2 V/ μm and a remarkable 2.8 A/ cm^2 at only 2.9 V/ μm . The corresponding Fowler-Nordheim plot showed an extremely close linear relation confirming field emission. The bundle array also exhibited no degradation over a 200 hour test operating at 150 mA/ cm^2 . Fujii *et al* performed 2D simulations of the electric field over a single bundle and produced similar

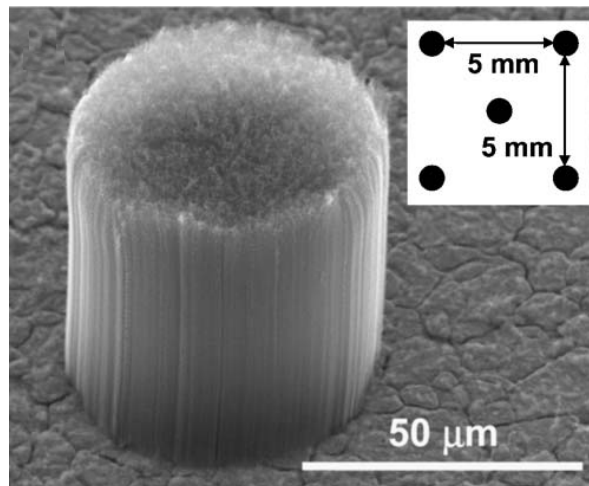


Figure 31. SEM of MWCNT bundle 50 μm diameter and 70 μm tall. Inset is schematic of 5 bundle array [57].

results to the 3D simulations of CNT arrays performed by Smith and Silva. The simulation showed an increase in the electric field of over 250% (4.2 to 15 V/ μm) from the inner area of the bundle to the outer edge. The cause of the increase was attributed to edge and screening effects. Although not experimentally verified, it was noted that this edge effect would cause emission to occur almost exclusively at the edges of each pillar. Clearly, there is much more to be learned about the field emission properties of CNT bundles and bundle arrays.

Triode based CNT field emission devices typically use conventional microelectronics or microelectromechanical systems (MEMS) based processes where structure layers are deposited and then etched to form specific features. The process shown in Figure 32 developed by Wong *et al* consists of standard fabrication steps with the exception of MPE-CVD growth of CNTs at the end. The SEM images in Figure 33 are of a single array element from the top (a) and in profile (b). The pretreatment process necessary before growth affects the catalyst in the open area more than the edges

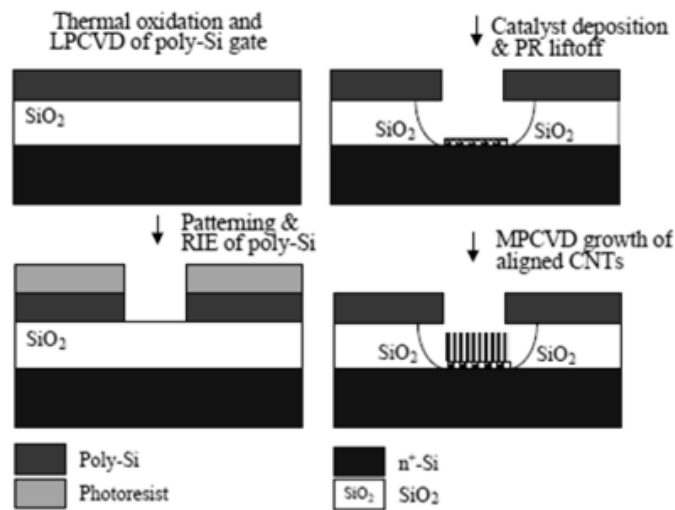


Figure 32. Triode based CNT field emission device fabrication process [56].

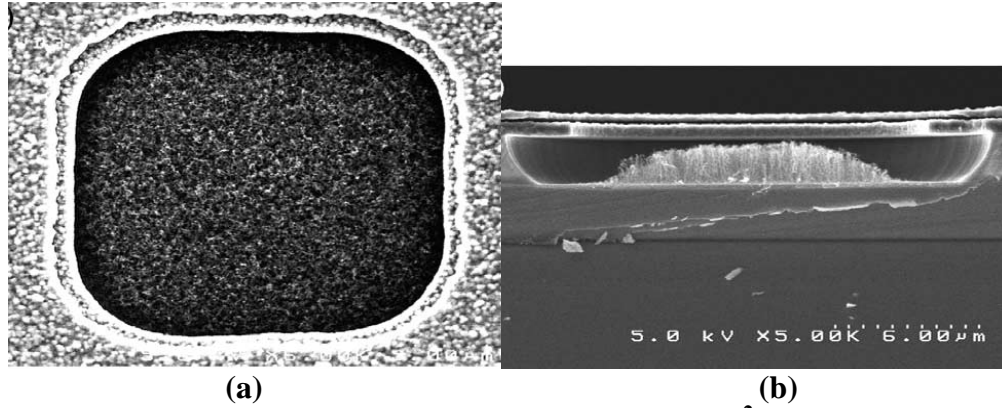


Figure 33. SEM images: (a) single $10 \times 10 \mu\text{m}^2$ pixel and (b) the corresponding profile [56].

resulting in a beneficial convex CNT growth clearly visible in Figure 33 (b). Stunted growth at the edges prevents electrical shorting with the gate, reduces screening effects, and increases device lifetime [56].

Nieman *et al* have reported a fabrication method that may allow devices to take advantage of the exceptional field emission properties of CNT bundles and the advantages associated with a triode configuration [62]. The process also demonstrates the remarkable strength of CNTs. Unlike most triode based devices, the integrated gate fabrication process begins with patterned CNT growth. MWCNT bundles 10 μm tall with 10 μm diameters are grown in arrays with 15 μm center-to-center spacing. Next the substrate and bundles are coated with an oxide layer of SiO_2 via CVD using tetraethyl orthosilicate (TEOS). Figure 34 (a) and (b) show a CNT bundle before and after oxide deposition.

A layer of Polyimide is spin coated on and fully cured; it will act as the dielectric layer for the finished device. The gate metal, Mo in this case, is deposited and patterned to form the gate openings over the oxide encased bundles. The patterned gate serves as the mask for subsequent oxide etch that removes the oxide coating from the CNT bundle.

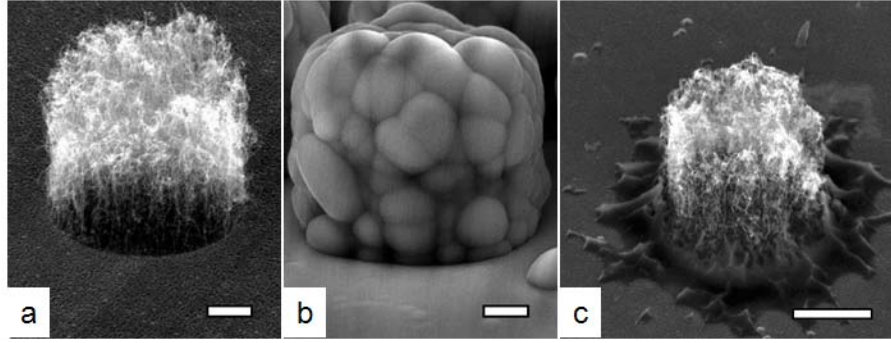


Figure 34. a) 10 μm diameter and height CNT bundle. b) CNT bundle coated with oxide layer. c) Released CNT bundle after oxide etch . Scale bars are 2 μm , 2 μm , and 5 μm respectively [62].

The entire array has yet to be fabricated, but a study was conducted on coating and releasing the CNT bundles. Figure 34 (c) shows an apparently unharmed CNT bundle after oxide etching. However, the analysis was based solely on SEM images, field emission data would need to be collected before and after the oxide process to determine if the CNTs are truly unaffected. The possibility of protecting CNTs with an oxide layer opens up new fabrication options that are not possible when CNT growth has to be the last fabrication step.

2.8. Summary

Carbon nanotube field emission devices have matured and improved as the understanding of their unique emission properties has increased and innovative methods of fabrication have evolved. This survey of recent literature documents the history and evolution of CNTs from an accidental discovery to an industry. The unique mechanical and electrical properties of CNTs were described in detail with particular emphasis placed on those properties that are conducive to field emission. Synthesis and growth mechanisms were explained and the specific growth methods used in this research effort are highlighted. Carbon nanotube patterning processes are reported along with the

processes applicability to large scale field emission arrays. Finally, recent field emission research was surveyed and the performance recorded for comparison with results of the current research effort.

III. Plasma Enhanced CVD Carbon Nanotube Synthesis

The first step to achieving carbon nanotube field emission array devices is to develop a reliable process for synthesizing CNTs. Of the many documented CNT synthesis methods, Chemical vapor deposition (CVD) synthesis occurs at low enough temperatures to facilitate silicon substrates. Two CVD processes, microwave plasma enhanced CVD (MPE-CVD), and thermal CVD (T-CVD), were developed to produce MWCNT films or carpets. The first, MPE-CVD, is explained in this chapter. The second process, T-CVD, is described in Chapter IV. Each synthesis method is described in detail to include substrate preparation, catalyst granulation, and the growth recipe.

Each step of the respective synthesis process and the resulting CNTs were characterized to develop an effective, reliable process for producing CNTs. The first step in characterizing each synthesis process is using scanning electron microscopy (SEM) to determine the size and spacing of the granulated catalyst nanoparticles. After CNT synthesis, the carbon nanotubes are characterized physically via Raman spectroscopy and SEM imagery. Raman spectroscopy provides a method to determine the quality of the CNTs. SEM micrographs are used to estimate CNT areal density, presence of amorphous carbon, and CNT physical characteristics such as diameter, length, and alignment.

3.1. MPE-CVD System

An Astex 1.5 kW MPE-CVD system was used for CNT Synthesis during this research effort. The MPE-CVD system is shown with components labeled in Figure 35. The system has been upgraded with a 600 V DC supply for stage bias, a new 1.5 kW

microwave plasma generator system with a three stub tuner for improved tuning control, a pyrometer for exact substrate temperature measurements, and new resistive heating stage and power supply.

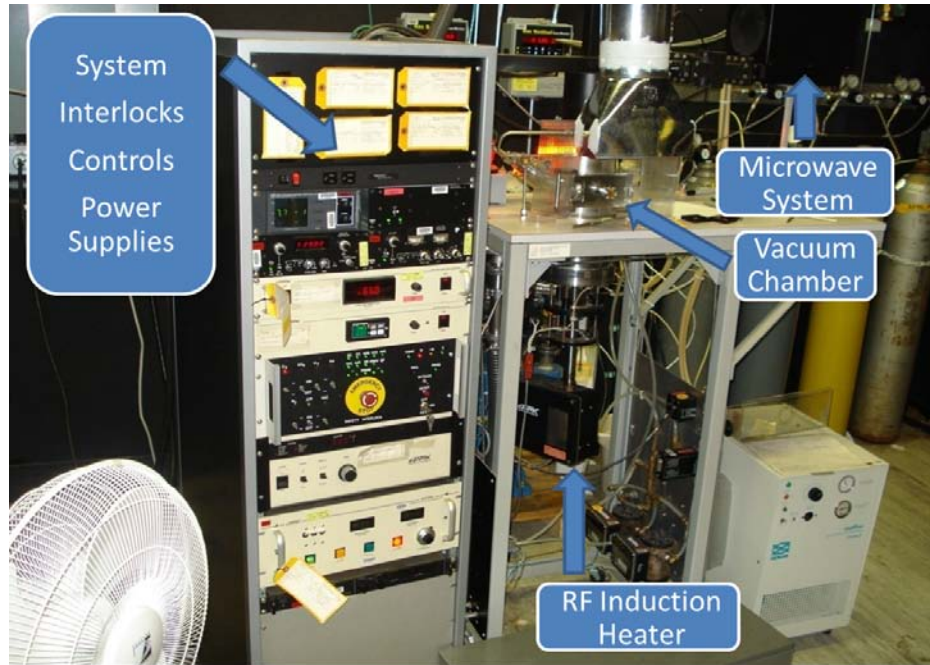


Figure 35. Astex MPE-CVD System [63].

3.2. Substrate Preparation

CNT growth via MPE-CVD requires nanometer sized catalyst particles for the CNT to nucleate around and form. Nickel and iron were used as catalyst materials; Ni with the MPE-CVD process and Fe with the T-CVD process. A hydrogen plasma pretreatment is applied to the Ni catalyst to granulate the layer into nanoparticles conducive to CNT growth. The most effective deposition method, catalyst thickness, and pretreatment time were determined by varying these parameters and analyzing the resulting catalyst nanoparticles and the resulting CNTs.

Samples were prepared with a titanium (Ti) layer 200 Å thick sputtered or evaporated onto an n-type silicon wafer [100] to act as an adhesion and diffusion barrier for the nickel catalyst layer and the subsequent CNTs. The nickel catalyst layers had thicknesses of 10, 50, 100, 200, 350, and 500 Å with samples of each thickness deposited by both e-beam evaporation and DC sputtering.

3.3. Physical Vapor Deposition

Physical vapor deposition (PVD) is the process of creating a vapor via physical means and depositing the vapor to form a thin film. There are a number of methods of physically creating a vapor. E-beam evaporation and DC sputtering were used for depositions in this research. Evaporation uses a thermal source to heat the target material to its melting point. The resulting vapor impinges on the substrate and, after reaching a condition of supersaturation, condenses forming a thin film [64]. The Sputtering process is facilitated by ions from a gas discharge plasma accelerated in an electric field. The electric field accelerates the ions towards the cathode, in this case the target material. The resulting collision and transfer of kinetic energy dislodges atoms from the target which then impinge on the anode, which is the substrate, forming the desired thin film [64].

Figure 36 shows AFM phase measurements of as-deposited sputtered and evaporated 100 Å Ni catalyst layers on a Silicon substrate with a 200 Å titanium barrier layer. The sputtered Ni clearly has larger grain sizes and more defined grain boundaries. Both evaporated and sputtered thin films are deposited in a condition of supersaturation which typically results in small grain sizes due to a high rate of nucleation [65]. With the

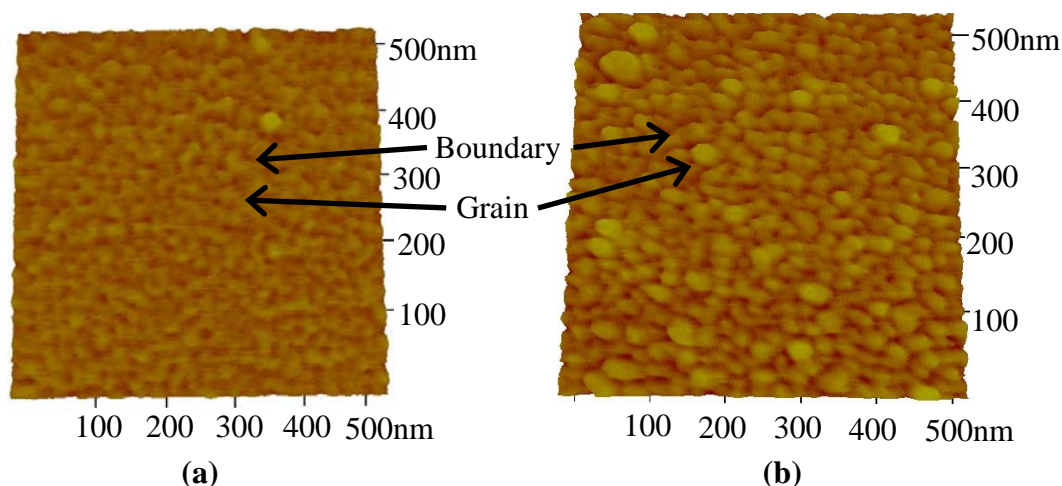


Figure 36. AFM image of as-deposited 100 Å of (a) evaporated Ni and (b) sputtered Ni.

exception of impurities which can cause compressive stress, evaporated films generally have tensile intrinsic stress [66]. Sputtered films on the other hand have been shown to have both compressive and tensile intrinsic stress with stress reversal occurring through control of many parameters such as ion mass, substrate temperature, target-plasma separation, and especially gas pressure. Sputtering at lower pressures typically results in compressive stress with tensile stress occurring at higher pressures. The reversal occurs between 1 – 10 mTorr [65]. The compressive stress has been attributed to shot-peening effects and possibly sputter gas incorporation. Radic *et al* demonstrated some control of the grain size of sputtered nanocrystalline nickel thin films. Average grain size was varied from 11 nm to 150 nm by changing the substrate temperature during deposition [67]. Thus, sputtered catalyst layers offer more control over the thin film properties than e-beam evaporation.

3.4. Hydrogen Plasma Pretreatment

Before CNT growth is possible; it is first necessary to pretreat the catalyst layer, a process that granulates the catalyst into the necessary nanometer size islands. The

catalyst nanoparticles are necessary for CNT growth and it has been shown that the diameter of the Ni nanoparticle corresponds closely to the diameter of the resulting CNT [68]. Using hydrogen plasma to granulate the Ni results in dispersed nanoparticle diameters, however, multi-walled CNTs can vary in diameter from less than 10 nm to 100 nm in diameter. The nominal goal for MWCNT growth for field emission applications is nanoparticles distributed around 50 nm or less.

The hydrogen plasma pretreatment was performed at 20 Torr with a substrate temperature of 400° C, an H₂ flow rate of 135 sccm, and microwave power at 400 W. The granulation and CNT growth processes were adapted from Wong *et al* [68]. A set of samples of each thickness and deposition method were pretreated for 3.5, 5, and 7 minutes. The results were analyzed using SEM images and AFM measurements and recorded in Table 3 below.

Ni layers of 10, 350, and 500 Å were processed, however, 10 Å proved to be too thin and no Ni was present after even the shortest pretreatment time. The thicker Ni Layers (350 and 500 Å) were too thick resulting in Ni islands much too large (>100 nm) to facilitate CNT growth. Both evaporated and sputtered samples showed clearly that as the nickel thickness increases, so does the size of the granules. The sputtered films consistently have larger granules than the evaporated films of the same thickness. This is attributed to the larger grain sizes of the as-deposited sputtered films. In normal grain growth the average grain size increases because larger grains tend to grow while smaller grains tend to shrink and disappear [65]. Thin films seldom experience completely normal grain growth due to interactions with the larger substrate at grain boundaries and

the almost always prevalent conditions that favor certain grain orientations. For example, Nickel nanocrystals show a preference for the $\langle 111 \rangle$ direction to be out of plane which indicates grains of this orientation grow faster than other orientations [67]. The results, represented in Figure 37, show the sputtered nanoparticles remain slightly larger than the initially smaller evaporated nanoparticles, indicating that the general trend of normal grain growth applies.

Table 3. Pretreatment Study Results

Treatment Time (Min)	PVD Method	Catalyst Thickness (Å)	Granule diameter (nm)
3.5	Evaporated	50	30
		100	45
		200	75
	Sputtered	50	35
		100	50
		200	80
5	Evaporated	50	20
		100	45
		200	100
	Sputtered	50	25
		100	58
		200	180
7	Evaporated	50	No Catalyst
		100	No Catalyst
		200	40
	Sputtered	50	40
		100	50
		200	60

The hydrogen plasma is expected to be a vapor etchant, which is considered beneficial during CNT growth where the H_2 removes amorphous carbon [35]. When hydrogen plasma is used to granulate the catalyst layer during pretreatment, etching also occurs. If the pretreatment process is too long and the catalyst layer too thin, it can be

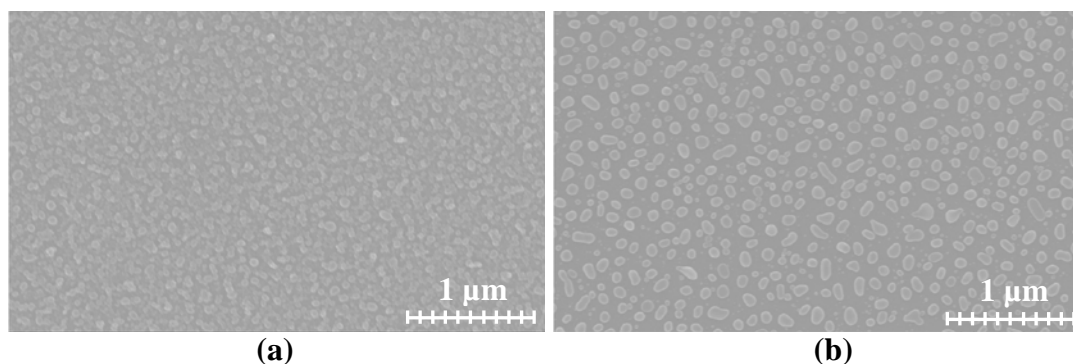


Figure 37. 100 Å Ni Layer after 5 minute pretreatment. SEM image shows good nanoparticle formation, (a) evaporated Ni and (b) sputtered Ni.

completely etched away, as was the case with the 50 and 100 Å evaporated Ni layers after 7 minutes of pretreatment. The 50 and 100 Å sputtered Ni layers were not removed during the 7 minute pretreatment.

Oddly enough, if the Ni catalyst is pretreated for too long the nickel nanoislands will begin to conglomerate creating islands with larger areas not suitable for CNT growth. The average diameter of nanoparticles of the 50 Å sputtered Ni increased from 25 nm to 40 nm from the 5 minute pretreatment to the 7 minute pretreatment. This phenomenon has been documented and attributed to Ostwald ripening [34]. Thus, determining the optimum pretreatment time is a crucial step in the CNT growth process.

Apart from the size of the catalyst, the areal density of the Ni catalyst is another important consideration. A high areal density will result in a dense CNT carpet which will aid in the growth of vertically aligned CNTs. Table 3 shows that in all cases the evaporated samples have smaller diameter particles and Figure 37 clearly illustrates that the evaporated samples have a higher areal density compared to the sputtered samples. The 5 minute pretreatment resulted in granulation closest to the nominal goal of 50 nm nanoparticles. The 50 Å evaporated and sputtered Ni catalyst was granulated into

nanoparticles averaging 20 nm and 25 nm, respectively; and the 100 Å evaporated and sputtered Ni was 45 nm and 58 nm. The 200 Å Ni samples both had average particle sizes of more than 100 nm, but due to the dispersive nature of the process there were many nanoparticles less than 100 nm as well.

AFM measurements were used to determine the surface morphology of the catalyst nanoparticles, specifically the boundaries or separation between granules. A representative AFM measurement comparing the 100 Å sputtered and evaporated samples is shown in Figure 38. The evaporated sample has smaller diameter granules with a higher areal density than the sputtered sample. For CNT growth, the pretreatment process must transform the Ni catalyst layer into Ni nano-islands and Figure 38 (a) shows that the evaporated samples have little to no spacing between their granules. CNT growth requires the hydrocarbon gas to completely surround the Ni catalyst for nucleation. The evaporated samples have many nanoparticles not completely separated, which may impede CNT growth.

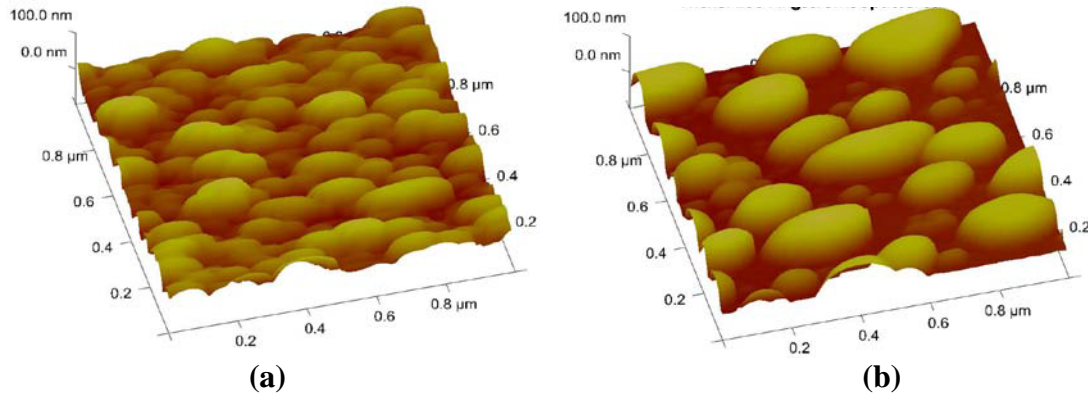


Figure 38. AFM measurement of 5 minute pretreatment (a) 100 Å evaporated Ni and (b) 100 Å sputtered Ni.

3.5. CNT growth

After the granulation of the catalyst has been accomplished the MPE-CVD system is adjusted to promote the growth of CNTs. CNT growth is achieved by increasing the substrate temperature to 650° C, increasing microwave power to 1000 W, and maintaining the pressure at 20 Torr while introducing the carbon feedstock gas, methane (CH₄), at a flow rate of 15 sccm and reducing the H₂ flow rate to 120 sccm for a ratio of 1:8, methane to hydrogen. The samples used above to analyze the pretreatment process were not used for CNT growth. Instead, samples with the same parameters were pretreated with the H₂ plasma for the specified time and then subjected to the 2 minute growth process without being removed from the MPE-CVD chamber.

A CNT growth time of 2 minutes was used with a goal of 1.5 – 2 µm CNTs. The 10, 350, and 500 Å Ni samples were completely unsuccessful showing no CNT growth. This was expected, due to the lack of any Ni after pretreatment on the 10 Å samples and the lack of granulation on the 350 and 500 Å Ni samples. The 50, 100, and 200 Å Ni samples all had some CNT growth. From Figure 39 (a), (c), and (e) it is very clear CNT growth was minimal on the evaporated samples, while the sputtered samples had significant CNT growth.

As noted above, the AFM measurements indicated evaporated films tend to result in granules that are closely packed together and may not be completely separated which would impede the growth of CNTs. The sputtered films in comparison showed complete granulation or separated nanoparticles in the AFM measurements, see Figure 38 (b), which resulted in successful CNT growth.

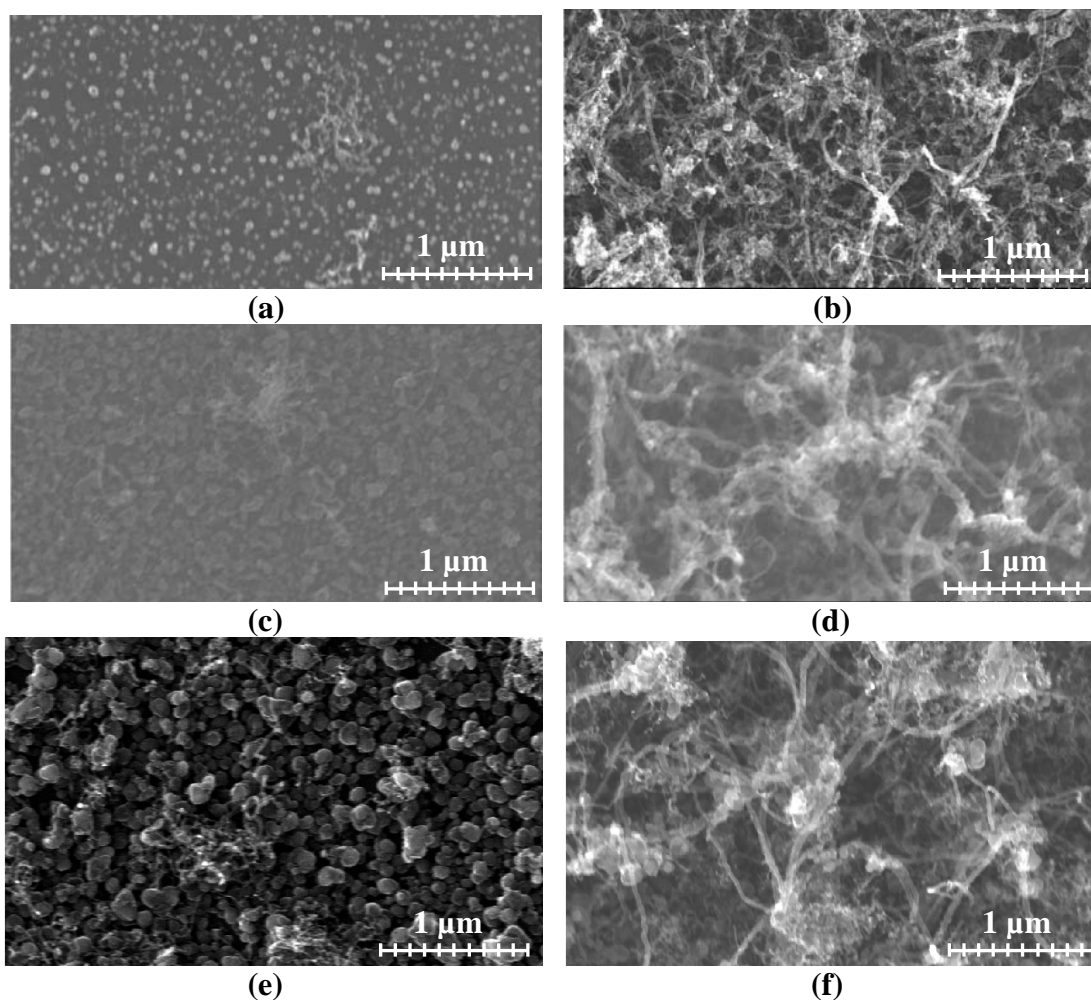


Figure 39. SEM image after 5 minute pretreatment and 2 minute CNT growth for (a) 50 Å evaporated Ni, (b) 50 Å sputtered Ni, (c) 100 Å evaporated Ni, (d) 100 Å sputtered Ni, (e) 200 Å evaporated Ni, and (f) 200 Å sputtered Ni.

Comparing Figure 39 (b), (d), and (f) the 50 Å sputtered Ni samples which had smaller average nanoparticle diameters with greater areal density resulted in denser growth with smaller diameter CNTs than the 100 Å and 200 Å sputtered Ni samples. There was no appreciable difference in the diameter of the CNTs between the 100 Å and 200 Å sputtered samples, but the 100 Å sample had denser CNT growth. The similarity in diameter with less dense growth would indicate the CNTs are only growing from the

smaller diameter nanoparticles spaced between the relatively large diameter nanoparticles that covered the majority of the 200 Å sample area.

The CNT growth rate for this process was estimated at approximately 1 μm per minute based on SEM micrographs taken at the edge of the samples. The growth time is measured as the time both the carbon feedstock gas is supplied in the presence of the microwave plasma. MWCNTs approximately 2 μm in length were achieved with a growth time of two minutes. A CNT carpet of approximately 13 μm was achieved with a growth time of 15 minutes. It should be noted that the lower portion of the CNTs tend to have some vertical alignment, however, the free ends do not.

3.6. Pretreatment Study Conclusions

An experimental parametric study of hydrogen plasma pretreatment of Ni catalyst layers deposited on a Ti diffusion barrier determined an optimum pretreatment time, catalyst deposition method, and thickness for CNT growth via MPE-CVD. As expected, thicker catalyst layers resulted in larger nanoparticles after pretreatment. Most significantly, it was shown that sputtered catalyst films facilitate CNT growth much better than evaporated films despite SEM imaging indicating “better” granulation with the evaporated films. The lack of CNT synthesis with evaporated catalyst layers was attributed to incomplete separation of the Ni nanoparticles shown through AFM measurements and the larger grain size and more defined grain boundaries of the initial sputtered Ni. While the thicknesses of the evaporated and sputtered layers were identical, there are clearly significant differences in the films. The sputtered Ni was deposited at a pressure of 3.2 mTorr which is within the intrinsic stress transition range of 1-10 mTorr.

The sputtered film may have compressive stress, while the evaporated film is most likely under tension due to differences in the coefficient of thermal expansion between the Si substrate and the Ti and Ni metal layers. Grain size is also inversely proportional to the yield stress, another reason large grains tend to grow and small grains tend to shrink. Evaporated catalysts are often used successfully in other CNT synthesis processes. Thus, these results have demonstrated a significant difference in the properties of sputtered and evaporated films in the same process conditions; not that evaporated Ni films cannot be used as a catalyst for CNT synthesis. Thus, sputtered and evaporated catalysts should not be considered interchangeable in a CNT fabrication process.

Variations of the pretreatment time, catalyst layer deposition and thickness were used to achieve desired catalyst nanoparticle diameters while maintaining a relatively high areal density for the growth of CNTs. The results of this study, as demonstrated with AFM measurements and SEM images, show a 50 Å sputtered Ni catalyst layer granulated for 5 minutes in a hydrogen plasma was the most effective recipe for growing dense CNTs via MPE-CVD.

3.7. CNT Characterization and Process Improvements

One of the advantages of MPE-CVD is the ability to control almost every aspect of the synthesis process, temperature, pressure, gas composition and flow, microwave power, and even the physical location of the microwave plasma. This control makes it possible to fine tune the growth process and improve the quality of the CNTs. The quality of the CNTs is assessed through SEM micrographs and Raman spectroscopy.

Having worked out an effective pretreatment process that granulates the catalyst into the desired nanoparticles allows the growth process to be adjusted to eliminate defects.

3.7.1. Raman Spectroscopy

Raman spectroscopy is a light scattering technique where an excitation laser is focused on the material of interest and the interaction of the photons with the material results in a small amount of light scattering at a slightly different frequency. This slight shift in frequency is called a Raman shift and provides a unique finger print of the material. Raman spectroscopy has been used for decades to identify carbon materials; and more recently has been shown capable of providing a myriad of information about well-ordered carbon materials such as doping, defects, diameter, chirality, and curvature [69]. Figure 40 shows the Raman shift of a number of carbon materials,

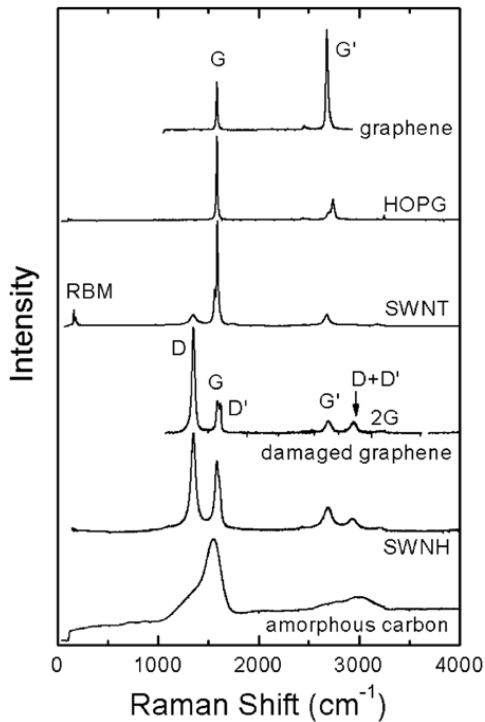


Figure 40. Raman shift of various carbon materials [69].

graphene, highly ordered pyrolytic graphite (HOPG), single walled nanotubes (SWNT), damaged graphene, single walled nano-horns (SWNH), and amorphous carbon. With the exception of amorphous carbon and HOPG these materials are all single atomic layers of carbon, which makes for specific and unique Raman shifts. Raman spectroscopy does not work as well for MWCNTs because the multiple nested CNT walls result in some dispersive effects whether defects are present or not. However, it is still very useful for identifying MWCNTs and determining the general quality based upon the Raman shift peaks present and the corresponding peaks relative intensities.

Raman spectroscopy was performed using a 532 nm green excitation laser, which provides Raman shift wavelengths from 200 – 3400 cm^{-1} . CNTs have a Raman shift with three primary peaks of interest within this range, D-band, G-band, and G'-band, that can be used to determine CNT quality [70]. The G-band peak is located at approximately 1580 cm^{-1} and is a result of ordered C-C bonds, indicative of defect free graphene and carbon nanotubes. The D-band, approximately 1350 cm^{-1} , is a disorder induced peak caused by defects in the carbon structure. A relative determination of CNT quality can be found by comparing the ratio of the D-band intensity over the G-band intensity (D/G).

The G'-band, approximately 2700 cm^{-1} , is dispersive but it is the result of a double resonance process and is also very prevalent in Raman shift data for graphene, see Figure 40. DiLeo *et al* propose that in MWCNTs disorder or defects will reduce this double resonance process decreasing the G' peak intensity; similar to the graphene and damaged graphene Raman shifts in Figure 40, when the graphene structure is damaged the G' peak almost entirely disappears [70]. Thus, in order to have the G' dispersive effect the carbon

structure has to be well ordered and free of the dispersive defects that cause the D peak. The ratio of the G' peak intensity over the D peak intensity (G'/D) has been shown to be a more accurate indication of CNT quality than the more commonly used ratio of D/G [70]. The ratio, G'/G , was also recorded for completeness.

The use of the G' peak as an indicator of MWCNT quality may have one caveat attached. The G' peak particularly and to some extent the G peak have greater intensity when the excitation laser is reflecting off the CNT sidewalls which can be defect free. The tips of MWCNTs are defective by nature due to the metal catalyst particle that caps the end. Pristine, vertically aligned CNTs may not be represented well by Raman shift due the high defect density at the exposed tips. Figure 41 shows an SEM image and Raman shift of vertically aligned MWCNTs purchased from Nano Lab, Inc. The CNTs appear pristine in the SEM micrograph, yet the Raman shift shows a D/G ratio of 0.89 which is worse than many of the CNT samples grown via T-CVD evaluated in Chapter IV. The G' peak is uncharacteristically low for a D/G ratio less than one. It is possible that the DC-CVD process used at Nano Lab, Inc. to grow the CNTs results in vertically aligned, defective CNTs. However, it's more likely that the defects are

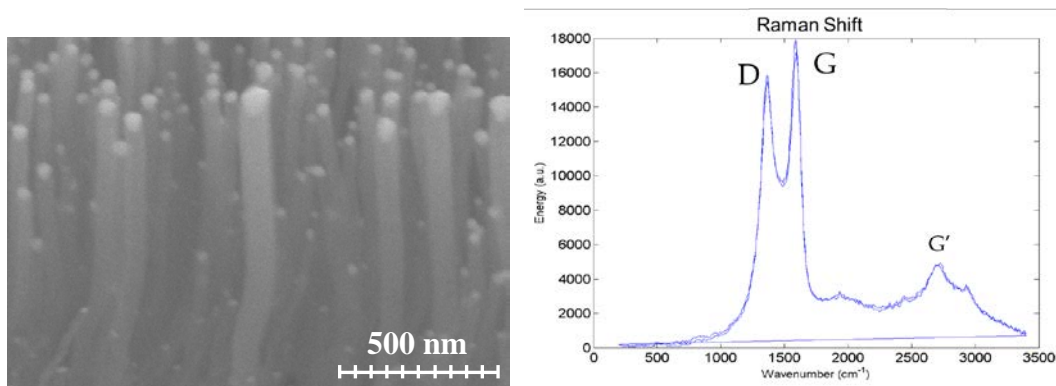


Figure 41. Commercial vertically aligned MWCNTs and Raman shift.

primarily at the CNT-metal barrier at the tips of the CNTs; and the Raman shift is not representative of the CNTs as a whole.

Often in the literature Raman spectroscopy is used solely to identify the presence of ordered carbon, especially for MWCNTs, by simply including a truncated Raman shift showing D and G peaks of any ratio as shown in Figure 42. Seldom is the G' peak discussed; most likely due to its absence because of the typically large D peak present in the Raman shift of MWCNTs. Raman spectroscopy by itself does not provide a complete picture of carbon nanotube quality. SEM images are also necessary to determine the areal density, presence of amorphous carbon, and physical characteristics of the CNTs such as alignment, length, and diameter. It should also be noted that from the SEM micrograph in Figure 42, there appears to be no vertical alignment of the CNTs. However, a profile SEM micrograph shows the CNTs are vertically aligned for the first 80-90% of their lengths [71].

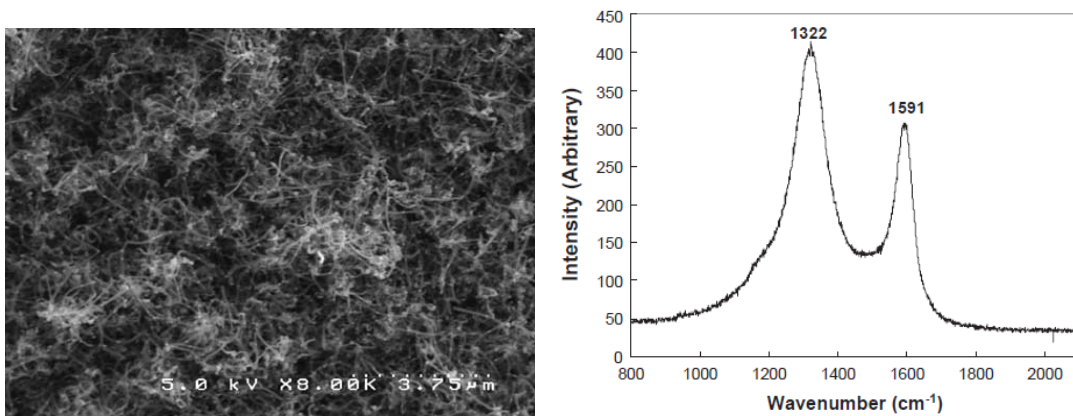


Figure 42. T-CVD grown MWCNTs with truncated Raman shift [71].

The initial CNT growth recipe developed in Section 3.5 produced CNTs, but the results were not reliable due to microwave tuning difficulties and the lack of an optimized

recipe. CNT carpets grown using this recipe and system ranged from those shown in Figure 39 above to the extremely poor quality CNTs shown below in Figure 43 (a) below.

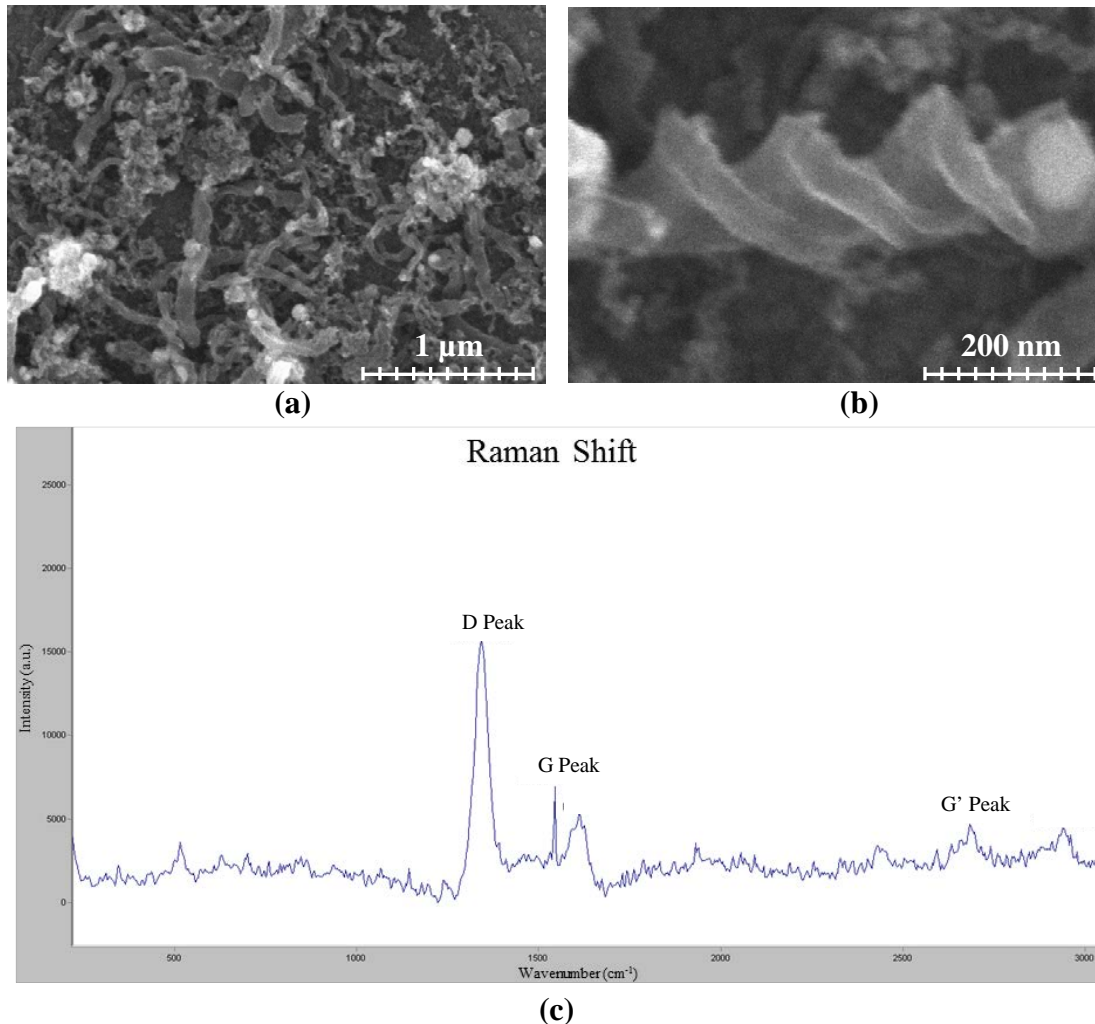


Figure 43. (a) Poor quality CNT growth; (b) defective CNT; (c) Raman shift.

These CNTs have diameters in excess of 100 nm and are extremely defective as shown in Figure 43 (b). Samples of this poor quality do not qualify as carbon nanotubes, but should be referred to as carbon nano-fibers. This characterization is further supported by the Raman shift shown in Figure 43 (c). There is a very high disordered D peak with almost no ordered G peak resulting in an I_D/I_G ratio of 2.33. As mentioned above, without any substantial order the second order G' dispersive peak has very little intensity.

The Raman shift as a whole is very similar to the damaged graphene Raman shift shown in Figure 40 rather than any of the ordered forms of carbon measured. Defective CNTs of this magnitude are unacceptable for any application.

3.7.2. Improved MPE-CVD Synthesis Process

After upgrading the microwave power generation system which made precise tuning and plasma generation possible; the CNT growth recipe was adjusted to improve CNT growth. Adjustments were made primarily to the pressure and methane to hydrogen ratio. Relatively small changes in pressure can have significant effects on the microwave plasma in the chamber where increases in pressure push the plasma ball towards the sample stage. In this case a reduction in pressure raised the plasma ball slightly above the stage. The second adjustment was to the gas mix ratio. The gas flow of both gasses was increased slightly, H₂ was increased from 120 to 125 sccm, which allowed the same gas flow for both the pretreatment and growth phases simplifying the process slightly. The CH₄ was increased from 15 to 20 sccm increasing the gas ratio from 1:8 to about 1:6 providing more carbon for the CNT synthesis. Increasing the CH₄ ratio above 1:6 resulted in carbon saturation and caused the formation of significant amounts of amorphous carbon. The precise control over the microwave plasma and the slight adjustments to pressure and process gas flow rates led to a final MPE-CVD process recipe with repeatable quality CNT growth. This improved growth recipe is listed below.

3.7.2.1. MPE-CVD Recipe

The improved MWCNT growth process employed for the MPE-CVD system begins with removing as many potential contaminants as possible by evacuating the

chamber below 10 mTorr after the sample is loaded. Then the graphite stage and sample are heated to 400° C with H₂ flowing at 125 sccm and chamber pressure maintained at 15 Torr. Once the system has reached a steady state, the granulation pretreatment of H₂ plasma induced by 400 W of microwave power is conducted for 5 min. The microwave power is terminated at the end of the 5 min pretreatment and the temperature is increased to 650° C while maintaining the same gas flow and pressure. The growth phase occurs for 1-2 min at 650° C, 5 Torr, H₂ at 125 sccm, methane (CH₄) at 20 sccm, and 1000 W of microwave power. A 2 min growth results in MWCNTs of 2 – 5 µm in length. Both the methane and microwave power are shut off to end the growth phase. The hydrogen flow and chamber pressure are maintained to facilitate cooling.

3.7.3. MWCNT Quality Analysis

Figure 44 shows an SEM micrograph and Raman shift of two representative samples grown via this improved recipe with all barrier and catalyst layers deposited via sputtering. The CNTs have a high areal density and are uniform in diameter with most CNTs being close to the desired 50 nm. The bright spots at the CNT ends are caused by catalyst particles that facilitated tip growth and now form a cap or plug at the CNT tip. The samples were clean having no observed amorphous carbon and the Raman shift varies only slightly from sample to sample. Unfortunately, the samples have high defect densities with the D peak being dominant which virtually eliminates the G' peak. The Raman shift peak ratios for samples (a) and (b), shown in Figure 44, are:

- D/G (a) 1.26 (b) 1.58
- G'/D (a) 0.19 (b) 0.14
- G'/G (a) 0.15 (b) 0.09

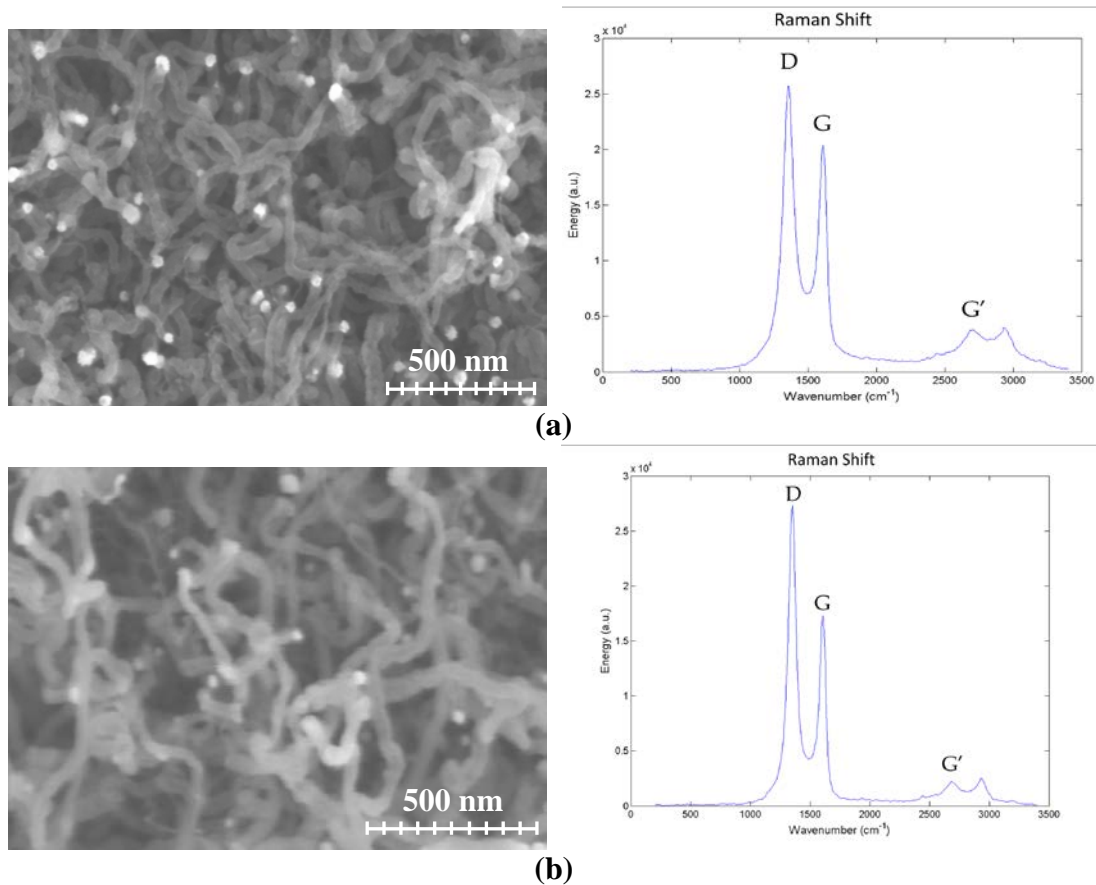


Figure 44. MPE-CVD grown CNTs and the corresponding Raman shift.

Based on the Raman shift, sample (a) is a better quality CNT growth with a slightly lower D/G and higher G'/D ratios. In cases such as these where the D peak is dominant, the best indicator of quality from the Raman shift will be the D/G ratio. As the D/G ratio drops below one and the G' peak increases; the larger G'/D ratio will become a more important indicator of MWCNT quality. Presently, it is not clear if there is a desired value for the G'/G ratio. While the CNTs of both samples do not appear to be vertically aligned the visible presence of the CNT tips in the SEM image, especially in sample (a), is indicative of some alignment. The repeatable, clean, dense, CNT growth with Raman shift indicating a quality of growth similar to other reported efforts for MWCNTs grown via CVD methods, see Figure 42, validates the improved MPE-CVD growth recipe used.

There is still significant room for process improvement--the defect density should be reduced and the end goal is still vertically aligned MWCNTs.

3.8. Summary

This chapter documented the steps to successful CNT synthesis via MPE-CVD. A detailed study of the catalyst and barrier layer materials was conducted to develop a pretreatment step capable of granulating the catalyst to the desired particle size. The growth phase was fine tuned to improve repeatability and quality of the MWCNTs. The resulting CNTs were characterized using SEM micrographs and Raman spectroscopy. The results of diode configured field emission tests with the CNT carpet samples characterized in this chapter are reported on in Section 4.4 with the results of T-CVD carpet samples for ease of performance comparisons.

IV. Thermal CVD CNT Synthesis Development and Characterization

Thermal CVD is the simplest of the various CVD synthesis methods available. It is simply flowing the correct gas mix through a large resistive heater. If the temperature, pressure, gas mix and flow rate, are correct CNTs will form. T-CVD synthesis, just like MPE-CVD synthesis described in the previous chapter, begins with substrate preparation. This chapter describes a parametric study of different catalyst and barrier materials' thicknesses were varied and the resulting CNT carpets were characterized and tested for field emission.

The physical characterization is carried out with SEM observations and Raman spectroscopy as described in Chapter III. Next the field emission properties of the CNTs, including the MPE-CVD grown samples, are characterized to include turn-on electric field strength, maximum current density at a fixed electric field strength, current density versus electric field strength relationship, and a Fowler-Nordheim plot is used to calculate field enhancement. Field emission tests are performed in a diode configuration under high vacuum. The CNTs are grounded and act as the cathode. The anode is a copper collector plate located above the CNTs. The anode is swept across a positive voltage range. The field emission current is measured through the anode and the current density is calculated using the area of the sample under test. The current density vs. electric field relationship is collected as the anode voltage is swept across the voltage range and displayed in a corresponding graph. The Fowler-Nordheim plot as derived in Section 2.7.1 from the Fowler-Nordheim model provides evidence the recorded current

density was the result of field emission as opposed to thermionic emission and was used to calculate the field enhancement factor.

All the CNT characterization and field emission data is collected and relationships between the quality of the CNT carpet growth and the resulting field emission properties are defined. Due to the results of another research effort that indicated a carbon buffer layer may facilitate CNT growth, the effects of an additional carbon buffer layer between the barrier and the catalyst on CNT quality and field emission was also investigated. Finally, the barrier/catalyst combination that makes the best field emission source was determined.

4.1. Substrate Preparation

Previous research with T-CVD had focused on non-conductive barrier layers on a Si substrate. A conductive barrier is required for field emission applications. Previous research has indicated that the barrier layer material can significantly affect the granulation process [72]. Thus, it was necessary to develop a process beginning with a conductive barrier layer. To that end, each silicon substrate was first coated with a barrier layer of titanium or chrome. This thin film acts as an adhesion layer and as a diffusion barrier preventing the formation of metal silicides. It also facilitates the cathode connection to the CNTs during field emission. Only a thin barrier layer, ~25 nm, is required for the purposes of adhesion and diffusion barrier, but a thicker layer, ~100 nm, was considered to improve conductance during field emission. Sputtered Ni and Fe were used as the catalyst layers, but unlike the MPE-CVD process the Ni catalyst did not result in CNT growth. Iron catalyst was deposited on both barrier materials in thicknesses of

10 nm and 2 nm. All of the barrier and catalyst layers were deposited via DC magnetron sputtering.

4.2. T-CVD CNT Synthesis Recipe

The quartz chamber and samples are prepared for growth by evacuating the chamber down to less than 10 mTorr for 15 minutes; after which an Ar+H₂ mix (95% + 5%) is flowed through the chamber to remove unwanted contaminants. The chamber is then evacuated again for an additional 15 minutes. Now that the samples and chamber are prepared, the Ar+H₂ gas mix is flowed while the chamber pressure is stabilized at approximately 90 Torr for the remainder of the entire process. The sample is annealed at 750° C to form iron nano-islands necessary for CNT synthesis. Next, the growth phase begins with the introduction of the carbon feedstock, in this case an Ar+C₂H₂ (90% + 10%) mix, into the chamber. Growth times ranged from 2 - 20 minutes, resulting in MWCNTs measuring from 5 – 30 μm in length. The growth phase is followed by a short clean phase with Ar+H₂ flow while the chamber temperature is maintained at 750° C. This removes any weakly bonded residual surface carbon contamination from the sample. Finally, the chamber is cooled to room temperature over a 45-60 minute period with a constant flow of the Ar+H₂ mixture.

4.3. CNT Characterization

Figure 45 shows SEM micrographs and the Raman shifts of the highest quality (a) and lowest quality (b) T-CVD grown CNTs based on the Raman shift data. The highest quality MWCNTs of all the different catalyst/barrier combinations considered was from 10 nm of Fe catalyst on a 100 nm Ti barrier with D/G and G'/D ratios of 0.47 and 2.52

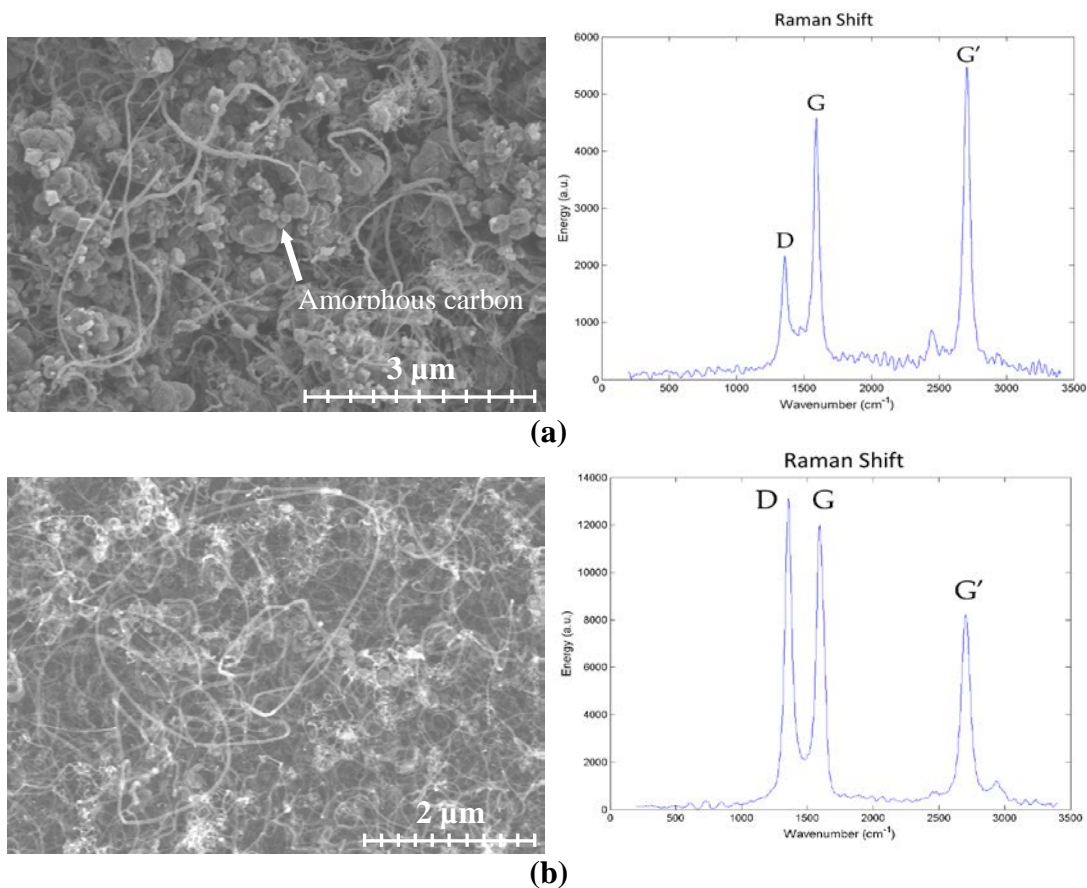


Figure 45. SEM micrograph and Raman shift of (a) highest quality and (b) lowest quality MWCNTs grown via T-CVD.

respectively. The lowest quality MWCNTs, with a D/G ratio of 1.09 and G'/D ratio of 0.63, are from the catalyst/barrier combination of 2 nm of Fe on 20 nm of carbon which is on a 25 nm Ti barrier. This sample reinforces the claim that the first order D peak dispersive effects prevent the secondary double resonance G' peak dispersive effects. The Ti25/C20/Fe2 sample is still much better quality, as far as CNT defects, than any of the MWCNTs measured from the MPE-CVD process. However, as mentioned above, Raman spectroscopy provides a relative measure of the quality of the CNTs, but SEM imagery is required to complete the characterization of the CNT carpets.

SEM micrographs of the highest and lowest quality CNT samples per Raman spectroscopy lead to different conclusions about the quality of the CNT carpet. The SEM image of the highest quality CNTs in Figure 45 (a) are sparse with large amounts of amorphous carbon deposited across the substrate surface. Also, the diameter of the CNTs varies widely from ~20 – 100 nm. While the individual CNTs present may have few defects, the overall quality of the CNT carpet is poor due to the low areal density, amorphous carbon deposits, and diverse diameters. SEM image of Figure 45 (b) shows a much higher density of CNTs with less dispersive diameters. These CNTs may have more growth defects, but the CNT carpet is much better than the sparse growth visible in Figure 45 (a).

Table 4 lists the Raman shift intensity ratios and SEM based qualitative assessment of CNT growth for all catalyst/barrier combinations. The chrome barrier of both 25 and 100 nm thicknesses performed poorly. Two combinations, Cr100/Fe2 and Cr100/C20/Fe2, did not grow CNTs at all. In Figure 46, the SEM micrograph of the catalyst after the anneal and growth process revealed poor granulation with the expected nano-islands spanning hundreds of nanometers instead of the desired 25 - 50 nm. It is also likely that the large nanoparticles are primarily Cr with little or no Fe present. The Cr100/Fe13 sample grew a sparse CNT carpet with CNT diameters in excess of 100 nm putting them closer to carbon fibers rather than carbon nanotubes. The addition of 20 nm of carbon improved the anneal process for the Cr barrier samples. The Cr100/C20/Fe10 sample showed an improvement over the Cr100/Fe13 sample in both D/G and G'/D

ratios and the CNT diameters were reduced to less than 100 nm. But the Cr100/C20/Fe2 did not grow CNTs the same as its counterpart the Cr100/Fe2 sample.

Table 4. Raman shift peak intensity ratios and SEM based qualitative assessment of CNT growth for all catalyst/barrier combinations.

Barrier Layer Type & Thickness (nm)		Catalyst (nm)	D/G	G'/G	G'/D	Areal Density	Overall Growth
Chrome	100	13	0.69	0.82	1.20	Low	Poor
	100	2	No CNT Growth				
	25	10	0.48	1.11	2.31	Low	Poor
	25	2	0.88	0.72	0.82	Medium	Poor
Chrome & Carbon	100 & 20	10	0.60	1.09	1.82	Medium	Good
	100 & 20	2	No CNT Growth				
	25 & 20	10	0.54	1.19	2.19	Low	Poor
	25 & 20	2	0.81	0.89	1.10	Medium	Poor
Titanium	100	10	0.47	1.19	2.53	Low	Poor
	100	2	0.56	0.95	1.71	Low	Poor
	25	10	0.48	0.99	2.06	Medium	Good
	25	2	0.90	0.86	0.96	Medium	Good
Titanium & Carbon	25 & 20	10	0.48	1.09	2.26	Low	Poor
	25 & 20	2	1.09	0.69	0.63	Medium	Poor
MPE-CVD #1	Ti 20	Ni 10	1.26	0.20	0.16	High	Good
MPE-CVD #2	Ti 20	Ni 10	1.58	0.15	0.09	High	Good

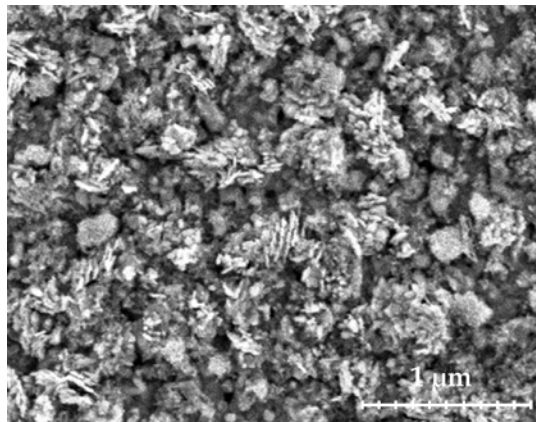


Figure 46. SEM of Cr100/Fe2 after T-CVD process.

The 25 nm chrome samples had poor overall CNT carpets. The Cr25/Fe10 sample was almost identical to the Ti100/Fe10 sample shown in Figure 45 (a), sparse growth of

low defect CNTs with large deposits of amorphous carbon. The addition of 20 nm of carbon to the Cr barrier layers improved the Raman shift ratios slightly in the Cr25/C20/Fe2 case, but made the D/G and G'/D ratios slightly worse for the Cr25/C20/Fe10 case. In both cases there was no appreciable difference in the SEM micrographs between the carbon and no carbon buffer layer combinations.

All titanium barrier combinations produced CNT carpets; although the 100 nm titanium samples had anneal issues that resulted in low defect CNTs with poor overall CNT carpet growth as discussed above and shown in Figure 45 (a). The 25 nm titanium barrier proved most effective for growing MWCNT carpets. The Ti25/Fe10 sample, shown in Figure 47, produced a medium to high density, low defect CNT carpet with little to no amorphous carbon and fairly uniform diameters. The Ti25/Fe2 carpet had a lower areal density with more CNT defects as evidenced by the Raman shift ratios. Adding the carbon thin film to the Ti barriers had little effect on the Raman shift characteristics, but made the overall CNT carpets less dense with more amorphous carbon deposits; for the Ti25/C20/Fe10 case the amount of amorphous carbon was significantly increased.

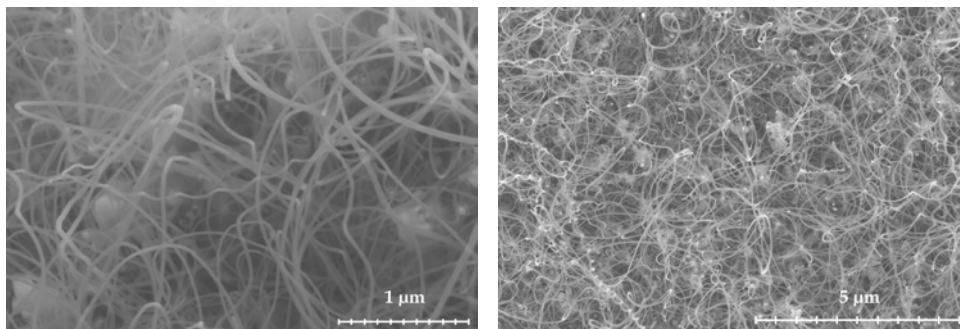


Figure 47. SEM micrographs of CNT carpet grown by T-CVD on Ti25/Fe10 sample.

Using thermal CVD, the 25 nm Ti is clearly the most effective barrier with the Ti25/Fe10 nm sample producing the cleanest, defect free CNT carpets out of all the barrier/catalyst combinations. The 100 nm Ti and both Cr barrier thicknesses have different thermal properties that will require extensive study to determine an appropriate anneal process for each barrier/catalyst combination to achieve catalyst nano-islands conducive to CNT synthesis. The addition of sputtered carbon as a buffer between the barrier and the catalyst did not reduce the effects of changes to the barrier, but rather added another change to the thermal properties during the anneal process. The addition of carbon on the chrome barrier improved the anneal process and subsequent CNT growth. However, the carbon layer degraded the overall quality of the CNT carpet growth when added to the Ti barrier, most likely due to the increased amorphous carbon.

The MPE-CVD grown CNT carpets are defect prone, but have no discernable amorphous carbon and have the highest areal density. MPE-CVD also offers precise control of the CNT growth conditions in the MPE-CVD process making it possible to achieve CNT carpets with uniform lengths. The CNT carpets of the two samples considered are approximately 2 μm in length. The short length is necessary for future integration into gated field emission devices. The T-CVD process does not have as much control over the growth conditions of the CNTs. Figure 48 shows a Ti25/Fe10 sample with a CNT carpet from a 2 minute growth. The CNTs are less dense than the 20 minute growth shown in Figure 47, but still are in excess of 10 μm in length with many exceeding 15 μm . Integration of CNTs grown by T-CVD into gated field emission

devices is unlikely until the lack of uniformity and control of the CNT lengths is resolved.

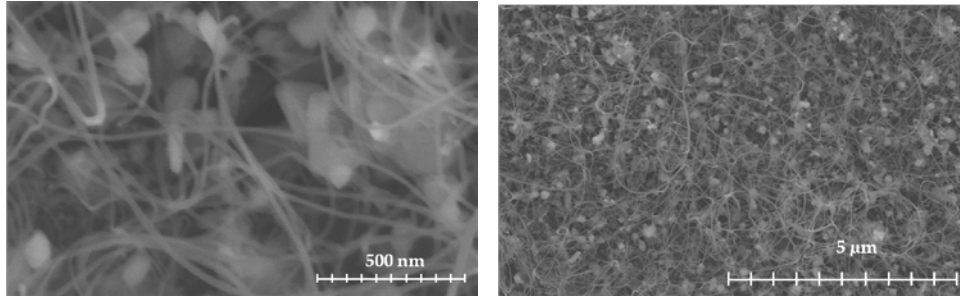


Figure 48 . SEM micrographs of CNTs grown by T-CVD for 2 minutes on Ti25/Fe10 sample.

4.4. Field Emission Results

After CNT characterization with Raman spectroscopy and SEM imagery, the CNT carpets were tested for field emission. This section describes the test chamber and the testing procedures used to obtain field emission properties of each sample. This performance data is collated and compared with the physical characterization to determine the most effective catalyst/barrier combination.

4.4.1. Test Chamber

The CNT field emission test chamber, shown in Figure 49, provides a high vacuum controlled environment down to 2×10^{-7} Torr. The load lock system allows samples to be changed quickly while maintaining high vacuum in the main chamber. Two associated DC power supplies provide voltages from 0-5000 V and 0-1250 V. The test stage and chamber feed-throughs have 7 wired ports. All testing procedures have been automated using the GPIB interface and Labview software for precise testing.

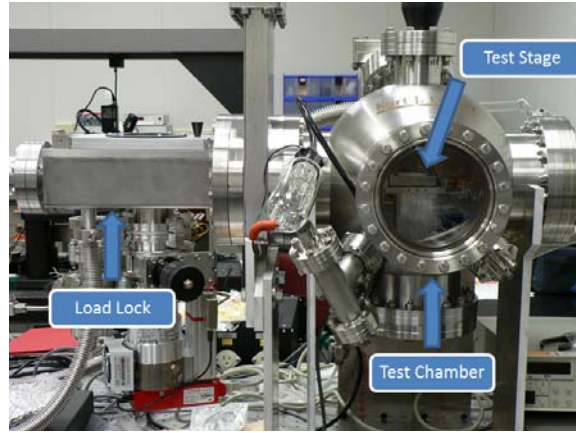


Figure 49. Field Emission Test Chamber.

4.4.2. Test Procedure

The device under test is mounted to a test structure with spring compression using copper wires. These also provide the electrical contact for the CNT carpet. The friction contact resistance measured is less than $1\ \Omega$. The test structure is then loaded into the main test chamber via the load lock. Field emission can only occur in a vacuum so the chamber is evacuated to less than 5×10^{-6} Torr.

The total current is measured on both the supply and ground side of the device under test, see Figure 50, to detect any potential leakage currents. A complete test run consists of increasing the extraction voltage in 10 V increments, equates to $\sim 0.05\ \text{V}/\mu\text{m}$,

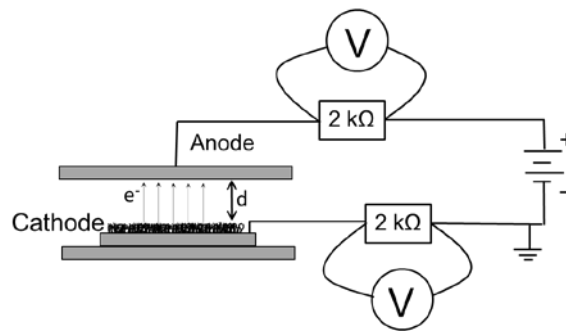


Figure 50. Diode configuration testing schematic.

from zero up to a pre-set voltage. At each voltage, after a user defined pause (default is 4 sec) for the system to reach a steady state, 100 measurements are taken at 0.01 sec intervals and averaged before proceeding to the next voltage increment. After reaching the pre-set voltage, the process is reversed and measurements are taken as the voltage steps back down to zero. The initial pre-set voltage is 700 V or ~ 3 V/ μm . However, if at any point during the test damage occurs to the CNTs, determined by visual arching at the CNT carpet or by sudden current spikes, the test is immediately terminated and the highest voltage measured is recorded as the maximum for the device under test. If a device is tested to 700 V with little or no field emission measured, the set voltage is increased for further testing. The system maximum voltage is 5000 V or ~ 23 V/ μm . The highest electric field applied for this effort was 5.34 V/ μm . Increasing the electric field strength too far damages the CNTs and causes permanent degradation in field emission performance.

The collected field emission data displayed in Figure 51 visually identifies the

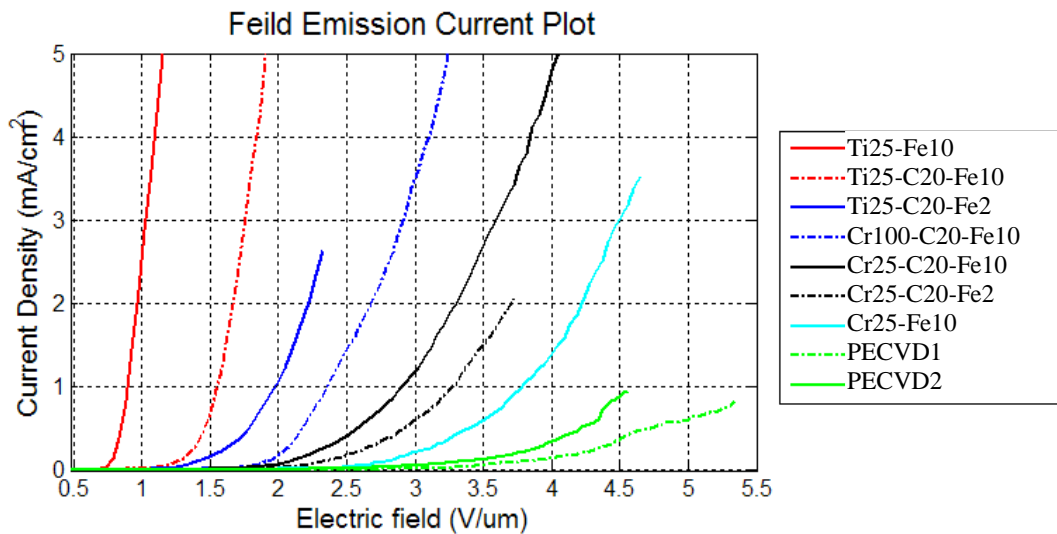


Figure 51. Field emission current density plot for selected samples.

strong field emission performers. The measurements are collected as current and matching voltage. The total field emission area is determined by measuring the sample area under the collector plate during the field emission tests using a set of precision callipers. The electric field is calculated simply by dividing the applied voltage by the distance, d , between the device under test and the collector plate ($d = 215 \mu\text{m}$). The field emission vs electric field plot should be an exponentially increasing curve if field emission is the current source. All of the samples shown in Figure 51 demonstrate this exponential trait.

The Ti25/Fe10 sample identified in Section 4.3 as the best overall CNT carpet sample clearly stands out as the best performer. The field emission test results are used to determine field emission properties or metrics for each sample. The turn-on electric field is the electric field strength required for a sample to reach a current density of $10 \mu\text{A}/\text{cm}^2$. As described above, the maximum current density achieved without damaging the CNT carpet and the corresponding electric field was also collected. The raw current vs voltage data was used to create Fowler-Nordheim Plots, $\ln(I/V^2)$ versus $1/V$, for each sample as derived in Section 2.7.1. A linear Fowler-Nordheim plot is indicative of field emission. The Fowler-Nordheim plots for selected samples are contained in Figure 52. Least squares linear regression was used to determine the slope, m , of the linear plots so the field enhancement factor, β , could be calculated using Equation (18).

$$\beta = \frac{bd\phi^{\frac{3}{2}}}{m} \quad (18)$$

Where $b = 6.83 \times 10^7 \text{ eV}^{-3/2} \text{ Vcm}^{-1}$, $d = 2.15 \times 10^{-4} \text{ cm}$, and $\phi = 4.65 \text{ eV}$. All the field emission metrics are listed for each processed barrier/catalyst combination in Table 5.

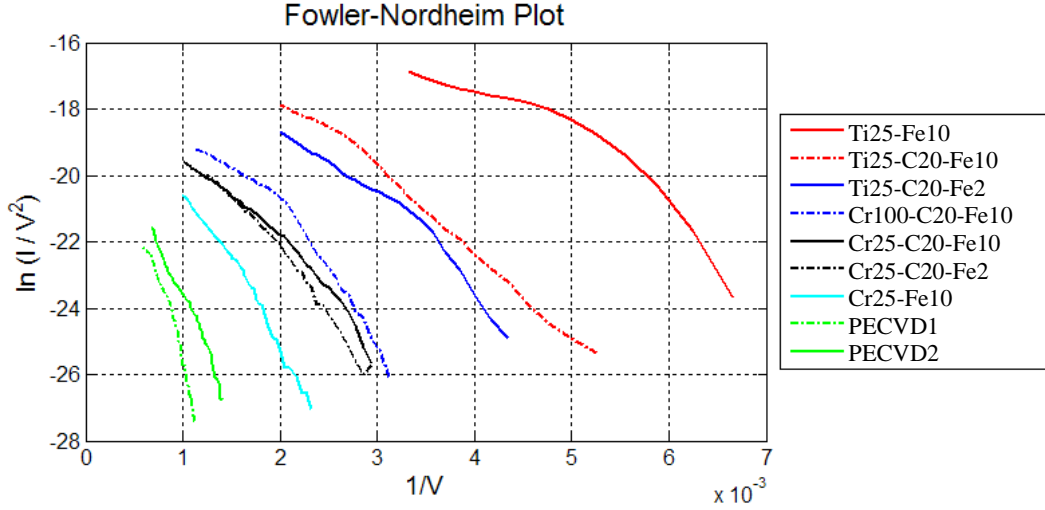


Figure 52. Fowler-Nordheim plot for selected samples.

Table 5. Field emission data for all combinations of barrier/catalyst samples.

Barrier Layer Type & Thickness (nm)		Catalyst (nm)	Beta	Turn-on E-field (V/ μm)	Max Current Density (mA/cm ²)	Max E-field (V/ μm)
Chrome	100	13	4660	2.56	0.13	3.72
	100	2	No CNT Growth			
	25	10	3110	2.37	3.52	4.65
	25	2	3630	2.60	0.34	4.19
Chrome & Carbon	100 & 20	10	4870	1.63	12.30	4.14
	100 & 20	2	No CNT Growth			
	25 & 20	10	5430	1.72	8.71	4.65
	25 & 20	2	4150	1.91	2.05	3.72
Titanium	100	10	6780	1.86	0.30	3.26
	100	2	3130	2.56	3.99	5.12
	25	10	8640	0.74	13.34	1.40
	25	2	8020	1.02	9.25	2.37
Titanium & Carbon	25 & 20	10	6070	1.63	12.94	2.33
	25 & 20	2	6130	1.21	2.63	2.33
MPE-CVD #1	Ti 20	Ni 10	2390	3.16	0.82	5.34
MPE-CVD #2	Ti 20	Ni 10	3460	2.56	0.95	4.56

As mentioned above, the Ti25/Fe10 sample immediately jumps out as the best field emission source with the highest β , lowest turn-on electric field, and the highest total current density with the lowest electric field. Excellent field emission from the CNT carpet with the best qualities is a reassuring result. However, the improvement in field emission from adding the carbon buffer to the chrome barrier is astounding. The Cr100/Fe13 sample had extremely large diameter CNTs to the point of being considered carbon fiber more than carbon nanotubes. The field emission from these samples was also poor with a total current density of only 0.13 mA/cm².

The Cr100/C20/Fe10 sample on the other hand demonstrated a 30% reduction in turn-on voltage and a 100x increase in maximum current density. The same is true for the 25 nm chrome barrier layers. While the addition of the carbon buffer did not have a significant effect on the characteristics of the CNT carpets showing moderate improvement in the Raman shift for the Cr25/C20/Fe2 sample and a moderate degradation for the other sample, the improvements to the field emission properties are striking. Both samples saw a 20% reduction in turn-on electric field strength, 2.5x and 6x increases in maximum current density, and corresponding increases in the field enhancement factor. The carbon buffer layer clearly has a positive interaction with the chrome barrier that enhances field emission.

Much like the results on the CNT characteristics, the carbon buffer on the 25 nm titanium barrier layer degraded the field emission properties to include lower field enhancement factors, higher turn-on electric fields, and lower maximum current densities. The maximum current density between the Ti25/Fe2 and Ti25/C20/Fe2

samples decreases from 9.25 mA/cm^2 to 2.63 mA/cm^2 at essentially the same electric field strength. As clearly as the carbon buffer improved the field emission properties of the chrome barrier samples, it degraded the field emission properties of the titanium barrier samples.

Field emission from the MPE-CVD samples does not compare well with the T-CVD samples. The MPE-CVD carbon nanotubes have a much higher areal density and are much shorter in length at $2 \mu\text{m}$. Both of these factors increase screening effects reducing field emission. However, as mentioned above, the controlled growth using MPE-CVD makes patterned and gated or triode configured field emission devices more feasible.

4.5. Summary

In this phase of a continuing research effort to develop CNT field emission devices, a study of the effects of Fe catalyst layers deposited on Ti and Cr diffusion barriers has been used to determine an optimum combination for effective field emission from CNTs produced via T-CVD and compared with a similar study for MPE-CVD. As expected, thicker catalyst layers resulted in larger nano-particles after the anneal or pretreatment granulation process causing more amorphous carbon deposits as shown in SEM images. Raman spectroscopy was used to characterize the quality of the CNTs. The G'/G ratio was calculated as another possible metric that could relate Raman shift characteristics to field emission. Since no relationship was evident and there is no evidence that the G'/G ratio is helpful in determining CNT quality, the G'/G ratio was determined to be an unnecessary calculation for future endeavors.

This study showed that sputtered Fe catalyst films on thin barrier layers (25 nm) of Ti facilitate excellent CNT growth by T-CVD with superior CNT field emission properties, specifically, lower turn-on electric fields and much higher field emission current densities than any other combination of barrier and catalyst via either growth method. There was not a clear correlation between CNT quality as determined by Raman spectroscopy and CNT field emission. This is attributed to the effects CNT areal density has on field emission. When the areal density is extremely high, such as with the CNT carpets grown by MPE-CVD, screening effects impede field emission. When the CNT growth is sparse, the lack of field emission sources or CNTs impedes field emission. The best field emission was achieved by the Ti-25/Fe-100 sample which had both good Raman shift characteristics and qualitatively good or medium areal density.

The addition of a carbon buffer layer between chrome diffusion barriers and the catalyst layer showed some potential for improving the quality of CNT growth and increased field emission dramatically. The lack of CNT synthesis with thicker barrier layers was attributed to poor or at least different thermal properties of the thicker metallic barrier which impeded the granulation process resulting in incomplete separation of the catalyst nanoparticles shown through SEM micrographs. The lack of good quality CNT carpet growth from any of the Cr barrier samples, which are often used successfully in CNT synthesis, is a result of the significant impact different barrier layers have on the granulation and growth processes. Any changes to the barrier or catalyst will require the development of a specific growth recipe.

While the most successful field emission results were achieved with samples produced by T-CVD, the MPE-CVD process allows better control and uniformity of the CNT lengths. The shorter length and high areal density of the MPE-CVD CNTs increases screening effects is the primary cause of the lower field emission performance. However, this same control makes integration into electronic devices possible where the less controllable growth of the T-CVD process would potentially fail. Using the controllability of the MPE-CVD process to fabricate gated CNT arrays is discussed in detail in Chapter VI.

V. CNT Array Modeling and Simulation

Since de Heer *et al* demonstrated the field emission capabilities of carbon nanotubes with the fabrication of a small electron gun using multi-walled carbon nanotubes, CNTs have been the center of a many field emission research efforts [42]. The physical and electrical properties of CNTs that are favorable for field emission such as narrow diameters, high aspect ratios, high temperature stability, good conductivity, and structural strength are documented in Chapter II. CNT field emission devices are created in two configurations, diode and triode, shown in Figure 27. A triode design is preferable to a diode design for arrays primarily because the extraction voltage required is much lower due to the proximity of the gate to the CNTs. A triode design also has the potential to reduce screening effects which limit electron emission to a small fraction of the CNTs within the extraction electric field.

COMSOL finite element analysis software is used to simulate various diode and triode CNT array configurations to develop an optimized design for a gated CNT field emission array within the currently available fabrication capabilities. Carbon nanotube synthesis technology provides a method to control CNT height and to a minor extent areal density. Standard fabrication processes control the array element shape, dimensions, and pitch. The goal is to obtain high array current densities through maximizing the electric field strength at the tips of the CNTs by balancing the array element dimensions, pitch, and height. The effects of CNT separation on the electric field intensity are also simulated.

5.1. Carbon Nanotube Array Models

As mentioned above, there are a variety of properties that make CNTs well suited for field emission applications. However, field emission occurs primarily due to the physical dimensions of CNTs. Single walled CNTs have diameters from 0.6 nm to 1.4 nm and multi-walled CNTs can range from 12 nm to more than 100 nm in diameter. Both types of CNTs can range from tens of nanometers to microns and even millimeters in length resulting in incredible aspect ratios. The resulting focus of the electric field at the tips of the CNTs is often referred to as the electric field enhancement factor. Previous research as summarized by Bonard *et al* has shown multi-walled CNTs to be more robust emitters than single walled CNTs [49]. Multi-walled CNTs are also much easier to fabricate reliably, as such only multi-walled CNT dimensions are used in these models. While the conductivity of single walled CNTs can be metallic or semiconducting depending on the nanotube structure, all multi-walled CNTs are considered metallic conductors. With the physical geometry providing the primary enhancement of the electric field, the CNTs are treated as perfect conductors in the models.

A simple 2D model of a 1 x 3 element CNT array was used to investigate general trends, which were then confirmed with much more computationally complex 3D models. The initial 2D model, shown in Figure 53, was based on a fabrication process that consisted of a silicon (Si) substrate with a 200 Å titanium (Ti) diffusion layer followed by 100 Å nickel (Ni) catalyst layer. The nickel was covered with 2 µm of silicon dioxide (SiO₂) with 0.5 µm chrome gate metal on top. The array consists of 1 µm circular or square elements etched in the gate metal and SiO₂ with a 1 µm pitch. The

anode is located directly above and relatively far away (10-50 μm) from the CNT emitters so its contribution to the electric field is assumed to be small and uniform in nature. Thus, the anode is not included in the model.

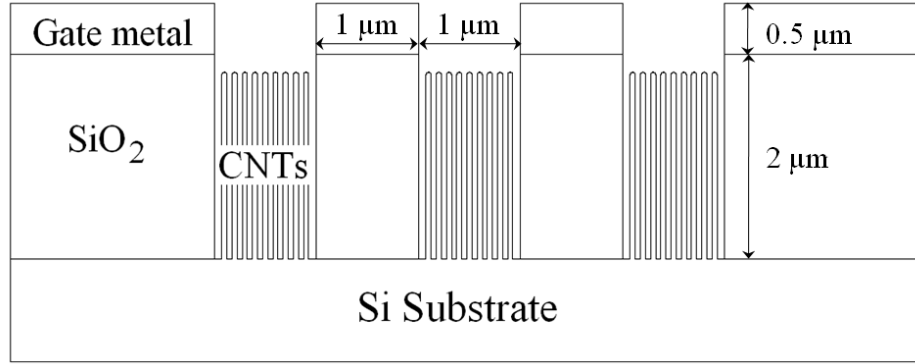


Figure 53. Basic 2D model of 1 μm x 3 gate array with 1 μm pitch.

The CNT films grown from the Ni catalyst via microwave plasma enhanced chemical vapor deposition result in closely packed CNTs with diameters of a fairly dispersive range, 10 - 100 nm. The process target is an average diameter of 50 nm, which is the diameter used in the simulations. The field enhancement will increase for smaller diameter CNTs and decrease for larger diameter CNTs.

Perhaps the most obvious approach to increasing the current density of an array is to decrease the array pitch. This will increase the number of elements across the array resulting in a higher total array current density. The effects of decreasing the spacing between gate openings was investigated by simulating 2D models with pitches of 3 μm , 2 μm , 1 μm , and 0.5 μm for both 1 μm and 0.5 μm array elements. Three dimensional simulations were also performed using 3x3 element arrays with 1 μm and 0.5 μm pitches.

The proximity of the gate to the CNT directly affects the electric field intensity. Thus, it's expected that decreasing the element dimensions will result in increased field

strength. The trade-off is fewer CNTs within the smaller element. However, within a given element only a fraction of the CNTs are expected to emit at any given time. This is caused by electrostatic screening which is described in detail below. Experimental results with decreasing larger element dimensions from $18\text{ }\mu\text{m}$ to $4\text{ }\mu\text{m}$ have shown increased field emission current densities [73]. The smallest feature size available in the current fabrication process is $0.5\text{ }\mu\text{m}$, so the electric field strength of $1\text{ }\mu\text{m}$ and $0.5\text{ }\mu\text{m}$ array elements were compared. 3D models were also created to compare the field strength of $1\text{ }\mu\text{m}$ and $0.5\text{ }\mu\text{m}$ circular and square elements. However, it should be noted that the processes available for this effort are capable of only $0.5\text{ }\mu\text{m}$ circular elements.

When de Heer *et al* first published the results of the first CNT field emission device, it was estimated that a mere 0.1 % of the total CNTs were emitting electrons. It is now widely accepted that this phenomenon is caused by electrostatic screening [10]. The CNTs are too close together for electrostatic field penetration which negates some of the expected field enhancement. As reported in Section 2.7.2, Nilsson *et al* conducted a study of screening effects for diode configured CNTs by performing 2D simulations of field penetration that concluded the optimum separation between individual CNTs was twice the CNT height [59]. 3D simulations performed by Smith *et al* showed 2D simulations underestimated the effects of screening and determined an optimized separation of 3 times the height of the individual CNTs. Neither of these optimized solutions is practical for large gated arrays as it would require e-beam lithography to pattern individual CNT growth sites within each element. Screening effects within the elements are unavoidable as the density of the CNTs can only be mildly influenced

during the synthesis process. However, the CNT spacing within an element was simulated at 50 nm, 200 nm, and with a single CNT to confirm electrostatic screening effects.

The limited electrostatic field penetration between densely grown CNTs introduces the possibility of improving the fabrication process by reducing the thickness of the dielectric layer and the height of the CNTs without any adverse effect on the electric field strength. As the feature sizes decrease; fabrication, especially etching, becomes more difficult unless there is a corresponding decrease in layer thicknesses. The dielectric thickness was simulated at 2 μm , 1 μm , and 0.5 μm with the CNT height adjusted accordingly. A dielectric thickness of 0.5 μm is probably not feasible due to the difficulty in reliably controlling CNT height below 0.5 μm .

Using the models and simulations discussed above, the optimization process can be summarized by varying these five parameters: CNT spacing, array pitch, array element dimensions, element shape, and dielectric thickness.

5.2. COMSOL Multi-physics

The COMSOL electrostatics of dielectric materials application was used to simulate the electric field generated by the gate extraction voltage across the CNTs within the array elements in both 2D and 3D. The models were created by subtracting the conductors (substrate, CNTs, gate) from a surrounding dielectric block of air and silicon dioxide. Subdomain properties were used to set the silicon dioxide permittivity at 3.9. Boundary conditions were used to ground the substrate and CNTs and put a 1 V potential

on the gate metal. Results were best visualized using contour and surface plots, while peak electric field magnitudes were recorded using point evaluations.

5.3. Simulation Results

Previous experimental and computer simulation research with diode configured CNTs indicated that relatively large spacing between the CNTs is necessary to avoid screening effects. These electrostatic screening effects are clearly evident in the simulation results shown in Figure 54. This simulation is of a $1\text{ }\mu\text{m}$ element with CNT spacing of 50 nm, 200 nm, and a single CNT in the center of the element. The simulation shows the equipotential lines of the electrostatic field with the background surface indicating the magnitude of the electric field.

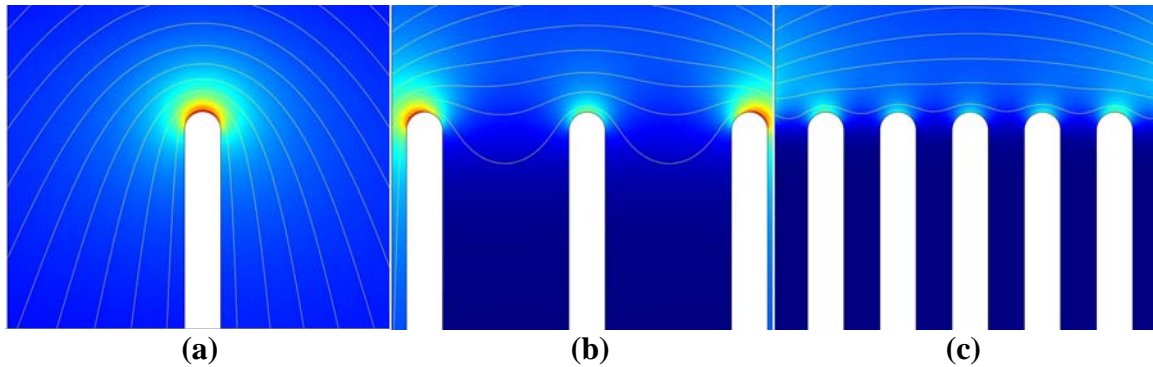


Figure 54. Screening effects for a) single CNT, b) 200 nm spacing, and c) 50 nm spacing.

The single CNT, shown in Figure 54 (a) clearly sees the most field penetration and correspondingly has the strongest electric field. There is a 42% reduction in electric field strength from the single CNT to the center CNT in Figure 54 (b) with neighboring CNTs 200 nm away. The magnitude of the electric field of the center CNT in Figure 54 (c) with 50 nm spacing is 60% less than the single CNT. The CNT spacing within each

element cannot be controlled precisely, so the electrostatic screening within each gate is unavoidable at this time.

Decreasing the array pitch poses the simplest method to increase the total current density of the array, as long as the reduced pitch does not cause screening effects between array elements. Results of array pitch simulations where the pitch of 1 μm and 0.5 μm element arrays were reduced from 3 μm to 0.5 μm are shown in Figure 55. The magnitude of the E-field at the tip of each CNT at each pitch is plotted. There is no reduction in magnitude across the center of each array element where the screening effects of immediately neighboring CNTs dominate. The 0.5 μm pitch causes a small reduction ($\sim 4\%$) in the E-field magnitude of the edge CNTs.

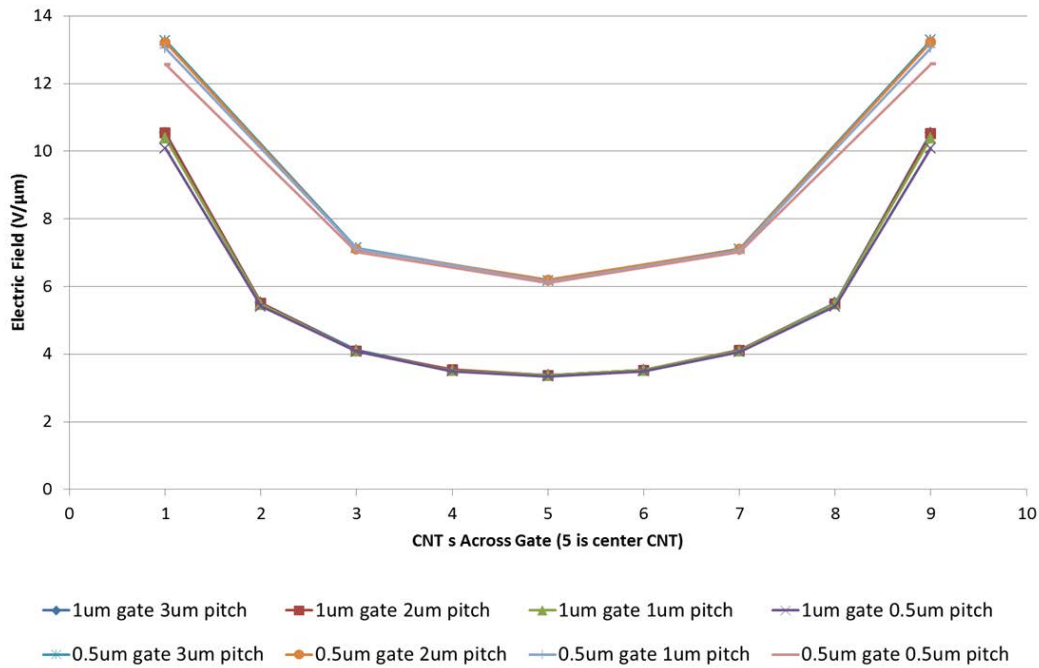


Figure 55. E-field magnitude at CNT tips of 1 μm and 0.5 μm element arrays with varying pitches.

3D simulations of a 3x3 0.5 μm element array with 1 μm and 0.5 μm pitches yielded similar results. Figure 56 shows the 3D model and the resulting E-field

magnitudes at the CNT tips of the center element. The scales are identical for both surface plots and show no discernable difference between the two pitches. Quantitative analysis across the entire array resulted in only a 2 % difference between the two arrays. Reducing the array pitch has little effect on the magnitude of the electric fields generated across each element; while the increased number of elements will result in larger total array current densities.

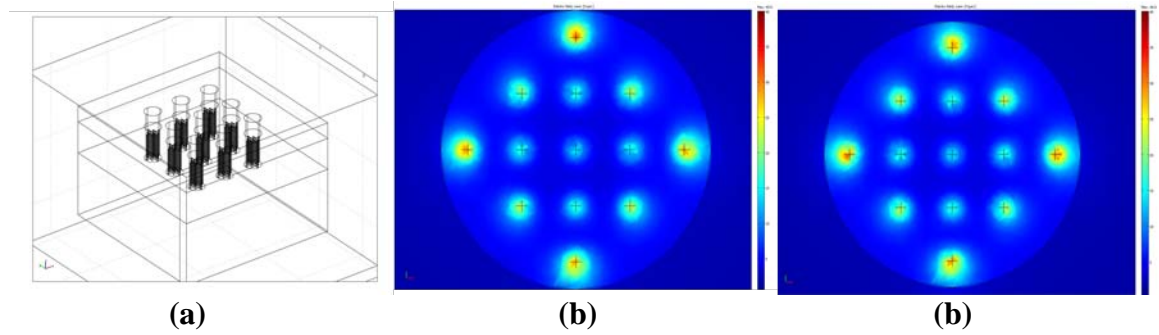


Figure 56. (a) 3x3 0.5 μm gated array with cross-section of E-field magnitude at CNT tips of the center element for (b) 0.5 μm and (c) 1 μm pitch.

Reducing the array element dimensions has the potential to increase over all array current density in two ways. First, smaller elements will increase the total number of elements across the array. Second, as shown in Figure 55, the decreased distance between the CNT emitters and the gate increases the electric field. The center CNT electric field magnitude increases almost two fold from 3.3 V/ μm to 6.1 V/ μm with the reduction in element dimension from 1 μm to 0.5 μm .

Three dimensional simulation results comparing elements of 1 μm and 0.5 μm showed greater increases in electric field strength. The E-field magnitude at the CNT tips shown in Figure 57 clearly shows an increase for both circular and square elements when the element dimension is reduced. The center CNTs of the 1 μm circular and square

elements have E-field magnitudes of $5.3 \text{ V}/\mu\text{m}$ and $7.8 \text{ V}/\mu\text{m}$ respectively. The center CNTs for the $0.5 \mu\text{m}$ circular and square elements increases to $14.7 \text{ V}/\mu\text{m}$ and $17.7 \text{ V}/\mu\text{m}$ respectively. Both 3D and 2D results confirm an increase in the electric field across the element with decreasing element dimensions.

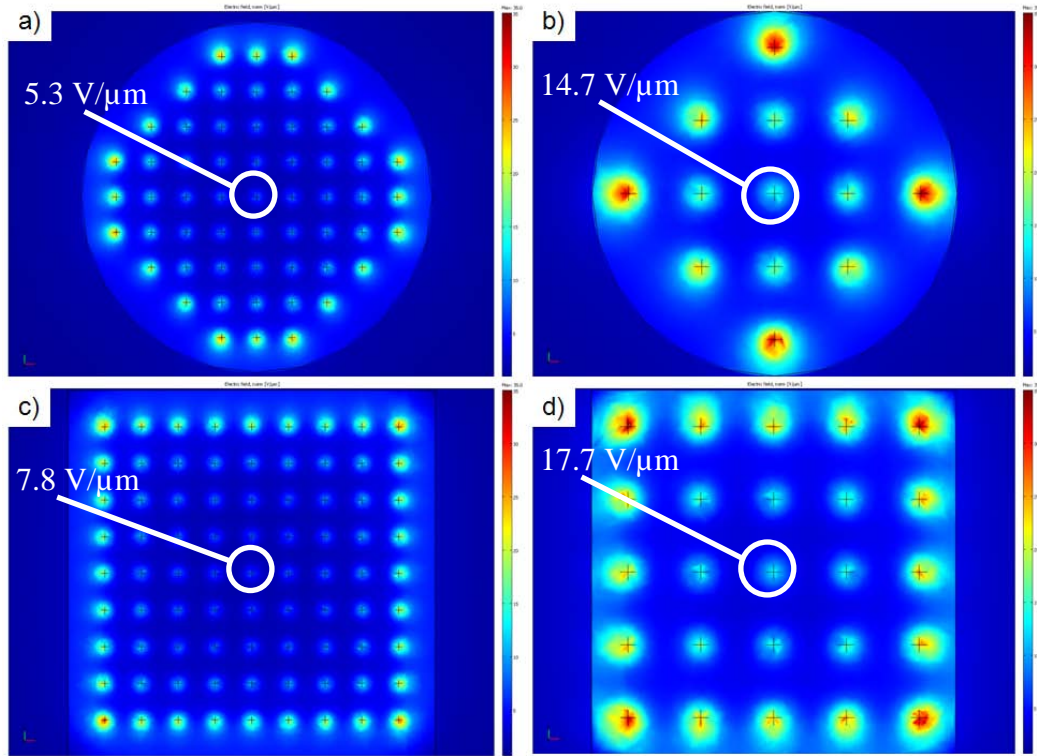


Figure 57. Cross-section of E-field magnitude at CNT tips of (a) $1 \mu\text{m}$ circular, (b) $0.5 \mu\text{m}$ circular, (c) $1 \mu\text{m}$ square, and (d) $0.5 \mu\text{m}$ square single elements.

These simulations also provided a comparison between square and round element shapes. It is interesting to note that in all cases, shown in Figure 57, the center CNT of the square element has a slightly higher E-field. In order to compare similar CNTs across both square and circular elements, CNTs were compared along the red lines in Figure 58. Both the $1 \mu\text{m}$ and $0.5 \mu\text{m}$ elements did not indicate a general increase in electric field strength. However, the square element has more CNTs with as strong and in the center slightly stronger electric fields than the circular element. Along the outer edge of the

element it could be argued that the CNTs in the square element are closer to the gate and will have a stronger electric field due to this proximity. By this same argument, the CNTs in the center of the square element are further from the gate than in the round element and the CNTs in the square element have more surrounding CNTs causing greater screening effects, so the center CNTs of the square element should have a lower field strength than the round element. Instead, there is a 38% difference between the 1 μm square and circular elements and a 9% difference for the 0.5 μm elements with the square element having the stronger electric field in both cases. This indicates that a square element is a better shape for the same feature size. Unfortunately, the fabrication processes currently available at the 0.5 μm feature size is limited to circular elements.

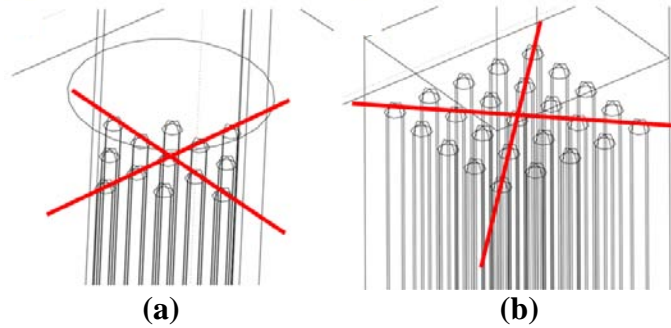


Figure 58. Method for comparing similar CNTs of circular and square elements.

Fabrication of small feature sizes, such as 0.5 μm elements with 0.5 μm pitch can be daunting when it requires etching through 2 μm of dielectric material. The last set of simulations compares the electric field across the 0.5 μm elements with 0.5 μm pitch when the SiO_2 dielectric layer is 2 μm , 1 μm , and 0.5 μm . The height of the CNTs is adjusted accordingly as well. Figure 55 shows a small reduction in the outside electric field strength at the 0.5 μm pitch due to element to element screening effects. After

accounting for this slight reduction, results of 2D simulations in Figure 59 show no electric field degradation regardless of the SiO₂ thickness.

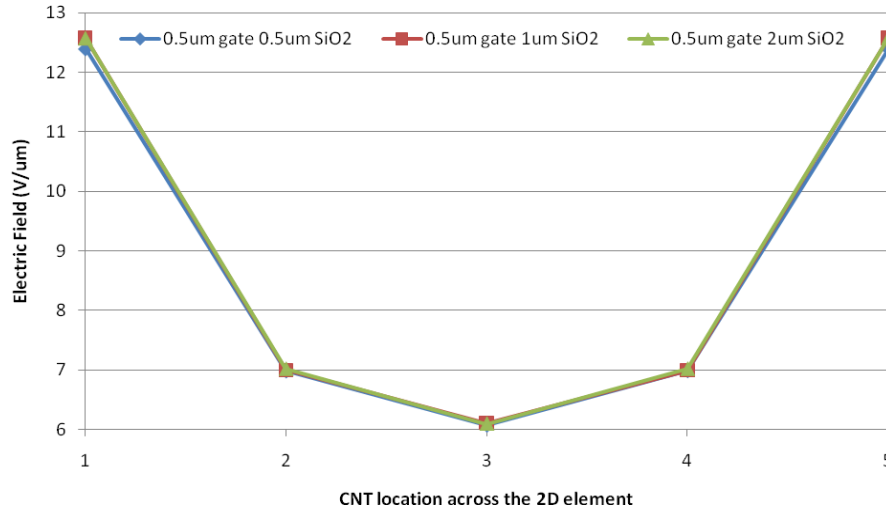


Figure 59. E-field magnitude at CNT tips across 2D element for dielectric thicknesses of 0.5 μm , 1 μm , and 2 μm .

Corresponding 3D simulations of 3x3 arrays with 0.5 μm circular elements and 0.5 μm pitch are shown in Figure 60. Figure 60 (a) is the results for the 0.5 μm dielectric thickness and shows a slight decrease in the electric field from the other two cases. The magnitude at the center is ~10 % less with the edges decreasing by smaller amounts. There is virtually no difference between the 1 μm and 2 μm dielectric thickness results. Reducing the dielectric thickness to improve fabrication reliability should not degrade the field emission properties of the resulting arrays.

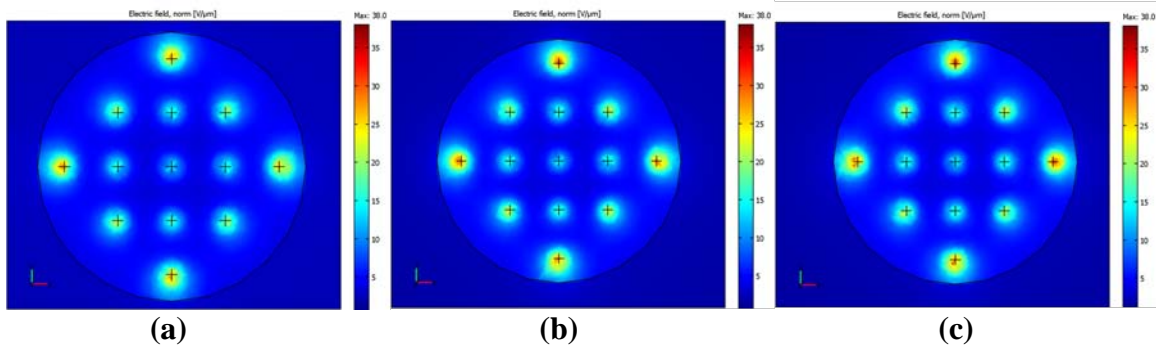


Figure 60. Cross-section of E-field magnitude at CNT tips of the center element of 3x3 array with SiO₂ thickness of (a) 0.5 μm , (b) 1 μm , and (c) 2 μm .

5.4. Summary

Carbon nanotubes have unique physical and electrical properties making them exceptional field emitters. COMSOL multi-physics has been used to optimize the physical dimensions for CNT field emission arrays. Five relatively simple parametric studies were performed to provide important insights into the design of field emission arrays within fabrication capabilities.

First and foremost, these simulations have shown that the electrostatic screening between CNTs within an array element is the dominating factor of the electric field magnitude. Any adjustments to the CNT synthesis process that can increase the carbon nanotube spacing will increase the electrostatic field penetration between CNTs and increase the local electric field magnitude. The screening effect is so dominant within the array elements that the pitch can be reduced significantly without adversely affecting the electric field magnitude at the CNT tips. Reducing the pitch will increase total array current density by increasing the total number of array elements. The same principle applies to the element dimensions. Reducing the element dimensions results in stronger electric fields and increases the total number of elements, both of which will increase

overall current density. The simulation results of element shape showed that a square element will potentially provide a better array fill factor without degrading the electric field strength; making it a better choice over a circular element of the same diameter. Finally, due to the dominant screening effects, the dielectric layer thickness and CNT height can be reduced significantly without decreasing the electric field strength.

The resulting optimized CNT field emission array, shown below in Figure 61, that fits within current fabrication capabilities available for this research effort consists of a $0.5\ \mu\text{m}$ circular element array with $0.5\ \mu\text{m}$ pitch. The SiO_2 dielectric layer can be reduced to $1\ \mu\text{m}$ with a corresponding CNT height between $0.5\ \mu\text{m}$ and $0.8\ \mu\text{m}$. The simulation results indicated a square element will perform better than a circular element. However, due to limitations of the current fabrication process, a circular element is used in the final design.

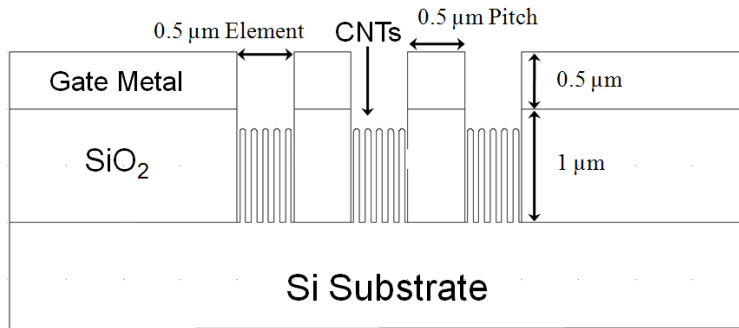


Figure 61. Optimized CNT field emission array basic schematic.

VI. CNT Field Emission Array Fabrication

CNT field emission can be achieved with either diode or triode configurations, both are shown in Figure 27. For reasons explained in Sections 2.7 and 5.4, a triode device is the preferred configuration. But, the diode configuration is also used for its simplicity and to characterize the field emission properties of CNT carpets avoiding the complexities of complete device fabrication. Field emission using this configuration requires relative high voltages to establish the necessary electric fields, due to the relatively large distance between cathode and anode. The diode configuration for this research required no fabrication beyond the deposition of the barrier and catalyst layers on the substrate followed by CNT synthesis. The CNT carpet then becomes the cathode and the field emission test apparatus places the copper anode above the CNT carpet.

Two processes were developed for fabricating triode devices. The first is a conventional photolithographic process, first developed at AFIT by Kossler [63]. The photolithographic process is mature and reliable, but limited in feature size to $\sim 1\text{-}2\text{ }\mu\text{m}$. The second process utilizes a novel patterning method called nanosphere lithography capable of feature sizes in the 10's of nanometers [75]. For both processes the anode is omitted, the ability to flip-chip bond the anode to the device has been demonstrated but was not required for the desired application and for test purposes the test apparatus supplied the anode. Detailed descriptions and the resulting devices are described in detail below.

6.1. Photolithography Process

A triode based field emission array test device was designed and all processing steps completed except aligned CNT growth. The gate masks for the photolithographic fabricated test devices consisted of an array area of 1 cm^2 with large 0.5 cm^2 contact areas for both the gate metal and catalyst/barrier metal. The array elements consisted of circles or squares with dimensions of 2, 4, 8, or $16 \mu\text{m}$ with element pitch also ranging from 2 to $16 \mu\text{m}$. The varying element shapes, dimensions, and pitches were designed to facilitate an experimental parametric study similar to the COMSOL simulations previously described.

The fabrication process is shown in Figure 62. The triode based device is fabricated on silicon by first depositing a titanium barrier layer of 200 \AA followed by the Ni catalyst layer ($50 - 200 \text{ \AA}$) via DC magnetron sputtering. The dielectric is sputtered SiO_2 , $1\text{-}2 \mu\text{m}$ thick with the final gate metal of 1000 \AA of chrome. The final prepared substrate with all layers deposited is represented in Figure 62 (a). After all materials are deposited, the gate

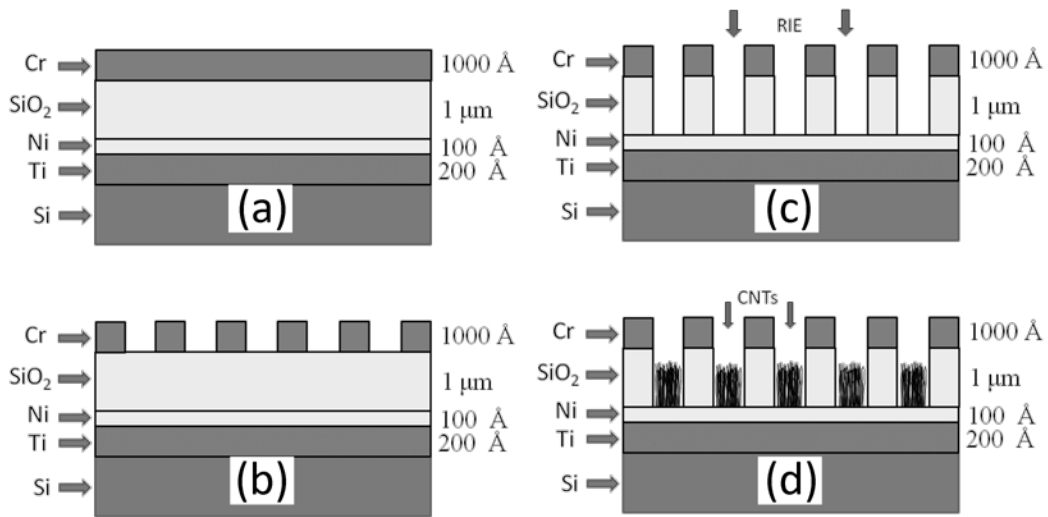


Figure 62. CNT field emission device photolithographic fabrication process.

mask is used to pattern and etch the chrome layer as shown in Figure 62 (b). The chrome and photoresist act as a mask and the nickel catalyst layer acts as an etch stop for the reactive ion etching (RIE) process that removes the SiO_2 , see Figure 62 (c). The final step for a complete device, shown in Figure 62 (d), is CNT growth which is detailed in Chapter III. Figure 63 provides images of a completed triode device at increasing magnifications.

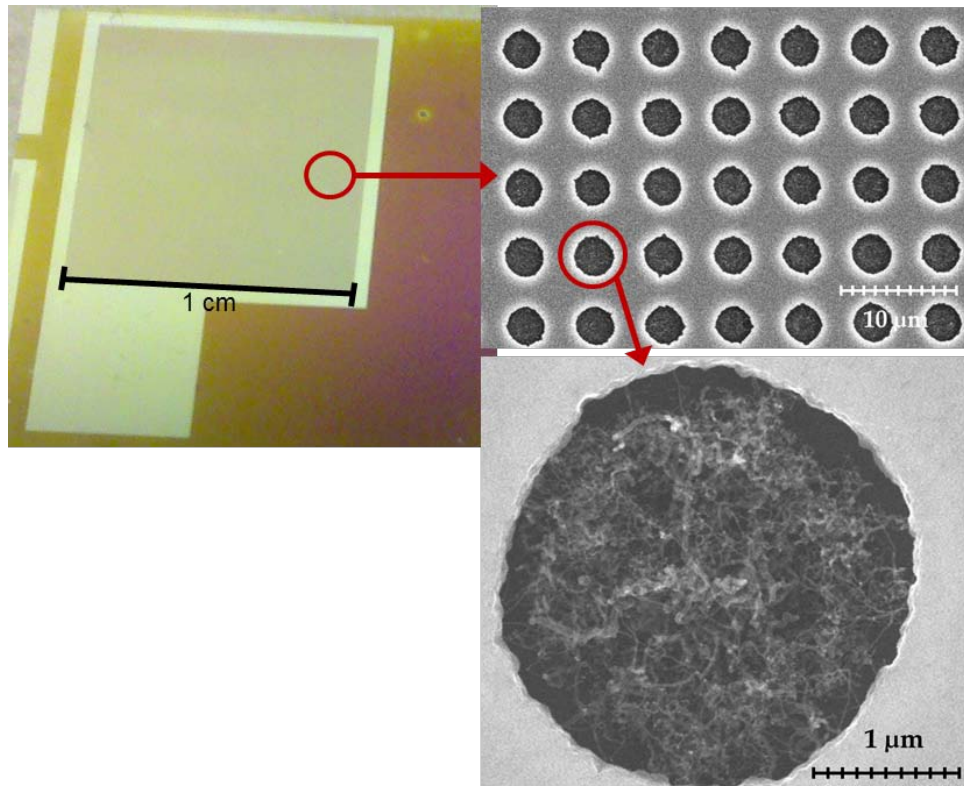


Figure 63. Triode device fabricated by photolithographic process.

6.2. Nanosphere Lithography

Nanosphere lithography was used to fabricate a CNT field emission array matching the physical dimensions of the optimized design from the parametric study simulations. A schematic of the optimized array is shown in Figure 61 with the physical dimensions labeled. The concept of nanosphere lithography was introduced in Chapter II with the

discussion on depositing a monolayer of nanospheres across a substrate. In the application discussed the polystyrene nanospheres were used as a mask to deposit nanoparticles of Ni catalyst for sparse CNT growth. This same nanosphere lithography process is applied but the nanospheres are used as a mask for the array elements for the optimized triode device. This novel masking method was chosen as an inexpensive, simple process for achieving the 0.5 μm gate elements and pitch desired with the potential for much smaller dimensions in the future.

The concept for nanosphere lithography was first proposed by Fischer and Zingsheim in 1981 when they used 312 nm latex spheres to achieve contact imaging with submicroscopic resolution [76]. Shortly thereafter, Deckman and Dunsmuir demonstrated the use of polystyrene nanospheres as an etching or deposition mask which they dubbed natural lithography [77]. Haginoya *et al* furthered the development of nanosphere lithography by investigating the effects of oxygen RIE on a Polystyrene (PS) monolayer. The RIE process effectively etched the PS allowing the diameter to be accurately adjusted. The following relationship between the desired diameter, d , and the RIE time, t , was approximated [78].

$$d = d_0 \cos \left\{ \cos^{-1} \left(\frac{kt}{2d_0} \right) \right\} \quad (19)$$

Where d_0 is the initial colloid diameter and k is a process specific constant that must be determined through experimentation. The relationship shows that as the diameter decreases the polystyrene etch rate increases significantly. Since these early efforts, monolayers and dual layers of PS nanospheres combined with angled deposition of

subsequent materials have been used to fabricate complex periodic arrays for a number of potential applications from nanoscale optics to magnetic memory [79].

Nanosphere lithography has well documented issues stemming from the fact that the monolayer is a “naturally” forming 2-D crystal. The first issue is depositing the polystyrene colloids in a manner conducive to self-assembly or natural formation. The second is the unavoidable defects that occur during self-assembly such as point defects or vacancies, line defects, and polycrystalline domains [79]. Figure 64 shows a relatively large area of a 1 μm sphere monolayer. The defects are easily identified in SEM images because of reflection at defect edges resulting in bright lines in the monolayer structure.

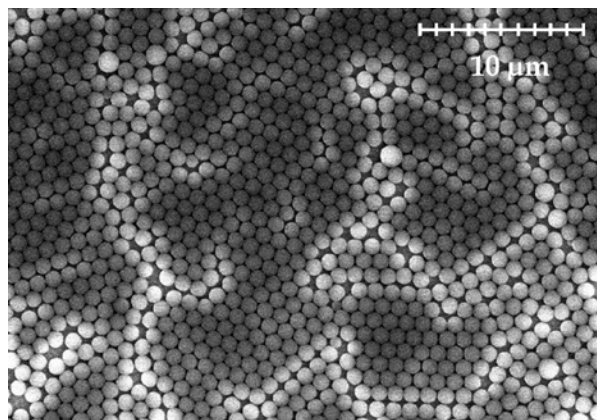


Figure 64. SEM image of 1 μm sphere monolayer. Bright lines indicate 2D crystalline defects.

There are two primary methods of depositing nanospheres, spin coating and drop coating. Spin coating utilizes a typical photoresist spinner and PS nanospheres suspended in water or a water and isopropyl alcohol mixture. Self-assembly will only occur if the polystyrene mixture wets to the substrate surface; so a hydrophilic surface is required. The addition of isopropyl alcohol helps the solution wet to the surface and increases evaporation which decreases the spin time required to dry the substrate after

application. Drop coating consists of submersing the hydrophilic substrate into water at a slight angle then adding a solution of PS nanospheres, water, isopropyl alcohol or methanol. The nanospheres form a monolayer on the surface of the water. At this point self-assembly will occur and can be enhanced by decreasing the surface tension of the water with the addition of a surfactant [39]. The actual deposition of the monolayer is accomplished by letting the water evaporate, lifting the substrate out of the water, or draining the water from the container. Whichever method is selected, it must be performed in a manner that does not disturb the delicate monolayer suspended on the surface of the water. The more complex drop coating processes usually result in larger defect free areas, but regardless of the method used defect free areas of more than 100 μm^2 are rare [79].

The PS is easily removed with either wet or dry etching processes. Solvents like toluene and acetone are effective wet etchants for polystyrene. Wet etchants are typically coupled with an ultrasonic bath to prevent any dissolved PS residue or deposited material intended for lift-off from remaining on the substrate. Oxygen RIE has already been mentioned as a dry etchant for PS. It is also possible to remove PS with an oxygen plasma ash. Using the nanosphere lithography processes described above a complete fabrication process for a sub-micron gated CNT field emission array was developed.

6.2.1. Fabrication Process

The fabrication process as shown in Figure 65 will focus on the nanosphere lithography aspects. A brief description of the necessary process steps leading up to Figure 65 (a) follows. A silicon substrate is prepared by first sputtering a 200 Å titanium

thin film to aid in adhesion and act as a diffusion barrier. Next a 100 Å Ni thin film is sputtered to act as the CNT catalyst. This is followed by 1 µm of SiO₂ which provides the necessary dielectric separation between the gate metal and the CNTs.

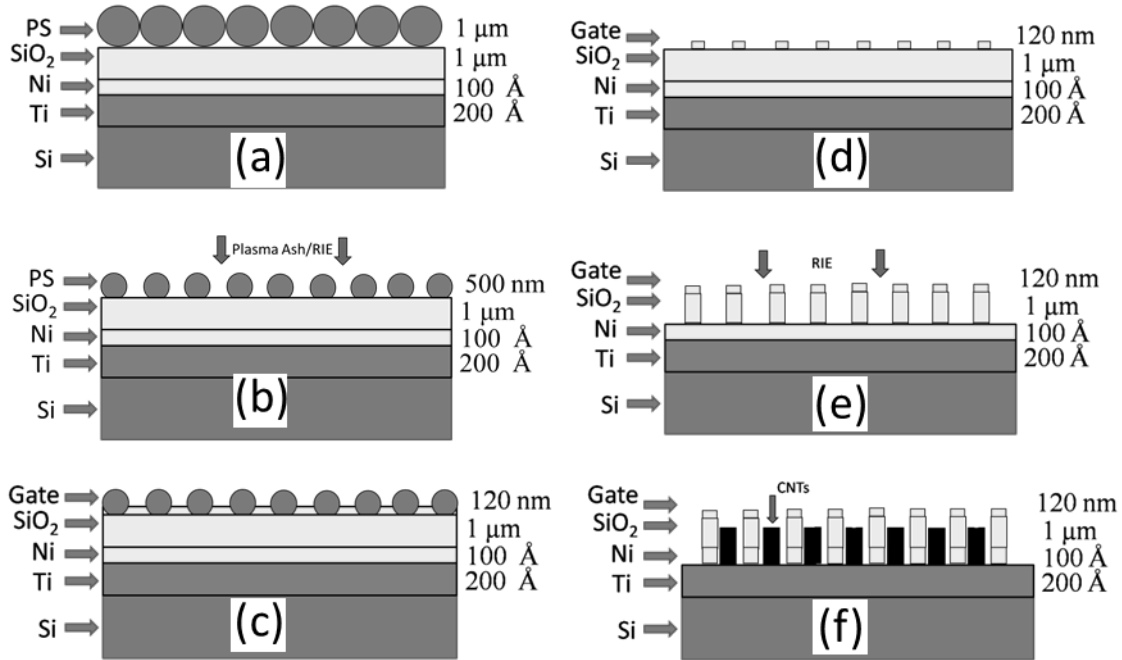


Figure 65. Complete device fabrication process; a) PS mask deposit on prepared substrate; b) Plasma ash or RIE to reduce PS size; c) deposition of gate metal via evaporation; d) removal of PS mask with ultrasonic acetone bath; e) RIE to remove SiO₂; f) MPE-CVD growth of CNTs.

The two key steps in this process are getting the PS monolayer deposited across the dielectric layer, both drop coating and spin coating methods were used. And the etch method employed to reduce the size of the individual PS colloids; again both plasma ashing and RIE were used. Thus, essentially two fabrication processes were developed one utilizing drop coating and plasma ashing and a second consisting of spin coating and reactive ion etching.

6.2.1.1. Drop Coating Process

The first drop coating process consisted of mixing the nanosphere solution 1:1 with isopropyl alcohol. The nanospheres are 10 % solid in a water solution. Using a small pipette the nanosphere/water/isopropyl solution is dropped on the SiO₂ layer. The surface must be hydrophilic for the solution to wet to it and the monolayer to form. SiO₂ should naturally be hydrophilic, but a short plasma ash is performed to both clean the wafer and ensure the surface is hydrophilic. The wafer must be resting at a slight angle (20° - 40°) with one edge submerged in DI water. The solution must be added right where the DI water meets the Si wafer. The isopropyl alcohol causes rapid evaporation and helps both keep the nanospheres on the DI water surface forming a monolayer and facilitates evaporation and capillary action which draws the nanosphere monolayer up the Si wafer. The resulting film is then allowed to air dry. The process is fairly crude and only works a small fraction of the times attempted. However, the actual deposition either works and the total process occurs in less than 1 minute or it doesn't work and the wafer can be cleaned by rinsing in DI water. Then the process can be attempted again in less than 1 minute. Although not attempted for this effort, it has been reported that the addition of small amounts of sodium dodecyl sulfate, a common surfactant, improves both the deposition success rate and the self-assembled monolayer quality [39]. The sodium dodecyl sulfate, a common ingredient in dish soaps, reduces the surface tension of the water allowing larger defect free monolayers to form.

The drop coating deposition and plasma etching of 1 μm spheres was accomplished with mixed results. The deposition process resulted in large wafer areas being coated

with a monolayer but the defect density was very high. Figure 66 (a) shows a very good close up of a virtually defect free area, while Figure 66 (b) shows the many defects and breaks in the monolayer after zooming out only four times. Large areas 2 - 5 cm² were covered with the 1 μ m sphere monolayer, but a defect free area of 20 μ m² or larger could not be found.

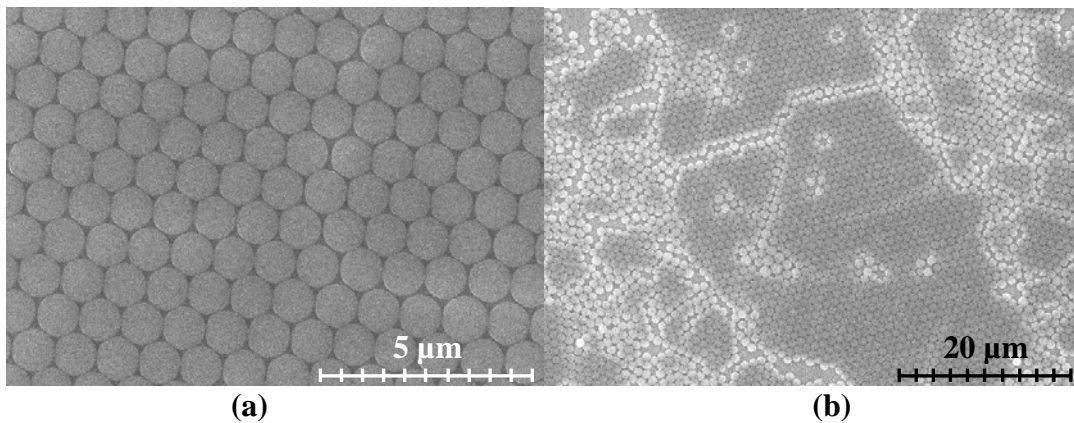


Figure 66. SEM images of 1 μ m sphere monolayer a) close up on defect free area and b) large area showing high defect density.

The 1 μ m diameter spheres were etched in the oxygen plasma asher at 100 W for 20 min. The goal was a reduction in diameter from 1 μ m to 500 nm. Figure 67 (a) shows that the etch was too much reducing the spheres to approximately 400 nm. The expectation was that van der Waals forces would hold the spheres to the substrate, so that a uniform distribution would be maintained. Figure 67 (b) shows a few spheres, like those in the lower left corner, that still seem to be ordered. The vast majority of the spheres look randomly distributed with many apparently sticking to each other better than to the substrate. Efforts to improve on the quality of the PS monolayers using this relatively crude drop coating method were not productive, so only the more promising spin coating method was continued.

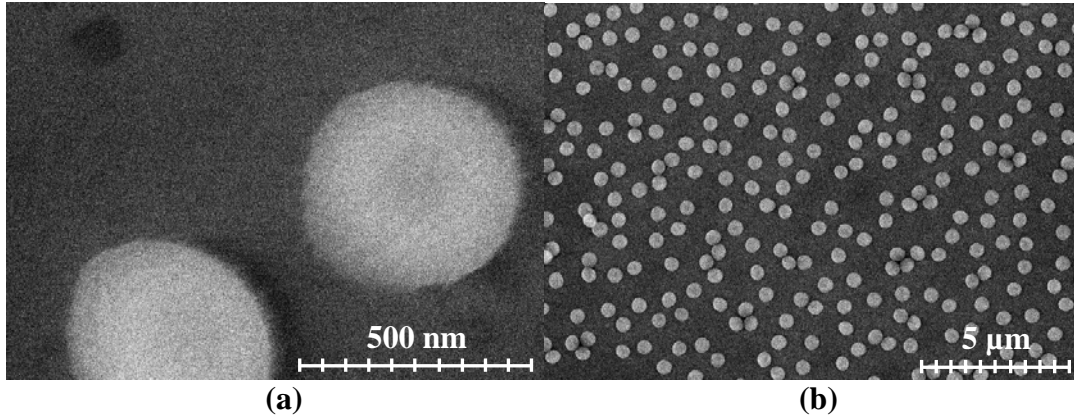


Figure 67. SEM images of oxygen plasma etched 1 μm spheres a) close up and b) zoomed out to larger area.

6.2.1.2. Spin Coating Process

This particular application does not require a defect free 2-D crystal lattice as a defect will only slightly increase the area of the gate metal. However, the defect density of the drop coating method described above was unacceptable. Thus, the simpler and significantly faster spin coating method was selected as the deposition method of choice. Spin coating allows quick application of the PS solution and if the result is poor, the sample can be cleaned and the solution reapplied while remaining on the spinner.

The spin coating process used begins with substrate preparation. The silicon dioxide surface of the substrate is thoroughly cleaned using an acetone, methanol, DI water rinse. The substrate is then cleaned and made hydrophilic with a 5 minute oxygen plasma ash at 75 W. The PS nanospheres (10 wt. %) are packaged suspended in DI water. The PS/DI solution is mixed in equal parts (1:1) with isopropyl alcohol. A small amount of solution is applied to the prepared substrate via pipette and the spin process is started. The spin process consists of a spreading speed of 400 to 800 rpm for 40 seconds followed by a gradual increase over 30 seconds to 2000 rpm until dry (60-70 sec).

Figure 65 (b) shows the PS nanospheres being reduced by oxygen plasma ashing or oxygen RIE. Plasma ashing is effective at etching PS and was initially chosen over RIE due to laboratory availability. The plasma ash was performed at 25 W for 7 min to reduce 1 μm diameter PS to 500 nm, 5 min to reduce 760 nm diameter PS to 500 nm, and 3 min to reduce 500 nm diameter PS to 250 nm.

The process step shown in Figure 65 (c) is the deposition of the gate metal. The gate metal is 1200 Å of chrome. The gate metal is deposited by e-beam evaporation without rotation to facilitate the lift-off step. Removal of the PS mask and gate metal lift-off is accomplished with an ultrasonic acetone bath for 8 minutes followed by an acetone-methanol-DI water clean. The result of the lift off is represented by Figure 65 (d).

Next the gate metal forms a mask for the SiO_2 etch shown in Figure 65 (e). The 1 μm of SiO_2 is etched by RIE at 90 W for 20 minutes. This exposes the Ni catalyst layer, which also acts as an etch stop for the RIE process. Finally, the device is completed with the growth of carbon nanotubes from the Ni catalyst as shown in Figure 65 (f).

6.2.1.3. Spin Coating Results

As mentioned above, the difficult part of nanosphere lithography is the deposition. Developing an effective spin coat process required extensive experimentation. The final spin coating process yielded acceptable results. The difference in spreading speed required is dependent on the sample size. Successful application was repeatedly achieved for 1.5-2 cm^2 samples with a spreading speed of 400 rpm, but for smaller samples 1 cm^2 or less it was necessary to increase the spreading speed. Deckman and Dunsmuir also

used spin coating and noted that PS nanospheres between 300 nm and 800 nm were more successful with spin coating than larger or smaller diameters [77]. Although their process was different, the results were similar. The deposition of 760 nm and 500 nm nanospheres had better coverage and fewer defects than the 1 μm nanospheres. An attempt to deposit 100 nm nanospheres using the above process was completely unsuccessful resulting in a multilayer film across the sample. This is most likely because the Van Der Waals forces between these small PS colloids are significant. A surfactant, as mentioned above, could be used to improve the process for smaller diameter PS nanospheres.

The spin coating process developed was used successfully to mask samples from 1 – 2 cm^2 with PS nanospheres 1 μm , 760 nm, and 500 nm in diameter. Figure 68 shows a relatively defect free area of a monolayer of 500 nm diameter nanospheres. Even though there are clearly many line dislocation and polycrystalline boundary defects this monolayer is acceptable for the current application.

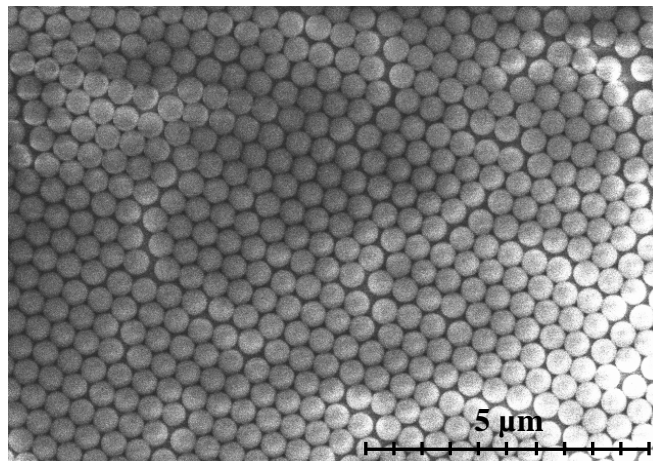


Figure 68. Monolayer of 500 nm diameter PS spheres self-assembled into 2-D crystal lattice by spin coating.

The oxygen plasma asher was effective at etching the PS nanospheres and after backing out a processing constant k of 3.9 using Equation (19), the etch rates matched the approximate relationship developed by Haginoya *et al.* One issue with using a plasma ash for diameter control is a PS bridge phenomenon where neighboring spheres seem to be connected by a melted PS bridge stretching between them. This phenomenon is not uncommon and has been exploited to create novel masking effects [81]. Reducing the power of the plasma ash from 75 W to 25 W reduced the phenomenon, but did not eliminate it entirely. Figure 69 (a) shows 1 μm PS nanospheres after plasma ashing with a resulting diameter of 500 nm. The bridge phenomenon can be seen in several places in the SEM micrograph. A bigger issue occurred with the plasma ashing of the 500 nm PS which may be related to the PS bridging. The 500 nm PS appear to adhere to each other better than they adhere to the substrate resulting in small groups of three and four etched PS nanospheres as shown in Figure 69 (b). With the exception of the bridge phenomenon, the plasma asher worked for both 1 μm and 760 nm PS, but is most likely an unacceptable etch process for the 500 nm PS. Using RIE Haginoya *et al* were able to etch 200 nm PS nanospheres down to 82 nm while still maintaining the original periodic spacing [78]. Oxygen RIE proved to be much more reliable with more repeatable results than plasma ashing. Figure 69 (c) shows 1 μm PS after 3 min and 30 sec RIE at 90 W with no evidence of the bridge phenomenon and the process was much less dependent upon the placement of the specimen in the system than with the plasma asher.

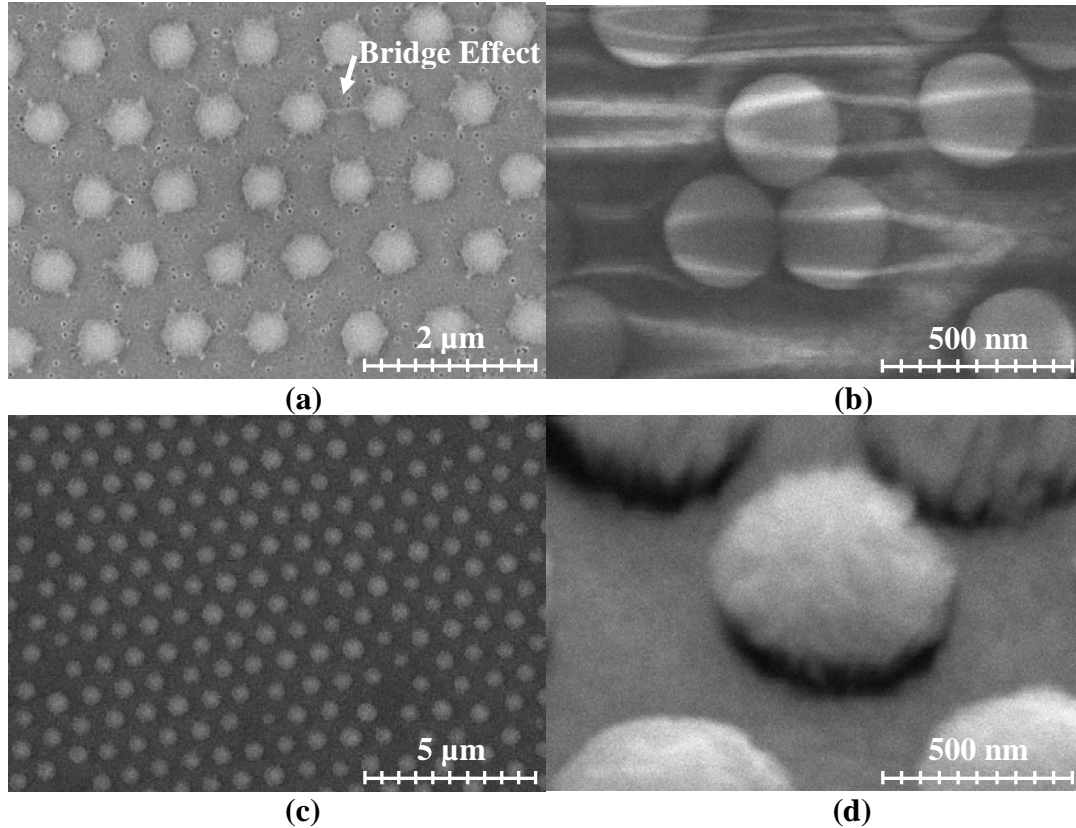


Figure 69. a) 1 μm PS nanospheres after plasma ashing; b) 500 nm PS nanospheres after plasma ashing; (c) 1 μm PS nanospheres after RIE; (d) 1 μm PS nanosphere with 120 nm Cr cap.

The curvature of the nanosphere coupled with the straight-on non-uniform deposition properties of evaporation result in a cap of Cr on top of the colloids that is not connected to the Cr layer on the substrate. This Cr cap effect, shown clearly in Figure 69 (d), facilitates an acetone lift-off of the Cr. The gate metal thickness is limited by the size of the PS colloids after etching. As a general rule the gate metal must be less than $1/4^{\text{th}}$ of the colloid diameter after etching. In this case, the colloids were initially 1 μm in diameter, after etching the colloids were reduced to 500 nm. The undercut curvature of the colloids nominally begins half-way up the colloid or at 250 nm. In order to ensure a gap between the Cr cap and the Cr deposited on the substrate, 120 nm of Cr was

deposited nominally leaving a 130 nm gap. Figure 69 (d) shows that the actual gap is closer to 100 nm or less. In some instances the gap was bridged by the Cr preventing lift-off and resulting in the Cr cap remaining, see Figure 70 (a). The removal of the PS mask and excess gate metal is accomplished with acetone, which dissolves the PS, in an ultrasonic bath. The lift-off is followed immediately with an acetone-methanol-DI water rinse to clean the sample. Efforts of removal using only an acetone bath and a cotton swab resulted in large amounts of metal debris from the dissolved PS coating the sample surface. Even with the ultrasonic bath and subsequent rinse there is still some debris present, but the sample surfaces are much improved. Figure 70 (a) shows a sample after ultrasonic acetone bath and cleaning rinse. The lift-off process has proven adequate when combined with the ultrasonic bath.

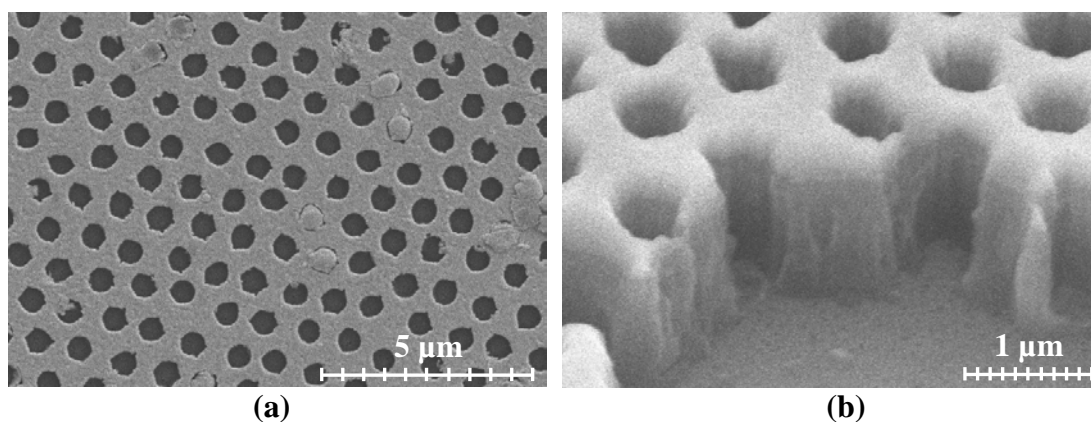


Figure 70. (a) 500 nm gate mask after PS release; (b) 500 nm gate after RIE.

The RIE of silicon dioxide through the gate mask is a mature process from previous fabrication efforts and worked well as shown in Figure 70 (b). A profilometer was used to confirm the etch depth on a larger gate metal opening for test purposes. The same opening was used to test for the presence of the Ni catalyst using conductivity measurements. Subsequent growth of CNTs also confirmed the presence of the Ni

catalyst. Figure 71 shows a single gate opening with CNTs grown in the MPE-CVD system using the recipe described previously. The growth time was 2 minutes and the CNTs are much too tall, reaching and extending beyond the gate metal. The CNTs are also not well aligned, but CNTs can emit electrons from the side walls as easily as the tips. Thus, vertically aligned CNTs are desirable for emission enhancement and efficiency but are not required for field emission.

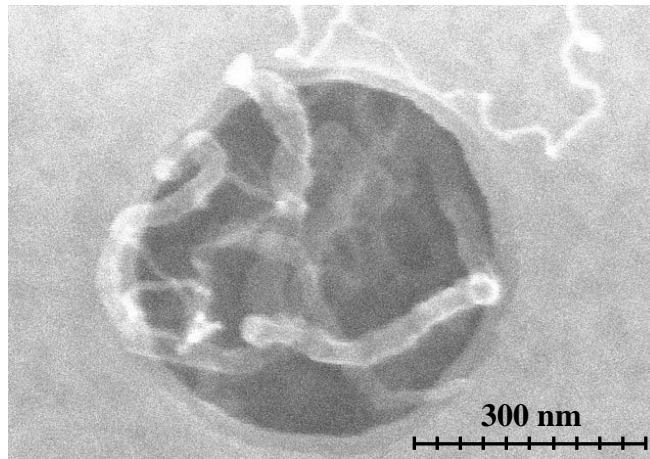


Figure 71. Single array element with CNTs.

6.2.1.4. Nanosphere Lithography Process Summary

A complete fabrication process using nanosphere lithography to fabricate the optimized sub-micron gated CNT field emission array has been described and each step in the process demonstrated successfully. Nanosphere lithography provides an inexpensive, simple method of achieving sub-micron gate features. There are unavoidable problems with nanosphere lithography chiefly monolayer deposition difficulties and monolayer defects. This form of lithography may not be feasible for large scale automated fabrication, but it provides an excellent method for proof of

concept research by achieving feature sizes beyond the capabilities of standard photolithography.

Steps in the nanosphere lithography process that should be improved were highlighted. The spin coating deposition method is simple and fast but not effective for smaller diameter PS nanospheres. For PS with diameters below 300 nm, a reliable drop coating method is necessary. Oxygen plasma ashing can be used to etch PS nanospheres, but oxygen RIE proved to be a more repeatable process. The current fabrication process was adequate for the production of the designed 500 nm gated CNT field emission array. There is also potential for significantly smaller gate openings, even to the point of limiting CNT growth to a single CNT per element.

6.3. Field Emission

Unfortunately, due to fabrication errors the devices were not capable of triode operation. Figure 71 shows that the CNTs are clearly too long and have extended beyond the gate metal. Resistance measurements confirmed a low resistance short between the substrate and gate. The devices were still capable of field emission in a diode configuration. Instead of assessing the performance of gated field emission devices, the screening effects of a grounded gate structure were studied.

Three working devices were compared. The first was an un-patterned CNT carpet. The second was the gated device in Figure 63. This device consists of a 1 cm^2 array of $4\text{ }\mu\text{m}$ round elements with a $4\text{ }\mu\text{m}$ pitch. This device also had a low resistance short between the substrate and gate metal after fabrication. The third device was the 500 nm

gated device fabricated using nanosphere lithography shown in Figure 71. Carbon nanotubes for all three devices were grown via MPE-CVD.

Device testing was conducted according to the test procedures explained in Section 4.4.2. The field emission test data is displayed in Figure 72 with the $10 \mu\text{A}/\text{cm}^2$ turn-on current density marked. The turn-on electric field for each device was $2.1 \text{ V}/\mu\text{m}$ for the $4 \mu\text{m}$ gated device, $2.47 \text{ V}/\mu\text{m}$ for the CNT carpet, and $2.84 \text{ V}/\mu\text{m}$ for the 500 nm gated device. The peak current density for the CNT carpet and 500 nm gated device can be seen in Figure 72 at $147 \mu\text{A}/\text{cm}^2$ and $112 \mu\text{A}/\text{cm}^2$ respectively. The $4 \mu\text{m}$ gated device had a peak current density of $267 \mu\text{A}/\text{cm}^2$.

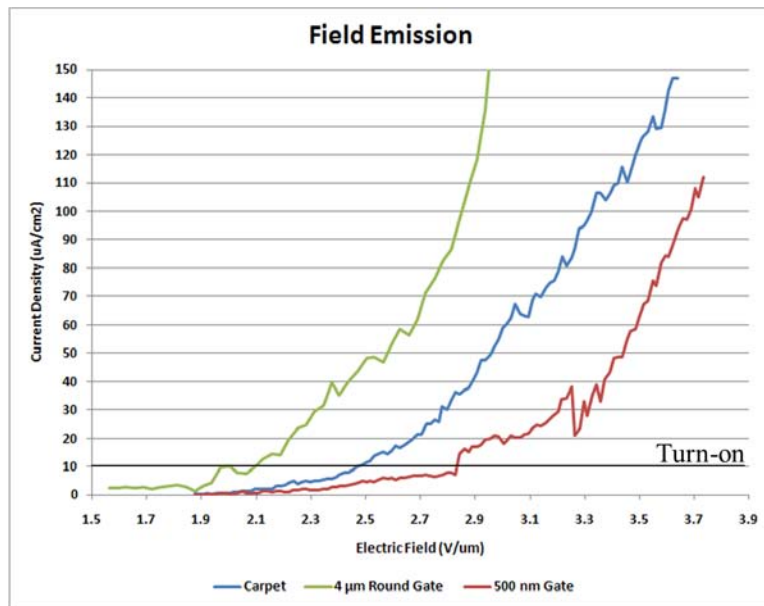


Figure 72. Field emission test of gated devices.

The $4 \mu\text{m}$ gated device performed the best out of the three devices with a lower turn-on electric field and higher maximum current density. The better performance can be ascribed in some part to a reduction in screening effects between the array elements caused by the grounded gate structure. The 500 nm gated device performs the worst for a

couple of reasons. Screening effects may be the biggest cause of poor performance. The 500 nm elements are small enough that the grounded gate is most likely screening the entire element reducing the field enhancement effect of the few CNTs within each element. A second reason for the poor performance might be a result of the limited number of CNTs per element across the array.

6.4. Summary

This chapter tied the various aspects of this research effort together to fabricate gated field emission devices. The MPE-CVD synthesis method was used for CNT growth. Gated devices were fabricated using both conventional photolithography and a novel nanosphere lithography process. The nanosphere lithography process provided an inexpensive method to achieve the sub-micron features required for the optimized device design developed in Chapter V. All fabrication steps for the gated arrays were demonstrated and prototype devices fabricated and tested. Although, not fully functioning triode devices, the devices tested provided valuable insight into electrostatic screening effects and validated the results of the modeling and simulation that showed a reduction in screening effects between elements in an array.

VII. Conclusions

One of the primary goals of this research effort was to develop a reliable CNT synthesis process. This goal was met with two separate CVD synthesis methods. The first CNT growth process was via MPE-CVD. Detailed research into the process revealed the specificity of a process recipe. It was shown that changes in barrier and catalyst material have significant effects on the growth process, so much so, that even changes in the deposition method from sputtering to evaporation of the same barrier and catalyst material requires the development of new growth parameters. A method to develop and refine the growth parameters was followed. First, the catalyst must be granulated into nanoparticles to facilitate the nucleation of CNTs. Once the pretreatment or granulation process has been verified by SEM or AFM measurements the growth phase can be refined to achieve quality CNT growth. The MPE-CVD synthesis process was refined for sputtered Ni catalyst with a Ti barrier and a reliable recipe was developed. Vertically aligned CNT growth was not achieved during this research effort.

The second CVD synthesis method developed was via thermal CVD. A similar process to that used for the MPE-CVD method was followed to achieve reliable CNT growth. Barriers of Ti and Cr were used with Ni and Fe catalyst of differing thicknesses to determine the best combination for CNT growth and field emission performance. Again, it was shown that any changes in the barrier or catalyst material change the granulation, done by annealing for T-CVD, and growth characteristics. Ni proved ineffective for the T-CVD process used, yielding no CNTs. Fe with a Ti barrier was

determined to be the best catalyst/barrier combination for the current T-CVD process. Vertically aligned CNTs were not achieved via T-CVD either.

CNT carpet samples from both synthesis methods were characterized by Raman spectroscopy and SEM measurements. Using both a D/G ratio and G'/D ratio from the Raman shift of a sample as a more accurate method for determining CNT quality was proposed. However, the G'/D ratio seemed to be particularly susceptible to degradation when the CNT sample under test was vertically aligned. This was due to the defects present at the exposed tips of the CNTs where the metal catalyst forms a plug or cap on the CNT. Analysis also showed that Raman shift cannot be used alone to determine CNT sample quality. The sample with the best Raman shift turned out to be a poor CNT sample due to sparse growth, dispersive CNT diameters, and the formation of excessive amorphous carbon. All qualities easily identified with SEM micrographs. The disparity in quality assessment was ascribed to the individual CNTs being relatively defect free which would affect the Raman shift, but the sample as a whole was still poor per the reasons already mentioned. The MPE-CVD grown CNT samples were on the opposite end of the spectrum. The Raman shift indicated high defect densities, but SEM micrographs showed dense CNT growth with uniform diameters and no amorphous carbon. The MPE-CVD process was also shown to have more control over the length of the CNTs.

Field emission testing was performed on both MPE-CVD and T-CVD samples and it was shown that good Raman shift ratios does not correlate to good field emission performance, unless the physical qualities observed through SEM images are also good.

The T-CVD grown Ti₂₅/Fe₁₀ CNT sample had the best overall qualities, good Raman shift and observed physical qualities, and also had the best field emission performance. In all cases the MPE-CVD samples performed much worse than the T-CVD samples. This is due to a combination of factors, which include the CNT length and areal density. The MPE-CVD CNTs were much more densely packed and were only 1-2 μm in length. Both of these traits increase electrostatic screening effects which in turn reduce field emission performance of CNT carpets. The T-CVD samples tested were both less densely packed and significantly longer, $\sim 20+$ μm . The MPE-CVD samples were determined to be better candidates for incorporation into gated field emission devices where the traits that reduced performance for the diode configured carpet samples will facilitate a triode configuration which will significantly increase overall device performance. The current T-CVD process requires more control over the CNT length before integration into gated devices.

A sputtered carbon buffer layer was deposited between the barrier and catalyst layer as a potential method to isolate the catalyst from the barrier layer to make it possible to change the barrier without having to adjust or change the growth recipe. The results were mixed. The carbon layer slightly improved the quality of the CNTs on a Cr barrier, but slightly decreased the quality of CNTs on the Ti barrier. The effects of the carbon buffer on field emission were even more impressive. The Cr/C/Fe samples saw a large performance increase over the Cr/Fe samples. The carbon buffer degraded the field emission performance of the Ti barrier samples. The combined field emission and physical analysis showed that reliable CNT synthesis processes had been developed for

both MPE-CVD and T-CVD. Albeit the MPE-CVD sample requires a Ti/Ni barrier/catalyst combination and the T-CVD process worked best with a Ti/Fe combination.

A simple gated array device and fabrication process was proposed. Then finite element analysis was used to optimize the device dimensions to maximize the electric field strength at the tips of vertically aligned CNTs. Both the simple gated array device and the optimized device were fabricated. A conventional photolithography process was used to fabricate larger, $>1\text{ }\mu\text{m}$, element array devices and an inexpensive novel nanosphere lithography process was used to fabricate sub-micron element array devices. All fabrication steps were demonstrated, but fully functional gated devices were not fabricated. Devices with the gate metal shorted to the substrate were tested for field emission and compared with a carpet sample. The results confirmed the effects of electrostatic screening and showed that field emission performance could be improved by limiting these screening effects.

7.1. Contributions

This research effort has resulted in a number of contributions to the field of CNT synthesis, characterization, and field emission. These unique contributions are summarized below.

The work documented in Chapter III showed that material stresses have a significant effect on CNT synthesis. Two physical vapor deposition methods, sputtering and evaporation, were used for both the barrier and catalyst layers. Each deposition method was analyzed and differences in compressive and tensile stresses identified as the

most likely cause of the differences in CNT growth. Sputtering was determined to have more control over the material stresses and resulted in successful CNT growth via MPE-CVD. This research effort also further defined the relationship between catalyst thickness and CNT diameter by showing the catalyst thickness has less effect than the granulation process in determining the resulting CNT diameters. This particular effort also confirmed Ostwald ripening effects which had recently been documented [34].

Chapter IV covered efforts to develop T-CVD synthesis and characterize and test the CNT carpets produced. It was shown that differences in barrier layer thickness could alter the growth process as significantly as changing the deposition method. The G' peak was used as a method for determining MWCNT quality with Raman spectroscopy. It was shown that when the CNT sidewalls are exposed to the excitation laser the G' peak can be used in the ratio of G' peak intensity to D peak intensity, but when the CNTs are vertically aligned the G' peak cannot be used to determine CNT quality. The ratio of D/G peak intensities is still effective at showing CNT quality. A significant discovery during this effort was the large increase in field emission performance for some barrier/catalyst combinations when a sputtered carbon buffer layer was deposited between the barrier and catalyst. The Cr barriers showed slight improvements in CNT quality with the addition of the carbon buffer, but field emission current density increased by as much as 100x. Relationship between CNT quality and field emission performance was documented. It was shown CNT quality alone cannot be used to predict good field emission performance. The areal density and presence of amorphous carbon also must be

considered. The combination of Raman shift data with SEM images was shown to be effective at predicting which CNT carpets would have good field emission performance.

Chapters V and VI were the results of a coordinated effort to design, fabricate, and test gated CNT field emission arrays. Finite element analysis was used to develop a design optimization process. The modeling and simulation results showed that for gated arrays screening effects are mitigated from element to element, but are dominant within an element. The results led to optimizations in element size, shape, and CNT length. Element shape was particularly interesting because the 3D simulations indicated square shaped array elements are more effective for maximizing electric field strength than round elements. A novel fabrication process was developed using nanosphere lithography for the optimized design. The process was shown to be effective for arrays with elements of 500 nm and 250 nm with the potential elements small enough to limit CNT growth to one per element. Testing of prototype arrays was performed and the results used to confirm simulation results that gated structures will reduce screening effects between elements. As with any research effort, every new piece of information results in three new questions. Where future research should be focused is covered in the next section.

7.2. Future Research

For the immediate future, all research efforts should be focused on completing the fabrication and testing of fully functioning gated array devices. Then process improvements towards vertically aligned CNTs within the devices can be accomplished in parallel with other field emission related research. With working gated field emission

devices, sensor suites could be developed to measure the energy bandwidth of the emitted electrons and phosphor screens could be used to gage or measure the electron plume created during field emission.

The MPE-CVD growth process should be further refined to successfully incorporate DC stage biasing for vertically aligned CNT growth. Once vertically aligned CNTs can be reliably grown, comparison studies could be performed to determine if alignment improves field emission performance over non-aligned CNTs.

The T-CVD process should be refined to allow more control over the length and areal density of the CNTs to facilitate integration into gated devices. Future research could also focus on the interactions of the carbon buffer layer with the catalyst and barrier layers to determine the mechanism or process that drives the field emission improvements seen with the chrome barrier samples but not the titanium barrier samples.

There is a lot of room for improvement in methods of characterizing the quality of multi-walled carbon nanotubes, both with in this research effort and the body of literature as a whole. A more refined and focused Raman spectroscopy study could be conducted to determine better relationships between the peak intensity ratios and the quality of the MWCNTs. Other aspects of Raman spectroscopy not considered in this research and currently not mentioned in the literature when Raman spectroscopy is applied to MWCNTs is peak width and peak shift. Both of which can be easily measured and may provide valuable insights into the quality of MWCNTs. The use of different wavelengths of excitation laser should also be considered in any further efforts of characterization via Raman spectroscopy.

The results reported in this effort indicate stress of the catalyst layer and possibly the barrier layer have significant effects on CNT growth. Samples used for this research had both barrier layer and catalyst layer sputtered or evaporated. Further study on these stress effects would provide valuable information about the catalyst granulation and CNT growth. Which layers have the most effect could be determined by swapping the deposition methods of the barrier and catalyst layers. Thus, evaporate the catalyst on a sputtered barrier and vice versa to determine if it is only the catalyst intrinsic stress that affects growth or if the barrier stresses also play a part. The sputtering process could also be adjusted to determine what effects varying the pressure, which varies the intrinsic stress, would have on CNT growth. Measuring the intrinsic stress as the thickness of the barrier layer is increased could also be used to determine growth recipes compatible with much thicker barrier layers.

The finite element analysis performed in this effort focused on the device design and only considered the electric field strength and physical dimensions of the CNTs. A more robust model could be developed to include actual electrical and mechanical properties of MWCNTs. The model would become more complicated but also provide much more insight if it incorporated field emission and the resulting current flow. Modeling and simulation of the proposed complexity would require a scaled approach. First defining the physical properties and validating a model of a single CNT; then simulating field emission from a single CNT and incrementally building up to a complete array.

All of these research areas maintain a focus on field emission, but with reliable methods of growing CNTs available the areas of potential research open up to many other potential CNT applications.

VIII. Bibliography

- [1] Iijima, S., (1991). "Helical Microtubules of Graphitic Carbon," *Nature*, 354, 56-58.
- [2] Meyyappan, M. *Carbon Nanotubes: Science and Applications*. CRC Press, Boca Raton, 2004.
- [3] Chhoker, S., Srivastava, S. K., and Vankar, V. D. (2007). "Field emission properties of carbon nanostructures: A review." Paper presented at the *Physics of Semiconductor Devices, 2007. IWPSD 2007*. 820-826.
- [4] Williams, L., Walker, M., Kumsomboone, V., and Ready, W. (2008). "Experimental characterization of a carbon nanotube field emission cathode," *44th AIAA/ASME/SAE/ASEE Joint Propulsion Conference & Exhibit*, Hartford, CT.
- [5] Agüero, V., and Adamo, R. (2000). "Space applications of spindt cathode field emission arrays." 6th Spacecraft Charging Technology Conference, 347-352.
- [6] Busek Co. *Field emission cathodes*. Retrieved March/21, 2009, from <http://www.busek.com/cathodes.html>
- [7] Leonard, F., *The Physics of Carbon Nanotube Devices*. William Andrew, Norwich, 2008
- [8] Radushkevich, L., Lukyanovich, V., "O structure ugleroda, obrazujucesja pri termiceskom razlozenii okisi ugleroda na zeleznom kontakte," *Zurn. Fisic. Chim.* 26, 88-95 (1952). Accessed at: <http://carbon.phys.msu.ru/publications/1952-radushkevich-lukyanovich.pdf> (12 Feb 2009).
- [9] Reich, S., Thomsen, C., and Maultzsch, J. *Carbon Nanotubes: Basic Concepts and Physical Properties*. Wiley, Germany, 2004.
- [10] Bhushan, B. *Springer Handbook of Nanotechnology*. Springer - Verlag. 2007
- [11] Pierson, H. *Handbook of Carbon, Graphite, Diamond and Fullerenes – Properties, Processing and Applications*. William Andrew Publishing, New Jersey, 1993.
- [12] O'Connell, M. *Carbon Nanotubes: Properties and Applications*. CRC Press, Boca Raton, 2006.
- [13] Hamada, N., Samada, S., and Oshiyama, A., (1992) "New One-Dimensional Conductors: Graphitic Microtubules," *Phys. Rev. Lett.* 68, 1579-1581.

- [14] Saito, R., Dresselhaus, G., and Dresselhaus, M. S. *Physical Properties of Carbon Nanotubes*. Imperial College Press, London, 1998.
- [15] Tanaka, K., Yamabe, T., and Fukui, K. *The Science and Technology of Carbon Nanotubes*. Elsevier, New York, 1999.
- [16] Guan, L. (2008), "Smallest carbon nanotube assigned with atomic resolution accuracy," *Nano Letters*, 8, 459-462.
- [17] Lair, S. L., Herndon, W. C., and Murr, L. E., & Quinones, S. A. (2006). "End cap nucleation of carbon nanotubes," *Carbon*, 44, 447-455.
- [18] Ventra, M., Evoy, S., and Heflin, J., *Introduction to Nanoscale Science and Technology*. Kluwer Academic Publishers, New York, 2004.
- [19] Geckeler K. E., and Rosenberg E., *Functional Nanomaterials*. American Scientific Publishers, California, 2006.
- [20] Bates, H., Brand, O., Fedder, G., Hierold, C., Korvink, J., and Tabata, O. *Enabling Technology for MEMS and Nanodevices*. Weinheim, Germany, Wiley-VCH, 2004.
- [21] Walters, D. A., Ericson, L. M., Casavant, M. J., Liu, J., Cobert, D. T., Smith, K. A., *et al.* (1999). "Elastic strain of freely suspended single-wall carbon nanotube ropes," *Applied Physics Letters*, 74, 3803-3805.
- [22] Nalwa H. S. *Nanostructured Materials and Nanotechnology*. Academic Press, California, 2002.
- [23] Iijima, S., Brabec, C., Maiti, A., and Bernholc, J. (1996), "Structural flexibility of carbon nanotubes," *The Journal of Chemical Physics*, 104, 2089-2092.
- [24] Pop, E., Mann, D., Wang, Q., Goodson, K., and Dai, H. (2006). "Thermal conductance of an individual single-wall carbon nanotube above room temperature," *Nano Letters*, 6, 96-100.
- [25] Kim, P., Shi, L., Majumdar, A., and McEuen, P. L. (2001). "Thermal transport measurements of individual multiwalled nanotubes," *Physical Review Letters*, 87, 5502-5506.
- [26] Balandin, A. A., Ghosh, S., Bao, W., Calizo, I., Teweldebrhan, D., Miao, F., *et al.* (2008). "Superior thermal conductivity of single-layer graphene," *Nano Letters*, 8, 902-907.

- [27] Avouris, P.; Appenzeller, J.; Martel, R.; and Wind, S.J., "Carbon nanotube electronics," *Proceedings of the IEEE*, 91, pp. 1772-1784, Nov 2003.
- [28] Pochet M., "Characterization of the field emission properties of carbon nanotube film formed on silicon carbide substrate by surface decomposition," Master's thesis, Air Force Institute of Technology, 2006.
- [29] Terranova, M., Sessa, V., and Rossi, M. (2006). "The world of carbon nanotubes: An overview of CVD growth methodologies," *Chemical Vapor Deposition*, 12, 315-325.
- [30] Li, Y., Mann, D., Rolandi, M., Kim, W., Ural, A., Hung, S., *et al.* (2004). "Preferential growth of semiconducting single-walled carbon nanotubes by a plasma enhanced CVD method," *Nano Letters*, 4, 317-321.
- [31] Maschmann, M. R., Amama, P. B., Goyal, A., Iqbal, Z., and Fisher, T. S. (2006). "Freestanding vertically oriented single-walled carbon nanotubes synthesized using microwave plasma-enhanced CVD," *Carbon*, 44, 2758-2763.
- [32] Hayashi, H., Koga, M., Kashirajima, J., Takahashi, K., Hayashi, Y., and Nishino, S. (2002). "Large-scale synthesis of aligned carbon nanotubes by surface-wave-excited microwave-plasma-enhanced chemical vapor deposition," *Japanese Journal of Applied Physics*, 41, 1488-1491.
- [33] Garg, R., Kim, S., Hash, D., Gore, J., & Fisher, T. (2008). "Effects of feed gas composition and catalyst thickness on carbon nanotube and nanofiber synthesis by plasma enhanced chemical vapor deposition," *Journal of Nanoscience and Nanotechnology*, 8, 3068-3076.
- [34] Amama, P., Pint, C., McJilton, L., Kim, S., Stach, E., Murray, T., *et al.* (2009). "Role of water in super growth of single-walled carbon nanotube carpets," *Nano Letters*, 9, 44-49.
- [35] Nessim, G., Hart, A., Kim, J., Acquaviva, D., Oh, j., Morgan, C., *et al.* (2008). "Tuning of vertically-aligned carbon nanotube diameter and areal density through catalyst pre-treatment," *Nano Letters*, 8, 3587-3593.
- [36] Chang, S., Lin, T., Li, T., and Huang, S. (2008). "Carbon nanotubes grown from nickel catalyst pretreated with H₂/N₂ plasma," *Microelectronics Journal*, 39, 1572-1575.
- [37] Teo, K., Lee, S., Chhowalla, M., Semet, V., Binh, V., Groening, O., *et al.* (2003). "Plasma enhanced chemical vapour deposition carbon nanotubes/nanofibres—how uniform do they grow?" *Nanotechnology*, 14, 204-211.

- [38] Lin, H., Chang, Y., Yen, J., Hsu, J., Leu, I., and Hon, M. (2004). "Selective growth of vertically aligned carbon nanotubes on nickel oxide nanostructures created by atomic force microscope nano-oxidation," *Chemical Physics Letters*, 399, 422-425.
- [39] Kempa, K., Kimball, B., Rybczynski, J., Huang, Z. P., Wu, P. F., Steeves, D., *et al.* (2003). "Photonic crystals based on periodic arrays of aligned carbon nanotubes," *Nano Letters*, 3, 13-18.
- [40] Rybczynski, J., Wang, Y., Banerjee, D., Kempa, K., and Ren, Z. (2005). "Large-scale periodic patterns and their application for growing aligned nanotube and nanowire arrays," *Proceedings of SPIE, the International Society for Optical Engineering*, 6003
- [41] Lee, D., Shin, D., Lee, W., and Kim, S. (2008). "Fabrication of vertical carbon nanotube arrays from self-assembled block copolymer films," *Journal of Nanoscience and Nanotechnology*, 8, 5571-5575.
- [42] Heer, W. A. d., Chatelain, A., and Ugarte, D. (1995). "A carbon nanotube field-emission electron source," *Science*, 270, 1179-1181.
- [43] Fursey, G., *Field Emission in Vacuum Microelectronics*. Kluwer Academic/Plenum Publishers, New York, 2005.
- [44] Paulini, J., Klein, T., and Simon, G. (1993). "Thermo-field Emission and the Nottingham Effect," *Journal of Physics D: Applied Physics*, 26, 1310-1315.
- [45] Seelaboyina, R., Boddepalli, S., Noh, K., Jeon, M., and Choi, W. (2008). "Enhanced field emission from aligned multistage carbon nanotube emitter arrays," *Nanotechnology*, 19, 65605-65609.
- [46] Chen, C., Shao, W., Ding, M., Li, X., Bai, B., Zhang, F., *et al.* (2007). "Development of micro-patterned carbon nanotube field emission arrays for high current applications," Paper presented at the *Vacuum Electronics Conference, 2007. IVEC '07. IEEE International*.
- [47] Suzuki, S., Bower, C., Watanabe, Y., and Zhou, O. (2000). "Work functions and valence band states of pristine and cs-intercalated single-walled carbon nanotube bundles," *Applied Physics Letters*, 76, 4007-4009.
- [48] Xu, Z., Bai, X., Wang, E., and Wang, Z. (2005). "Field emission of individual carbon nanotube with in situ tip image and real work function," *Applied Physics Letters*, 87, 163106-163106-3.

- [49] Bonard, J., Kind, H., Stöckli, T., and Nilsson, L. (2001). "Field emission from carbon nanotubes: The first five years," *Solid-State Electronics*, 45, 893-914.
- [50] Zhu, W., Bower, C., Zhou, O., Kochanski, G., and Jun, S. (1999). "Large current density from carbon nanotube field emitters," *Applied Physics Letters*, 75, 873-875.
- [51] Williams, L., and Walker, M., "Experimental Characterization of a Carbon Nanotube Field Emission Cathode," AIAA-2008-5015, 44th Joint Propulsion Conference, Hartford, CT, July 20-23, 2008.
- [52] Milne, W., Teo, K., Minoux, E., Groening, O., Gangloff, L., Hudanski, L., *et al.* (2006). "Aligned carbon nanotubes/fibers for applications in vacuum microwave amplifiers," *Journal of Vacuum Science & Technology B: Microelectronics and Nanometer Structures*, 24, 345-348.
- [53] Sohn, J. I., Lee, S., Song, Y., Choi, S., Cho, K., and Nam, K. (2001). "Large field emission current density from well-aligned carbon nanotube field emitter arrays," *Current Applied Physics*, 1, 61-65.
- [54] Chuang, C., Huang, J. H., Lee, C., and Chang, Y. (2004). "Fabrication and field emission characteristics of high density carbon nanotubes microarrays," Paper presented at the *Vacuum Nanoelectronics Conference, 2004. IVNC 2004. Technical Digest of the 17th International*, 220-221.
- [55] Manohara, H., Bronikowski, M., Hoenk, M., Hunt, B., and Siegel, P., (2005) "High-current-density Field Emitters Based on Arrays of Carbon Nanotube Bundles," *Journal of Vacuum Science & Technology B: Microelectronics and Nanometer Structures*, 23, 157-162.
- [56] Wong, Y. M., Kang, W. P., Davidson, J. L., Choi, B. K., Hofmeister, W., and Huang, J. H. (2005). "Field emission triode amplifier utilizing aligned carbon nanotubes," *Diamond and Related Materials*, 14, 2069-2073.
- [57] Fujii, S., Honda, S., Machida, H., Kawai, H., Ishida, K., Katayama, M., *et al.* (2007). "Efficient field emission from an individual aligned carbon nanotube bundle enhanced by edge effect," *Applied Physics Letters*, 90, 153108-153108-3.
- [58] Aplin, K. L., Kent, B. J., Song, W., and Castelli, C. "Field emission performance of multiwalled carbon nanotubes for a low-power spacecraft neutralizer," *Acta Astronautica*, *In Press, Corrected Proof* doi:DOI: 10.1016/j.actaastro.2008.10.012
- [59] Nilsson, L., Groening, O., Emmenegger, C., Kuettel, O., Schaller, E., Schlapbach, L., *et al.* (2000). "Scanning field emission from patterned carbon nanotube films," *Applied Physics Letters*, 76, 2071-2073.

- [60] Suh, J., Jeong, K., Lee, J., and Han, H. (2002). "Study of the field-screening effect of highly ordered carbon nanotube arrays," *Applied Physics Letters*, 80, 2392-2394.
- [61] Smith, R., and Silva, S. (2009). "Maximizing the electron field emission performance of carbon nanotube arrays," *Applied Physics Letters*, 94(13), 133104-133104-3.
- [62] Niemann, D., Silan, J., Killian, J., Schwanfelder, K., Rahman, M., Meyyappan, M., *et al.* (2008). "Carbon nanotube field emission devices with integrated gate for high current applications," Paper presented at the *Nanotechnology, 2008. NANO '08. 8th IEEE Conference on*, 456-459.
- [63] Kossler M., "Patterning and Characterization of Carbon Nanotubes Grown in a Chemical Vapor Deposition Chamber," Master's thesis, Air Force Institute of Technology, 2009.
- [64] J. E. Mahon, *Physical Vapor Deposition of Thin Films*, Wiley, New York, NY (2000).
- [65] C. V. Thompson and R. Carel, (1996). "Stress and grain growth in thin films," *Mechanical Physics of Solids, Journal of*, 44, 657–673.
- [66] H. Windischmann, (1991). "Intrinsic stress in sputtered thin films," *Vacuum Science Technology: A, Journal of*, 9, 2431–2437.
- [67] N. Radic, P. Dubcek, S. Berstorff, I. Djerdj, and A. M. Tonejc, (2007). "Structural study of nanocrystalline nickel thin films," *Applied Crystallography, Journal of*, 40, 377–382.
- [68] Y. M. Wong, W. P. Kang, J. L. Davidson, B. K. Choi, W. Hofmeister, and J. H. Huang, (2006). "Fabrication of aligned convex cnt field emission triode by mpcvd," *Diamond and Related Materials*, 15, 334–340.
- [69] Dresselhaus, M. S., Ado J., Hofman, M., Dresselhaus G., and Saito, R., (2010). "Perspectives on Carbon Nanotubes and Graphene Raman Spectroscopy," *Nano Letters*, 10, 751-758.
- [70] DiLeo, R., Landi, B., and Raffaele, R., (2007). "Purity assessment of multiwalled carbon nanotubes by Raman spectroscopy," *Journal of Applied Physics*, 101, 064307-064307-6.
- [71] Wong, Y., Kang, W., Davidson, J., Hofmeister, W., Wei, S., and Huang, J. (2005). "Device characterization of carbon nanotubes field emitters in diode and triode configurations," *Diamond & Related Materials*, 14, 697-703.

- [72] Crossley, B. L., Kossler, M., Coutu Jr., R. A., Starman, L. A., & Collins, P. J., (2010). "Effects of hydrogen pretreatment on physical-vapor-deposited nickel catalyst for multi-walled carbon nanotube growth." *Journal of Nanophotonics*, 4, 049502-049502-6.
- [73] Yinmin M. Wong, Y., *et al.* (2005). "Array geometry, size and spacing effects on field emission characteristics of aligned carbon nanotubes," *Diamond and Related Materials*, 14, 2078-2083.
- [74] Crossley, B. L., Kossler, M., Starman, L. A., Coutu Jr., R. A., and Collins, P. J., (2009). "Optimization of carbon nanotube field emission arrays," *Proc. COMSOL* 6288.
- [75] Bayraktaroglu, B., Guest Lecture Presentation, EENG 779 Introduction to Nanotechnology. Graduate School of Engineering and Management, Air Force Institute of Technology, Wright-Patterson AFB, OH, January 2009.
- [76] Fischer, U. Ch., and Zingsheim, H. P., (1981). "Submicroscopic pattern replication with visible light," *J. Vac. Sci. Technol.* 19, 881-885.
- [77] Deckman, H. W., and Dunsmuir, J. H., (1982). "Natural lithography," *Appl. Phys. Lett.* 41, 377-379.
- [78] Haginoya, C., Ishibashi, M., and Koike, K., (1997). "Nanostructure array fabrication with a size-controllable natural lithography," *Appl. Phys. Lett.* 71, 2934-2936.
- [79] Haynes, C. L., and Van Duyne, R. P., (2001). "Nanosphere Lithography: A Versatile Nanofabrication Tool for Studies of Size-Dependent Nanoparticle Optics," *J. Phys. Chem. B*, 105, 5599-5611.
- [80] Kossler, M., Crossley, B. L., Coutu, Jr., R. A., Starman, L. A., and Collins, P. J., (2009). "Study on the effects of hydrogen pretreatment on nickel catalyst used for multi-walled carbon nanotube growth." *Proc. SPIE* 7399(739904).
- [81] Lee, B. K., Kim, S. K., Lee, J. H., Kim, N. H., and Roh, Y., (2008). "Nanometer-scaled triangular platinum islands fabricated using the bridge phenomenon of polystyrene beads," *J. Vac. Sci. Technol. A*, 26, 819-823.

REPORT DOCUMENTATION PAGE				Form Approved OMB No. 074-0188	
<p>The public reporting burden for this collection of information is estimated to average 1 hour per response, including the time for reviewing instructions, searching existing data sources, gathering and maintaining the data needed, and completing and reviewing the collection of information. Send comments regarding this burden estimate or any other aspect of the collection of information, including suggestions for reducing this burden to Department of Defense, Washington Headquarters Services, Directorate for Information Operations and Reports (0704-0188), 1215 Jefferson Davis Highway, Suite 1204, Arlington, VA 22202-4302. Respondents should be aware that notwithstanding any other provision of law, no person shall be subject to a penalty for failing to comply with a collection of information if it does not display a currently valid OMB control number.</p> <p>PLEASE DO NOT RETURN YOUR FORM TO THE ABOVE ADDRESS.</p>					
1. REPORT DATE (DD-MM-YYYY) 16-06-2011		2. REPORT TYPE Doctoral Dissertation		3. DATES COVERED (From – To) September 2007 – June 2011	
4. TITLE AND SUBTITLE Carbon Nanotube Field Emission Arrays				5a. CONTRACT NUMBER	
				5b. GRANT NUMBER	
				5c. PROGRAM ELEMENT NUMBER	
6. AUTHOR(S) Benjamin L. Crossley, Maj, USAF				5d. PROJECT NUMBER 08-237	
				5e. TASK NUMBER	
				5f. WORK UNIT NUMBER	
7. PERFORMING ORGANIZATION NAMES(S) AND ADDRESS(S) Air Force Institute of Technology Graduate School of Engineering and Management (AFIT/EN) 2950 Hobson Way WPAFB, OH 45433-7765				8. PERFORMING ORGANIZATION REPORT NUMBER AFIT/DCE/ENG/11-03	
9. SPONSORING/MONITORING AGENCY NAME(S) AND ADDRESS(ES) Capt Michael Etan Advanced Systems and Technology Directorate National Reconnaissance Office 14675 Lee Rd Chantilly, VA 20151 Phone: 571-643-7471 email: etanmich nro.ic.gov				10. SPONSOR/MONITOR'S ACRONYM(S) NRO	
				11. SPONSOR/MONITOR'S REPORT NUMBER(S)	
12. DISTRIBUTION/AVAILABILITY STATEMENT Approval for public release; distribution is unlimited					
13. SUPPLEMENTARY NOTES This material is declared a work of the U.S. Government and is not subject to copyright protection in the United States.					
14. ABSTRACT <p>This effort exploits the unique physical and electrical characteristics of carbon nanotubes (CNTs) for field emission applications. Carbon nanotube field emission devices are designed, fabricated, and tested. Two reliable CNT synthesis methods, microwave plasma enhanced chemical vapor deposition (MPE-CVD) and thermal chemical vapor deposition (T-CVD), are developed. The physical properties of the resulting CNTs are analyzed using Raman spectroscopy and Scanning electron microscopy (SEM) and then tested for field emission performance. The T-CVD grown CNTs are shown to have fewer growth defects, but suffer from less process control making integration into devices difficult without further process development. Field emission testing shows the T-CVD CNTs to be much better emitters, exceeding 13 mA/cm² at an electric field of only 1.4 V/μm, while the best MPE-CVD CNTs only managed ~1 mA/cm² at the much higher electric field of 4.56 V/μm.</p> <p>Two methods of device fabrication, conventional photolithography and nanosphere lithography, are developed and used to fabricate gated field emission arrays. Finite element analysis is used to optimize the gated array design to maximize the electric field strength. All fabrication steps are successfully demonstrated and prototype devices tested and compared to simple CNT carpet samples showing marked improvements by reducing electrostatic screening effects.</p>					
15. SUBJECT TERMS Multi-walled carbon nanotubes, carbon nanotube synthesis, plasma enhanced chemical vapor deposition, CVD, thermal chemical vapor deposition, field emission, finite element analysis, nanosphere lithography					
16. SECURITY CLASSIFICATION OF:		17. LIMITATION OF ABSTRACT		18. NUMBER OF PAGES	
REPORT U	ABSTRACT U	c. THIS PAGE U	UU	157	19a. NAME OF RESPONSIBLE PERSON Ronald A. Coutu, Jr.
					19b. TELEPHONE NUMBER (Include area code) (937) 255-3636 x7230; Ronald.coutu.afit.edu

Standard Form 298 (Rev: 8-98)

Prescribed by ANSI Std. Z39-18